SRPK2 regulates active zone ultrastructure and RIM1 phosphorylation to tune presynaptic function and plasticity

Dissertation

zur
Erlangung des Doktorgrades (Dr. rer. nat)
der
Mathematisch-Naturwissenschaftlichen Fakultät
der
Rheinischen Friedrich-Wilhelms-Universität Bonn

vorgelegt von

Julia Betzin

aus
Bergisch Gladbach

Bonn, February 2020

Angefertigt mit der Genehmigung der Mathematisch-Naturwissenschaftlichen
Fakultät der Rheinischen Friedrich-Wilhelms-Universität Bonn

1. Gutachter: Prof. Dr. Susanne Schoch McGovern

2. Gutachter: Prof. Dr. Walter Witke

Tag der Promotion: 28.05.2020

Erscheinungsjahr: 2020

Index

List of figures

List of tables

1. Summary

Chemical synapses communicate through the release of neurotransmitter-filled synaptic vesicles into the synaptic cleft. Synapses are able to dynamically adapt to the changes in the neuronal network by strengthening or weakening synaptic connections. How these changes that can range from milliseconds to days are mediated is still unknown. Potential mechanisms to achieve this dynamic regulation are the posttranslational modifications of proteins involved in synaptic transmission. Many active zone (AZ) proteins are known phospho-proteins and in the last years it was postulated that protein phosphorylation, especially in the presynapse, is regulated during neuronal activity.

Here, we characterized a novel presynaptic kinase, the Serine-Arginine Protein Kinase 2 (SRPK2), and investigated its interaction with proteins of the AZ and its role in synaptic plasticity. SRPK2 was identified as a new integral component of the synaptic cytomatrix. For the first time, the phosphoproteome of SRPK2 was determined and RIM1 was identified as a direct target of SRPK2. Superresolution microscopy revealed that SRPK2 controls RIM1 nanoclusters and thereby potential release sites. Moreover, presynaptic SRPK2 and RIM1 clusters increase during homeostatic plasticity. We therefore propose that SRPK2 regulates the clustering of RIM1 by controlling its phosphorylation status by direct and indirect phosphorylation. The increase in synaptic strength during homeostatic plasticity is mediated by the translocation of SRPK2 to the presynapse resulting in the recruitment of RIM1 molecules to form new RIM1 nanoclusters.

2. Introduction

2.1 The synapse

The human brain consists of millions of neurons that communicate via their functional unit: the synapse. Synapses are intercellular signaling junctions and can be divided into chemical and electrical synapses (reviewed in Pereda, 2015). In electrical synapses, the communication is based on gap junction channels, which connect the cytoplasm of two adjacent cells. Ions and small molecules can pass the channels to signal to neighboring neurons. The majority of communication, however, is taking place at chemical synapses. The presynapse is separated from the postsynapse by the synaptic cleft that encompasses 20-100 nm. In the presynapse, neurotransmitter-filled synaptic vesicles are located. Upon stimulation by an action potential, synaptic vesicles fuse with the plasma membrane and release neurotransmitter into the synaptic cleft. The neurotransmitters target their respective receptors at the postsynapse and lead to the de- or hyperpolarization of the postsynaptic neuron.
The first visualization and proof of the synapse was achieved by electron microscopy (EM). This method allowed to look at nerve cells with a nanometer resolution (Robertson, 1953). EM was also used to further investigate the ultrastructure and led to the first description of synaptic vesicles by Palade and Palay and De Robertis as well as Benett (De Robertis and Bennett, 1955; Palay, 1956).

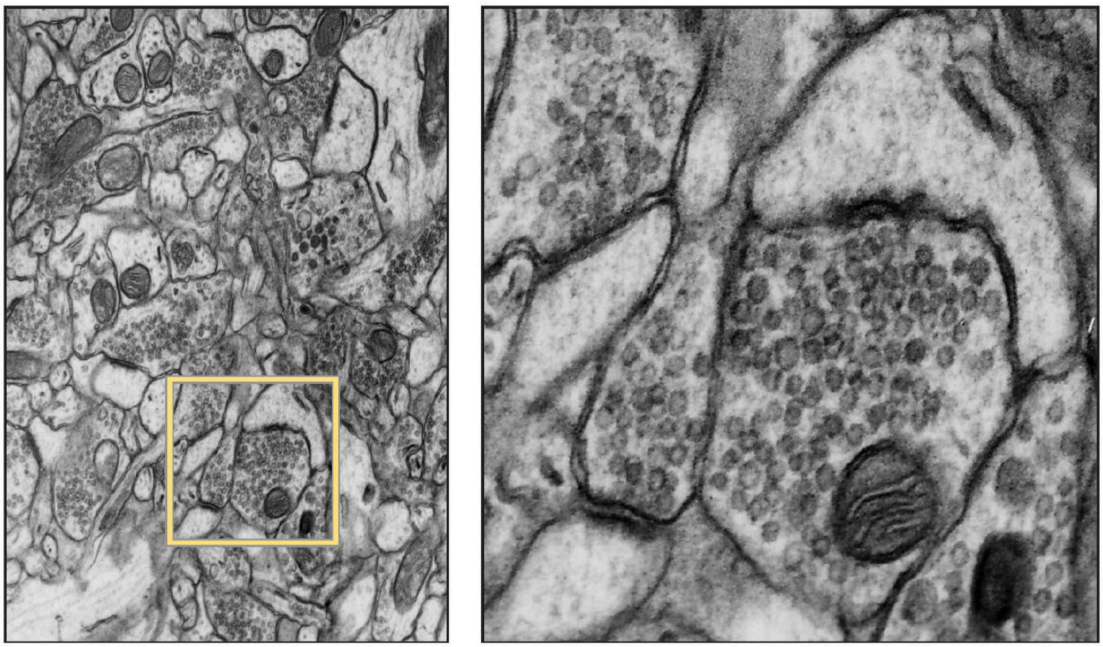

Figure 2.1: Electron micrograph of a synapse.
A presynaptic terminal with multiple synaptic vesicles opposed to a postsynaptic neuron. Some synaptic vesicles are docked at the presynaptic plasma membrane (Monday *et al.*, 2018).

2.2 Presynaptic plasticity

Synapses are highly dynamic structures in which both the protein scaffold in the presynapse as well as the synaptic output exhibit activity-dependent modulations (Sigrist and Petzoldt, 2016). The ability of synapses to dynamically adapt to changes in the neuronal network is termed synaptic plasticity. The synapse can respond to experience or neuronal activity by strengthening (potentiation) or weakening (depression) its output. Synaptic connections can be modified in a short time range (short-term plasticity), which includes alterations within milliseconds to minutes. Short-term plasticity results in transient behavioral changes and short-lasting forms of memory (reviewed in Citri and Malenka, 2008). However, alterations in the strength of synaptic connections can also be long lasting (long-term plasticity) leading to changes for hours or days. Hebb proposed already in 1949 that synaptic modifications such as strengthening are involved in memory formation. This was confirmed by experiments showing that repetitive stimulations of synapses in the hippocampus result in long-term potentiation (Bliss and Lømo, 1973; Bliss and Gardner-Medwin, 1973).

Voltage-gated Ca^{2+} channel (VGCC) play a crucial role during neurotransmitter release. Upon membrane depolarization, VGCC are activated and enable the entry of Ca^{2+} into the presynaptic terminal thereby initiating synaptic transmission. Consequently, VGCC and their role in presynaptic plasticity has been intensively studied. N-type channels are necessary for hippocampal presynaptic long-term potentiation (LTP) (Ahmed and Siegelbaum, 2009) while in the amygdala L-type channels are of importance (Fourcaudot *et al.*, 2009). Not only the recruitment itself of VGCC is important but their arrangement at the synapse. The formation of nanodomains of VGCC is mediated by VGGC-interacting proteins like RIM1 (Rab3-interacting molecule) (Han *et al.*, 2011) and is essential for presynaptic LTP (Nakamura *et al.*, 2015).

The molecular mechanisms underlying synaptic plasticity are being investigated and it is already known that gene transcription and translation play an important role in these processes (reviewed in Alberini, 2009). In addition, posttranslational modifications such as SUMOylation (Lee *et al.*, 2014), ubiquitination (reviewed in Hegde, 2017) and phosphorylation (reviewed in Lee, 2006) are involved.

Cycling adenosine monophosphate/protein kinase A (cAMP/PKA) signaling has been shown to be involved in multiple forms of presynaptic LTP or LTD. The phosphorylation of multiple PKA targets was identified to be important for different plasticity forms. For LTP at mossy fiber synapses projecting to CA3 pyramidal cells, phosphorylation of serine 97 of synaptotagmin-12 by PKA was described to be necessary (Kaeser-Woo *et al.*, 2013). Another PKA target, RIM1, is a key player in mediating neurotransmitter release and is important in regulating presynaptic plasticity (reviewed in Südhof, 2012). Presynaptic PKA-dependent LTP in hippocampal mossy fibers and cerebellar parallel fibers depends on RIM1α (Castillo *et al.*, 2002). It was demonstrated that RIM1 is phosphorylated by PKA at serine 413 and serine 1548, but only serine 413 was necessary for long-term presynaptic plasticity in cultured cerebellar neurons (Lonart *et al.*, 2003). The importance of this phosphorylation site was questioned using a RIM1 knock-in mouse that had an alanine (phospho-deficient) instead of a serine at position 413. The RIM1-S413A knock-in model did not exhibit any deficiency in presynaptic long-term plasticity (Kaeser *et al.*, 2008). Thus, RIM1 is essential for presynaptic LTP in both synapse types but the plasticity is not mediated by PKA phosphorylation of RIM1 at serine

413. RIM1 was additionally shown to mediate short-term plasticity at CA1 excitatory synapses (Schoch *et al.*, 2002).
Phosphorylation of other presynaptic proteins like synaptosomal-associated protein of 25 kDa (SNAP-25) by PKC (Katayama *et al.*, 2017) and complexin by PKA (Cho *et al.*, 2015) are necessary for short-term presynaptic plasticity. Altogether, the importance of kinases as well as the phosphorylation of different presynaptic proteins for presynaptic plasticity has been demonstrated. However, the precise mechanism of presynaptic plasticity and how the dynamic changes in the neuronal network are regulated is still unclear.

2.3 Homeostatic presynaptic plasticity

To maintain a physiological level of activity in a neuronal network, synaptic scaling counteracts activity-dependent forms of plasticity and maintains network stability. Synaptic scaling describes a form of homeostatic plasticity, which acts as a negative feedback (reviewed in Pozo and Goda, 2011). Homeostatic scaling is characterized by an increase of both presynaptic calcium influx and the readily releasable pool (RRP) (Davis and Müller, 2015). This change can be induced by a decrease in postsynaptic receptor function or by blocking sodium channels using tetrodotoxin (TTX) and results in a compensatory upregulation of presynaptic neurotransmitter release. The increase in the synaptic output can last from seconds to days and can be modulated up to a two-fold increase (Frank *et al.*, 2006). The alteration of postsynaptic receptor function is used to study the molecular mechanisms of presynaptic homeostatic plasticity: In *Drosophila melanogaster* the glutamate receptor inhibitor philantotoxin-433 induces presynaptic homeostatic scaling, which is independent of transcription and translation (Goold and Davis, 2007).
Interestingly, the addition of release sites was shown for chronic plasticity induction in *Drosophila melanogaster* (Böhme *et al.*, 2019). To uncover the mechanism underlying homeostatic plasticity, different active zone proteins were analyzed. Thereby, $Ca_V2.1$ channels were identified to be necessary to express presynaptic scaling (Frank *et al.*, 2006). Moreover, Rab3-GTPase activating protein (GAP) facilitates the increase in synaptic output during presynaptic homeostatic plasticity (Müller *et al.*, 2011). For both rapid and chronic plasticity, a structural remodeling goes along with an increase in the abundance of several AZ proteins (Bruchpilot,

RIM-BP (RIM-binding protein), Unc13A, Syntaxin1A), which depends on Bruchpilot and RIM-BP expression as well as on their transport to the presynapse (Böhme *et al.*, 2019).

RIM mutants were used in *Drosophila melanogaster* to investigate the role of RIM during homeostatic plasticity because the RIM family is evolutionarily conserved and has been shown to control synaptic transmission in mammals (Schoch *et al.*, 2002, 2006). Moreover, the requirement of RIM1 for the docking of synaptic vesicles (Deng *et al.*, 2011) and a proper calcium channels at the AZ (Han *et al.*, 2011; Kaeser *et al.*, 2011) encouraged to investigate whether RIM regulates the dynamic changes in the neuronal network. The homeostatic elevation in presynaptic Ca^{2+} influx was not disturbed in RIM mutants (Müller *et al.*, 2012). However, the increase in the ready releasable pool was dependent on RIM indicating an important role of RIM during homeostatic plasticity (Müller *et al.*, 2012).

Consistent with the rapid form of philantotoxin-433-induced presynaptic homeostatic plasticity in *Drosophila melanogaster*, a rapid and reversible form of presynaptic homeostatic plasticity was observed in acute mouse brain slices (Delvendahl *et al.*, 2019). An enhancement in Ca^{2+}-current density, which was accompanied with an increase of the readily releasable pool, was detected to counteract a postsynaptic receptor perturbation. Similarly to *Drosophila melanogaster*, the network silencing in mammalian neuronal cultures induced by NMDA- or AMPA-receptor agonists resulted in a remodeling of the pre- and postsynaptic architecture as whole cell protein levels of multiple proteins (RIMs, Bassoon, ELKS, Munc13, liprin-α, synapsins and PSD-95, Homer1) were significantly reduced (Lazarevic *et al.*, 2011). The same effect was observed during presynaptic silencing by TTX treatment (Lazarevic *et al.*, 2011). The remodeling of the presynaptic architecture goes along with an increase of the size of the AZ (Murthy *et al.*, 2001). Interestingly, synaptic RIM1 levels were shown to correlate with synaptic activity (Lazarevic *et al.*, 2011) pointing to a regulatory role of RIM1 in synaptic plasticity. This correlation was neither observed for Munc13 nor for Bassoon. However, an elevation of synaptic $Ca_V2.1$ levels similar to RIM1 levels were observed upon silencing (Lazarevic *et al.*, 2011). The authors propose two different mechanisms to drive the remodeling at the presynapse: Protein synthesis might be modified or that degradation is altered (Lazarevic *et al.*, 2013). The decrease of bassoon and liprin-α in silenced neurons was achieved by an ubiquitin-proteasome (UPS)-dependent degradation (Lazarevic *et al.*, 2011). How the

protein levels of other AZ proteins like ELKS, Munc13 or RIM1 are modified in homeostatic plasticity remains unknown.

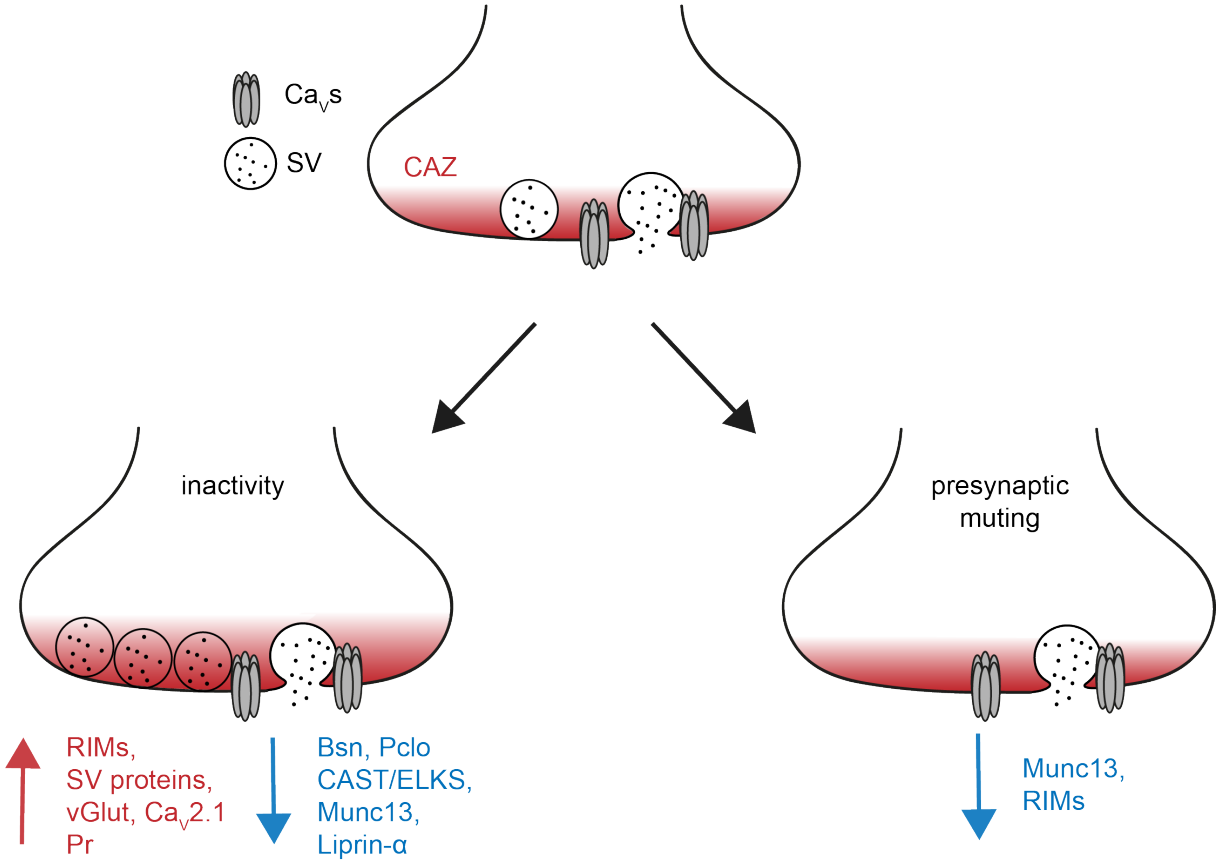

Figure 2.2: Molecular mechanisms of homeostatic plasticity.
Activity deprivation results in presynaptic upscaling with an increased readily releasable pool and an increase of the CAZ. Protein synthesis and protein degradation lead to a remodeling of the CAZ. Presynaptic muting induced by depolarization results in a reduction of the readily releasable pool and the degradation of Munc13 and RIM proteins. Modified from (Lazarevic *et al.*, 2013).

In contrast to homeostatic scaling, depolarization-induced synaptic muting results in the reduction of the RRP (Moulder *et al.*, 2006). Therefore, the bidirectional regulation of the RRP enables the maintenance of physiological level of activity during presynaptic homeostatic plasticity. Both RIM1 and Munc13 protein levels were increased in active synapses (Jiang *et al.*, 2010). Interestingly, the degradation of RIM1 in muted synapses is mediated by the UPS (Jiang *et al.*, 2010). Overexpression of RIM1 could restore presynaptic function demonstrating the importance of RIM1 for neuronal activity (Jiang *et al.*, 2010).

The data so far suggests that RIM1 is a key player in homeostatic plasticity. However, the precise mechanism how different AZ members control homeostatic plasticity remains to be delineated.

2.4 Role of posttranslational modifications in synaptic plasticity

In the last years, it has been demonstrated that posttranslational modifications are important to regulate synaptic plasticity. One posttranslational modification is the ubiquitination leading to the degradation of proteins by the ubiquitin-proteasome system. It has been shown that depolarization induces increased proteasome activity (Jiang *et al.*, 2010). RIM1α is degraded by the proteasome (Yao *et al.*, 2007) and presynaptic muting in neuronal cultures resulted in the degradation of cellular and synaptic RIM1 as well as Munc13-1 (Jiang *et al.*, 2010). In contrast, SUMOylation of RIM1 leads to clustering of $Ca_V2.1$ calcium channels and increases Ca^{2+} influx (Girach *et al.*, 2013).

The role of several kinases in synaptic plasticity has been studied. Presynaptic plasticity mechanisms depending on PKA have been described in chapter 2.2. Another kinase regulating synaptic plasticity in the hippocampus is the extracellular signal regulated kinase (ERK) (Vara *et al.*, 2009; Yamanaka *et al.*, 2016). ERK is activated during synaptic plasticity in the CA3 region of the hippocampus and likely modulates synaptic plasticity by the phosphorylation of synapsin I (Vara *et al.*, 2009). Phosphorylation of synapsin I has been linked to the regulation of the synaptic vesicle availability (Greengard *et al.*, 1993). Thus, ERK most likely controls the availability of synaptic vesicles during synaptic plasticity.

Another kinase involved in synaptic plasticity is the cyclin-dependent kinase 5 (CDK5) (Guan *et al.*, 2011). Impaired synaptic plasticity was demonstrated in CDK5 mutant mice as well as a reorganization of the protein composition. The importance of CDK5 for neurotransmitter release and presynaptic plasticity was highlighted by the identification of N-type voltage-gated calcium channels as a substrate of CDK5 (Su *et al.*, 2012). The phosphorylation alters the interaction with RIM1 and increases the number of docked vesicles.

Recent studies showed that the phosphorylation status of presynaptic AZ proteins is regulated upon depolarization, while postsynaptic proteins exhibited only a moderate regulation (Kohansal-Nodehi *et al.*, 2016; Engholm-Keller *et al.*, 2019). Bassoon is

the major target in the AZ harboring eight of the top 100 regulated phosphorylation sites (Engholm-Keller *et al.*, 2019). Taking the protein in length into account, RIM1 is one of the proteins with the highest number of regulated phosphorylation sites. A specific site of RIM1 involved in synaptic plasticity, however, and which kinase regulates it, remains enigmatic.

2.5 Serine-Arginine Protein Kinase 2 (SRPK2)

2.5.1 The SRPK family

The Serine-Arginine Protein Kinase (SRPK) family has been intensively studied for its role in phosphorylating serine/arginine-rich (SR) proteins to mediate splicing. Defects in alternative splicing have been linked to various human diseases such as cancer or spinal muscular atrophy (Faustino and Cooper, 2003; Venables, 2006; Tazi *et* al., 2009). The first member of the SRPK family (SRPK1) was identified in 1994 (Gui *et al.*, 1994). SRPK1 is highly expressed in the pancreas and specifically phosphorylates serine but not threonine (Gui *et al.*, 1994; Wang *et al.*, 1998). The second member of the SRPK family (SRPK2) exhibits the highest expression in the brain (Wang *et al.*, 1998), while the third member (SRPK3) is predominantly present in muscles (Nakagawa *et al.*, 2005).

2.5.2 Structure of SR protein kinases

Human SRPK2 consists of 688 amino acids. Two kinase domains are separated by a large spacer sequence. SRPK2 and SRPK1 share a 77% identity over the kinase domains (Wang *et al.*, 1998). The spacer sequence is a common feature of tyrosine but not serine/threonine kinases (Hanks and Quinn, 1991). Deletion of the spacer region in a SRPK family member in fission yeast, Dsk1, caused a change of Dsk1 localization (Takeuchi and Yanagida, 1993). Similarly, deletion of the spacer sequence in SRPK1 resulted in an exclusive nuclear instead of a nuclear-cytoplasmic localization (Ding *et al.*, 2006). Thus, the spacer sequence seems to be important for protein localization. The N-terminus of SRPK2 reveals a proline-rich sequence with a binding consensus core for Src Homology 3 (SH3) domain-containing proteins (Wang *et al.*, 1998).

2.5.3 SRPK2 in mammals

The majority of studies about SRPKs were investigating the role of SRPKs in phosphorylating SR-proteins. However, SRPK2 has been studied in different diseases in mammals. In many cancer studies it was shown that SRPK2 expression is increased (Gout *et al.*, 2012; Zhuo *et al.*, 2018). In mammals, the microtubule associated protein Tau, which stabilizes microtubules, was identified as a target of SRPK2 (Hong *et al.*, 2012). Tau phosphorylation resulted in impaired microtubule polymerization. Moreover, SRPK2 activates a delta-secretase, asparaginyl endopeptidase (AEP), which cleaves both tau and Aβ precursor protein (APP) and has an increased activity in Alzheimer's disease brains and aged mice (Wang *et al.*, 2017). Depletion of SRPK2 in the dentate gyrus improved learning and memory in Alzheimer's APP/PS1 mice indicating a role of SRPK2 in synaptic plasticity (Hong *et al.*, 2012).

2.5.4 SRPK2 homologue in *Drosophila melanogaster*: SRPK79D

To identify proteins involved in AZ formation in the *Drosophila melanogaster* neuromuscular junction (NMJ), a forward genetic screen was conducted. A P-element insertion was identified that resulted in large accumulations of Bruchpilot in peripheral axons (Johnson *et al.,* 2009; Nieratschker *et al.*, 2009). The identified gene is a member of the SRPK family and is called SRPK79D as it lies on band 79D of chromosome 3L. The kinase domain of *Drosophila melanogaster* SRPK79D and human SRPK2 show a 54% identity. Consistently, Nieratschker and colleagues showed that SRPK79D is a SR protein kinase due to phosphorylation of a SR protein peptide *in vitro* (Nieratschker *et al.*, 2009). SRPK79D did not change the turnover of Bruchpilot as the overall protein levels were unchanged in immunohistochemistry and immunoblots (Johnson *et al.,* 2009). Mutations of SRPK79D lead to accumulation of Bruchpilot and its depletion from the synapse. The number and growth of synapses, however, was not altered by SRPK79D (Johnson *et al.,* 2009; Nieratschker *et al.*, 2009). To further characterize the interaction between Bruchpilot and SRKP79D, *in* vitro phosphorylation assays were performed and Bruchpilot was identified as a substrate of SRPK79D (Driller *et al.*, 2019). The kinase activity of SRPK79D is required to prevent axonal accumulation of Bruchpilot but not for the colocalization of

both proteins (Johnson *et al.,* 2009). Therefore, the interaction does not seem to depend on the phosphorylation of Bruchpilot but the phosphorylation regulates most likely the transport of Bruchpilot to the synapse. Perturbed AZ structures after the overexpression of SRPK79D indicate correlation between the phosphorylation of Bruchpilot by SRPK79D and the transport to the synapse (Johnson *et al.,* 2009).
Presynaptic homeostatic potentiation has been shown to induce AZ remodeling dependent on RIM and other AZ proteins in *Drosophila melanogaster* (Müller *et al.*, 2012; Müller, Genc and Davis, 2015; Bruckner *et al.*, 2017; Böhme *et al.*, 2019). AZ remodeling was abolished in SRPK79D mutants and fewer Bruchpilot and Unc13A clusters were observed pointing to an important role of SRPK79D in AZ organization in *Drosophila melanogaster* (Böhme *et al.*, 2019). All in all, the data from *Drosophila melanogaster* raise the question about a role of SRPK2 in the organization of the active zone ultrastructure and synaptic plasticity in mammalian synapses.

2.6 The synaptic proteome

Highly specialized proteins mediate the communication between different synapses in our brain. To unravel the molecular composition that mediates synaptic transmission, researchers made major progress using sensitive mass spectrometry proteomic analyses of synapses. Therefore, synaptosomes were prepared because they contain nerve-ending terminals in which the presynapse is still tethered to the postsynapse building up a new vesicular structure (Whittaker *et al.*, 1964). Synaptosomes were used to define the overall synapse composition. Mass spectrometry revealed between 1131 to 2980 unique proteins of the synaptosome proteome (Schrimpf *et al.*, 2005; Filiou *et al.*, 2010). The proteome includes 118 synaptosomal phosphoproteins (Filiou *et al.*, 2010). Proteins of the cytomatrix of the active zone like bassoon, piccolo, RIM, liprin-α and ELKS (protein rich in the amino acids E (glutamic acid), L (leucine), K (lysine), S (serine)) were found in multiple studies (Boyken *et al.*, 2013; Weingarten *et al.*, 2014). Additionally, the proteomic characteristics between glutamatergic and GABAergic synapses were evaluated (Boyken *et al.*, 2013). However, only small differences between them were detected while most proteins of the docked synaptic vesicle fraction were similar (85%). Calcium/calmodulin-dependent protein kinase type II alpha subunit (CAMKIIα) and

the AZ protein bassoon were among the proteins enriched at excitatory synapses. In contrast, no differences between glutamatergic and GABAergic synapses were observed for Piccolo or Munc13 (Boyken *et al.*, 2013).
The proteome of synaptic vesicles was identified by Takamori and colleagues. They showed that Synaptobrevin/VAMP2 is the most abundant protein with 69.8 copies per vesicle, while 31.5 synaptophysin proteins and 8.3 synapsin proteins are present per vesicle (Takamori *et al.*, 2006).
However, all these studies lack the identification of the proteome of specific synapse types. The different characteristics of synapses like the expression of a presynaptic LTP in MF and cerebellar fibers (Zalutsky and Nicoll, 1990; Salin *et al.*, 1996; Linden and Ahn, 1999) compared to the postsynaptic LTP in Schaffer collateral synapses (Tsien *et al.*, 1996) point to a distinct synapse composition to facilitate the respective properties. All proteomic studies so far were based on a mixture of synapse types. Therefore, the identified proteomes can not be linked to a specific synapse type to explain its unique features. The isolation of the synapse types of interest would allow determining their proteomes and gaining more insights about the properties of the respective synapses.

2.7 The presynaptic active zone

The arrival of an action potential initiates a signaling cascade at the presynaptic terminal that results in the fusion of synaptic vesicles with the plasma membrane and the release of neurotransmitter. These events rely on the highly organized structure at the presynaptic terminal: the active zone (AZ). The AZ consists of a highly specialized network of different proteins also known as the cytomatrix at the active zone (CAZ) (Schoch and Gundelfinger, 2006; Südhof, 2012). At the CAZ, specialized proteins mediate the docking and fusion with the subsequent neurotransmitter release in a temporally and spatially controlled manner (Schoch and Gundelfinger, 2006). Proteins associated with the CAZ can be distinguished into proteins mediating synaptic vesicle fusion, scaffolding proteins, VGCCs, cell adhesion molecules (LAR-RPTPs: Leukocyte common antigen-related receptor protein tyrosine phosphatases) and cytoskeletal proteins (Schoch and Gundelfinger, 2006; Südhof, 2012). The structure of the AZ reflects the functional properties of a synapse type. A higher

number of AZ proteins like RIM1 or presynaptic calcium channels is associated with a larger AZ area (Holderith *et al.*, 2012). Moreover, the AZ size correlates with the release probability and thereby determines synaptic strength (Matz *et al.*, 2010; Holderith *et al.*, 2012). Many proteins involved in the release machinery are evolutionary conserved. Synaptotagmin1, RIM, RIM-BP, calcium channels, ELKS, α-liprins and Munc13 are found in vertebrates and invertebrates. RIM, RIM-BP, ELKS, bassoon, piccolo and Munc13 are scaffold proteins that connect the molecular release machinery at the AZ. RIM binds VGCCs as well as Rab3 and thereby brings synaptic vesicles in close proximity to Ca^{2+} ions (Kaeser *et al.*, 2011). Munc13 homodimerizes via the N-terminal C2 domain (Dulubova *et al.*, 2005) defining the inactive state. Disruption is achieved by binding to RIM1 leading to the activation of Munc13 and its ability to prime synaptic vesicles (Lu *et al.*, 2006). α-liprins are regulating the AZ size in both *C. elegans* and *Drosophila melanogaster* and are expressed by one gene (Dliprin-α in *Drosophila melanogaster* and syd-2 in *C. elegans*) (Zhen and Jin, 1999; Kaufmann *et al.*, 2002). In contrast, four genes are encoding for α-liprins in vertebrates (α1, α2, α3, α4) (Serra-Pages *et al.*, 1998). However, no similar function could be identified in vertebrates. Bassoon is important for normal transmission and its deletion results in spontaneous epileptic seizures (Altrock *et al.*, 2003). The interaction of bassoon with RIM-BP localizes P/Q-type Ca^{2+} channels to release sites (Davydova *et al.*, 2014).

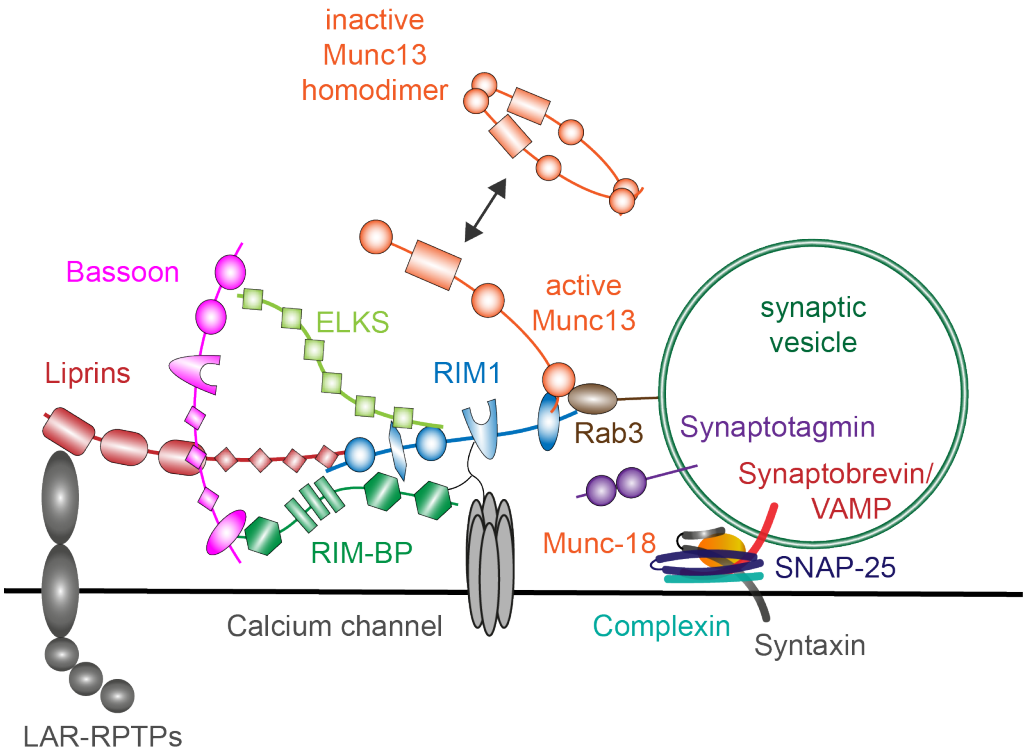

Figure 2.3: Organization of the presynaptic AZ.

The AZ consists of a highly specialized network of proteins. Schematic overview of AZ proteins and their interactions with the release machinery. Adapted from (Südhof, 2012).

2.8 The nanoorganization of the active zone

The organization of the AZ has been studied for a long time and the key components have been characterized. The small size of an AZ of approximately 250 nm limited the investigation of the ultrastructure of the AZ. Superresolution enabled the investigation of the AZ at individual synapses demonstrating that RIM1 is localized ~35 nm apart from the presynaptic membrane and within 40-50 nm distance to VGCCs, consistent with the role of tethering synaptic vesicles (Dani *et al.*, 2010; Glebov *et al.*, 2017). RIM1 clusters were trans-synaptically aligned to postsynaptic clusters of PSD-95 (Tang *et al.*, 2016). A comparable number of nanoclusters per synapse were found for RIM1 (2 clusters) and bassoon (1.5 clusters) (Tang *et al.*, 2016), while different studies found a higher number of Munc13 clusters per synapse (2-5 clusters) (Tang *et al.*, 2016; Sakamoto *et al.*, 2018). In contrast to RIM1, bassoon displays a higher distance to VGCCs (~70 nm) (Dani *et al.*, 2010). In addition, several scaffold proteins such as piccolo, bassoon, Munc13, RIM-BP2 are

found within a 50-100 nm distance to the synaptic cleft (Dani *et al.*, 2010; Grauel *et al.*, 2016).

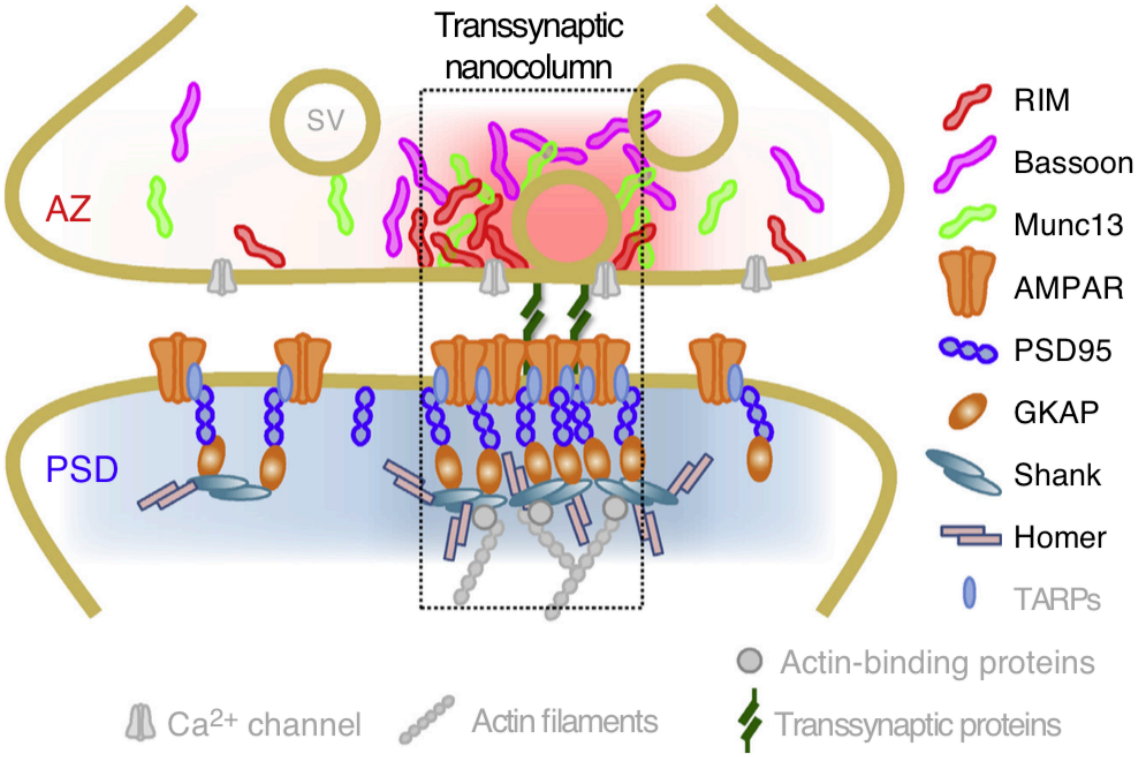

Figure 2.4: Transsynaptic nanocolumns.

Key presynaptic proteins like RIM1/2 and Munc13 mediate the vesicle fusion and form transsynaptic nanocolumns with postsynaptic nanoclusters. The positioning of color-coded proteins has been confirmed in contrast to the grey-colored proteins (Chen, Tang and Blanpied, 2018).

Neuronal activity regulates the architecture of the synapse. Long-term potentiation increased PSD-95 density within the PSD-95 nanocluster while depression reduced number, volume and protein density. In contrast, RIM1 cluster number was not affected in either activity change (Tang *et al.*, 2016).

Homeostatic plasticity induction by TTX treatment had no effect on the number of bassoon clusters but decreased the cluster area (Glebov *et al.*, 2017). Similarly to bassoon, no change for RIM localizations per AZ was observed while $Ca_V2.1$ clusters were increased (Glebov *et al.*, 2017). All this data points to a highly dynamic structural organization at the AZ. However, further studies are necessary to reveal exact mechanisms that regulate the dynamic processes of neurotransmitter release.

3. Aims of the study

Synapses are able to adjust their structure and efficacy in neurotransmitter release in order to maintain neuronal activity within a physiological range. The ability to dynamically weaken or strengthen synaptic transmission is called synaptic plasticity. Whereas the molecular machinery regulating the release of synaptic vesicles is well studied, the mechanisms underlying synaptic plasticity are still not fully understood. The importance of posttranslational modifications, in particular phosphorylation has been proposed during neuronal activity. Additionally, it has been suggested that presynaptic properties are impacted by the specific composition of the release machinery.

In this thesis we will address these two aspects by pursuing the following two aims:

The first aim is to investigate the role of phosphorylation in synaptic plasticity. Therefore, we will examine the role of a kinase, the Serine-Arginine Protein Kinase 2 (SRPK2), which in *Drosophila melanogaster* has been linked to synaptic plasticity, with regard to its impact on the ultrastructure and function of the mammalian presynapse. We aim to determine the phosphoproteome of SRPK2 in order to identify its downstream effectors. In addition, superresolution microscopy will identify if SRPK2 plays a role in the organization of the active zone ultrastructure.

Our second aim is to identify for the first time a neuron-type specific proteome. To link the presynaptic proteome to its synaptic properties, we will characterize the proteome of two synapses with distinct forms of presynaptic plasticity. Accordingly, we will need to establish an approach to isolate the proteome of the two synapses of interest. Using mass spectrometry, we will be able to identify the proteome of both synapses and highlight differences in the protein composition.

Taken together, this study will provide new insights into the role of phosphorylation as well as of the presynaptic composition in synaptic plasticity to better understand the underlying molecular mechanisms how synapses are able to regulate their synaptic strength.

4. Methods

4.1 Molecular biology

4.1.1 Polymerase chain reaction (PCR)

To amplify the DNA fragment of interest, the following protocol and reagents were mixed for the polymerase chain reaction (PCR) (Table 4.1). The Phusion High-Fidelity DNA Polymerase (Thermo Fisher Scientific) was used to amplify the DNA.

Components	Volume
5X HF buffer	10 µl
5’ Primer (10 pmol/µl)	2.5 µl
3’ Primer (10 pmol/µl)	2.5 µl
dNTP-Mix (25 mM)	1 µl
Template DNA	100 ng
Polymerase	0.8 µl
H_2O	ad 50 µl

Table 4.1: PCR protocol

The reaction was performed in a thermocycler (Bio-Rad). Different temperature steps were used to amplify the DNA fragment with 35 cycles of Steps 2 - 4 (Table 4.2).

Step	Temperature	Time
Step 1: Initial Denaturation	98°C	30 sec
Step 2: Denaturation	95°C	10 sec
Step 3: Annealing	50-60°C	30 sec
Step 4: Extension	72°C	15-30 sec/kb
Step 5: Final extension	72°C	10 min

Table 4.2: PCR program

4.1.2. Sequencing

To verify successful generation of the plasmid of interest, 100 ng of plasmid were sent to Eurofins Genomics with 2 µl of the primer (10 pmol/µl) that was used to sequence.

4.1.3 Oligonucleotide cloning

Oligonucleotides with a length of 13-15 amino acids (aa) were designed to contain the sequence of interest with the target serine at P0 position. On the N-terminus a site for EcoRI and on the C-terminus a stop codon and a site for SalI were incorporated. Custom generated oligonucleotides arrived lyophilized and were dissolved in MilliQ water to achieve a concentration of 100 µM. To anneal the oligonucleotides 3 µl of each oligonucleotide was added to 12 µl H_2O and 2 µl 10X annealing buffer (10 mM Tris-HCl (Roth), 50 mM NaCl (Roth), 1 mM ethylenediaminetetraacetic acid (EDTA, Roth)). The reaction was incubated for 10 min at 95°C. Afterwards, samples were cooled down in the device. Successful annealing was confirmed with 1 µl of annealed oligonucleotides using a 3% agarose gel. To phosphorylate the annealed oligonucleotides, 1 µl was added to 1 µl polynucleotide kinase (PNK), 2 µl 10X T4 buffer and 16 µl H_2O and incubated for 30 min at 37°C. Deactivation of the kinase was performed subsequently for 5 min at 65°C. The target vector (pGEX) was digested with EcoRI and SalI for 2 h at 37°C. The vector was dephosphorylated by adding 1 µl FastAP per digest sample and was subsequently incubated for 20 min at 37°C. The digestion of the vector was confirmed on a 1% agarose gel. The digested vector was cut out using UV illumination and purified using the NucleoSpin® Gel and PCR Clean-up kit (Macherey-Nagel) following the manufacture's instruction. For the ligation reaction, vector and oligonucleotides were used in a molecular ratio of 1:3 using the T4 ligase (Thermo Fisher Scientific). After 1 h at 37°C, 5 µl of ligation product were used for transformation as described in section 4.1.4.

4.1.4 Transformation of bacteria

To transform the plasmid of interest, 50 µl of Stellar or BL21 cells were thawed on ice. For a re-transformation 1 µg DNA and for a ligation product 5 µl were added to the bacteria and incubated for 20 min on ice. A heat shock was performed at 42°C for

42 sec. The bacteria were subsequently placed on ice for 2 min before the addition of 150 µl of LB medium for BL21 or SOC medium for Stellar cells. Bacteria were incubated for 1 h at 37°C in a thermo shaker. Afterwards, bacteria were plated on an agar-plate supplemented with the respective antibiotic and incubated at 37°C overnight.

4.1.5 Bacteria culture

To cultivate bacteria expressing the plasmid of interest, a single colony grown on an agar plate or 400 µl of a glycerol stock was added to LB medium and was incubated overnight at 37°C with 180 rpm. For long-term storage, a glycerol stock consisting of 50% bacteria culture and 50% glycerol (50% (v/v) in H_2O) was kept at -80°C.

4.1.6 DNA plasmid purification

Purification of plasmid DNA was achieved using commercial kits following the manufacturer's instructions. Plasmids that were used for virus production or transfections of primary neurons were purified using the endotoxin-free maxi kit (Qiagen).

4.1.7 Messenger RNA (mRNA) isolation and cDNA synthesis

Neuronal cultures were seeded at a density of 75,000 cells per 24-well or 300,000 cells per 6-well. The plates were briefly washed with phosphate buffered saline (PBS) and then 50 µl or 250 µl of lysis buffer from the Dynabeads® mRNA DIRECT™ Micro Purification Kit (Life Technologies) was transferred onto the cells. Cells were immediately stored at -80°C. The mRNA was isolated following the manufacturer's instruction. To synthesize the cDNA from the purified mRNA by reverse transcription, the Revert AidH Minus First Strand cDNA Synthesis Kit (Thermo Fisher Scientific) was used and the manufacturer's instructions were followed.

4.1.8 Real time PCR

For quantitative real time PCR the Maxima SYBR Green/ROX qPCR Mix (ThermoFisher) was used and the following components were mixed for one replicate:

Components	Volume
2X Master mix	3.125 µl
5' Primer (10 pmol/µl)	0.1875 µl
3' Primer (10 pmol/µl)	0.1875 µl
DEPC - water	1.5 µl

Table 4.3: Real time PCR protocol

In total three to four technical replicates for each biological replicate were performed. The following PCR protocol with 40 cycles of steps 2-4 was used:

Step	Temperature	Time
1	95°C	10 min
2	95°C	15 sec
3	59°C	60 sec
4	72°C	40 sec
5	4°C	∞

Table 4.4: Real time PCR program

To evaluate the gene expression differences between treatments, β-actin was used as an internal reference. The gene expression was calculated as $2^{-\Delta ct}$ with:

Δct (cycle threshold value) = ct of analyzed gene – ct of β-actin.

4.2 Cell culture

4.2.1 HEK293T cell culture

Human embryonic kidney-293 cells (HEK293T) were cultivated using Dulbecco's Modified Eagle's Medium (DMEM) (Life Technologies) supplemented with 1% penicillin/streptomycin (Life Technologies) and 10% fetal calf serum (FCS) (Life Technologies) in a humidified incubator at 37°C with 5% CO_2. Every 2-3 days the cells were splitted.

4.2.2. Transfection of HEK293T cells

HEK293T cells were seeded with a density of 1.5 x 10^6 cells/10 cm dish. After 24 h, DMEM medium was removed and cells were incubated with Iscove's Modified Dulbecco's Medium (IMDM), supplemented with 5% FCS. For transfection 2X HEBS and 2.5 mM $CaCl_2$ were used as indicated in Table 4.5.

Components	Amounts
dH_2O	1.1 ml
$CaCl_2$ (2.5 M)	145 µl
DNA plasmid	4-5 µg
2X HEBS (pH 7.05)	1.6 ml

Table 4.5: Transfection protocol

As the last ingredient, 2X HEBS was added in a drop-wise manner under vortexing. The transfection mixture was incubated for 2 min to allow complex formation before addition to the HEK293T cells. The IMDM medium containing the precipitate was removed 24 h after the transfection and replaced with DMEM medium.

4.2.3 rAAV serotype 1/2 production

HEK293T cells were seeded and transfected as described in 4.2.2. The transfection was based on the Ca^{2+}-phosphate method but included more components to produce recombinant adeno-associated virus (rAAV) serotype 1/2.

Components	Amounts
dH_2O	1.1 ml
$CaCl_2$ (2.5 M)	145 µl
AAV plasmid	5.5 µg
pFdelta6 – *helper virus*	11 µg
pNLrep / pRV1 – serotype 1	2.75 µg
pH21 – serotype 2	2.75 µg
2X HEBS (pH 7.05)	1.6 ml

Table 4.6: Transfection mixture for rAAV serotype 1/2 production

To harvest the virus, the medium was removed 48 h post transfection and 1 ml DMEM (including 5% penicillin/streptomycin, 10% FCS) was added. Cells were scraped off and suspension was frozen at -80°C. To break off cells, suspension was thawed at 37°C and refrozen at -80°C. After three freeze-thaw cycles, suspension was centrifuged for 10 min at 14,000 rpm and virus-containing supernatant was stored at 4°C.

4.2.4 Preparation of neuronal cultures

Mouse hippocampal and cortical neurons were cultured from embryonic mice (E16-18) as previously described (Zürner *et al.*, 2011). In brief, hippocampus or cortex was dissected from the embryonic mice, washed several times with Hank's Buffered Salt Solution (HBSS, Life Technologies) and subsequently digested with trypsine (Life Technologies) for 20 min at 37°C (0.025 g/ml, Life Technologies). After several washing steps with HBSS (Thermo Fisher), the remaining DNA was digested with DNase I (0.001 g/ml, Roche). Cannulas were used to dissociate the tissue and the suspension was passed through a Nylon cell strainer (100 µm, BD Biosciences). Cells were seeded in a 12 or 24-well plate on glass coverslips coated with poly-D-lysine at a density of 25,000 cells per 24-well or 30,000 cells per 12-well. For proteomic analysis, cells were plated in a 6-well plate with 300,000 cells per well. All cells were cultured in basal medium eagle (BME, Life Technologies) supplemented with 0.5% glucose (Sigma-Aldrich), 10% FCS (Life Technologies), 2% B-27 and 0.5 mM L-glutamine (Life Technologies). Cells were maintained at 37°C in 5% CO_2 until use.

4.2.5 Transfection of neuronal cultures

4.2.5.1 Ca^{2+} phosphate method

Neuronal cultures with a density of 3 x 10^4 cells/12-well dish were transfected at DIV2-6 following the protocol of Köhrmann et al. (Köhrmann *et al.*, 1999). Briefly, cells were incubated with pre-warmed Minimum Essential Medium (MEM) (Life Technologies) for 1 h prior to infection. The original medium was kept and incubated at 37°C during the transfection. For the transfection, 5 µg of endofree plasmid per well was used and added to 60 µl $CaCl_2$. Neurons were incubated for 30-60 min at 37°C before precipitate was removed by two washing steps with HBSS and two

washing steps with BME medium. BME medium was removed and replaced the original medium. Transfected neurons were further cultivated at 37°C and 5% CO_2.

4.2.5.2 Lipofectamine method

Prior to transfection, BME medium of the primary neurons was removed and stored at 37°C. Neurons were incubated with Opti-MEM (Life Technologies) for 30 min at 37°C with 5% CO_2. Plasmid and lipofectamine2000 (Life Technologies) were diluted in Opti-MEM. Lipofectamine dilution was added to the diluted plasmid in a drop-wise fashion under vortexing. The solution was incubated for 20 min at room temperature (RT) and subsequently added to the neurons. After 2 h, the Opti-MEM medium was removed and neurons were washed twice with fresh Opti-MEM before being further cultivated in the original BME medium.

4.2.6 Transduction of neuronal cultures with rAAV

Primary neurons were transduced at DIV2-6 with crude or purified viral particle extracts (rAAV serotype 1/2). To infect cells with crude viral particle extracts, 5 µl were used per 24-well plate. For purified viral particles 1-2 µl of virus suspension were used per 24-well or 5 µl per 6-well. Transduced neurons were further cultivated at 37°C and 5% CO_2.

4.2.7 Pre-treatment of primary neurons and HEK293T cells with various drugs

Mouse primary neurons were silenced with 1 µM tetrodotoxin (TTX) (Tocris) at DIV12/13. After 48 h neurons were directly fixed with 4% paraformaldehyde (PFA) without washing or lysed for immunoblotting (IB) (see section 4.3.7.). To block the proteasome, neurons or HEK293T cells were incubated with 10 µM lactacystin (Sigma-Aldrich) or 10 µM MG-132 (Sigma-Aldrich) for 6 h. Translation was blocked for 6 h using 50 µM emetine (Roth) or 50 µg/ml cycloheximide (Roth). Afterwards, neurons were lysed and analyzed using immunoblots. Control neurons were incubated in unsupplemented media.

4.3 Biochemical methods

4.3.1 Preparation of whole brain homogenates

Wild-type (WT) mice were decapitated and the whole brain homogenate was removed. The brain was transferred into an eppendorf tube and immediately frozen in liquid nitrogen. The frozen brain was weighted and subsequently homogenized with PBS containing proteinase inhibitor (Millipore) (2 ml per 100 mg brain) using a rotor stator (Kinematica). Homogenates were denatured with Laemmli buffer at 95°C for 5 min. After denaturation, homogenates were sonicated 5 x 10 sec. Samples were analyzed using immunoblots or stored at -20°C.

4.3.2 Subcellular fractionation

Synaptosomes were prepared from whole brain homogenates. Therefore, the wild-type brain was homogenized in homogenization buffer (0.32 M sucrose (Roth), 4 mM 4-(2-hydroxyethyl)-1-piperazineethanesulfonic acid (HEPES, Roth), proteinase inhibitor (Millipore)) in a glass potter using a Teflon pestle. After 12 strokes at 900 rpm, the homogenate was centrifuged for 15 min at 3,000 x g. The first pellet (P1) was discarded and the supernatant 1 (S1) was centrifuged for 25 min at 4500 rpm. The cytosolic proteins in the supernatant (S2) were kept for immunoblot analysis and pelleted crude synaptosomes (P2) were resuspended in 10 mM HEPES with 1% Triton X-100 (Sigma-Aldrich) and protease inhibitor (Protease Inhibitor Cocktail Set III, EDTA-free, Millipore, 1:1000) and lysed for 1 h at 4°C. Afterwards, the lysed crude synaptosomes were centrifuged for 30 min at 50,000 x g. Cytosolic synaptic proteins (S3) were kept for immunoblot analysis and the synaptic plasma membrane fraction (P3) was resuspended in 10 mM HEPES with 1% Triton X-100 and proteinase inhibitor. After 1 h at 4°C, centrifugation at 50,000 x g at 4°C separated the TX-100 resistant synaptic membrane fraction (P4) and the TX-100 soluble fraction (S4). Samples were denatured with Laemmli buffer at 95°C for 5 min and analyzed using immunoblots.

4.3.3 Preparation of synaptosomes

4.3.3.1 Preparation of synaptosomes from primary neurons

Primary cortical neurons, cultured in a 6-well plate, were washed once with PBS. After removal of PBS, neurons were scraped off in 500 µl of homogenization buffer (0.32 M sucrose, 4 mM HEPES, proteinase inhibitor). The solution was filtered through a filter with a pore size of 5 µm (Millipore) and subsequently centrifuged for 15 min at 3500 rpm and 4°C. The pellet contained crude synaptosomes and was denatured with Laemmli buffer for 5 min at 95°C to analyze the samples by immunoblots.

4.3.3.2 Preparation of crude synaptosomes from mice

Wild-type mice were sacrificed and the cerebellum was quickly removed. The forebrain was cut into 4 pieces and transferred into a potter containing 2.5 ml of homogenization buffer (0.32 M sucrose, 4 mM HEPES, proteinase inhibitor). Brains were homogenized by 12 strokes at 900 rpm with a teflon pestle. The homogenate was transferred into a fresh falcon tube. To collect residual homogenate, 2 ml fresh homogenization buffer was transferred into the potter and 3 strokes were performed with the pestle. The homogenization buffer was added to the first homogenate fraction. The potter was rinsed with 2 ml fresh buffer as a last cleaning step. All three fractions were pooled and centrifuged at 3,000 x g for 15 min. Pellet 1 (P1), containing blood vessels and cellular nuclei, was discarded and supernatant 1 (S1) was centrifuged for additional 25 min at 17,500 x g. Supernatant 2 was discarded and pellet 2 (P2), representing crude synaptosomes, was collected.

4.3.3.3 Tissue homogenization and synaptosome fractionation for fluorescence activated synaptosome sorting

Wild-type or NG2CreER:PSD95mVenus mice were sacrificed and the cerebellum was quickly removed. Homogenization was performed as described in 4.3.3.2. Homogenate was centrifuged at 1,000 x g for 8 min at 4°C. Pellet 1 was discarded and the supernatant was transferred into new tubes and centrifuged at 12,000 x g for 13 min at 4°C. The supernatant 2 was discarded and pellet 2 was resuspended in 1 ml homogenization buffer (0.32 M sucrose, 4 mM HEPES pH 7.4). A sucrose gradient was prepared with filtered 1.2 M sucrose, 4 mM HEPES pH 7.4 on the

bottom and filtered 0.8 M sucrose, 4 mM HEPES pH 7.4 on top. The resuspended pellet 2 was added on top of the sucrose gradient. The gradient was centrifuged at 50,000 x g for 70 min at 4°C with the ultracentrifuge swinging rotor (TH-641, Beckman-Coulter). The acceleration was set at 6 and deceleration at 4. Synaptosomes were collected at the interface of the two sucrose phases with a 25G needle by piercing through the centrifuge tube. Synaptosomes were diluted 1:200 with ice-cold PBS supplemented with proteinase inhibitor and stored on ice until used for synaptosome sorting.

4.3.4 Protein-protein interaction assays

4.3.4.1 Protein induction and purification from *BL21* bacteria

BL21 *Escherichia coli* were transformed with the plasmid coding for the protein of interest fused to glutathione-s-transferase (GST). Bacterial cultures were grown until an optical density (OD) of 0.5 – 0.7 was reached. Protein expression was induced by 1 mM isopropyl-β-D-thiogalactopyranosid (IPTG) (Roth) for 4 h at 37°C with 180 rpm. Bacteria were pelleted by centrifugation at 4,500 rpm for 30 min at 4°C. The pellet was resuspended in PBS and the centrifugation step was repeated. The pellet was either stored at -80°C or directly lysed by resuspension in PBS in the presence of lysozyme (1 mg/ml) and proteinase inhibitor and incubation on ice for 20 min. Bacterial suspension was sonicated 5 x 10 sec and subsequently centrifuged at 4,500 rpm for 1 h at 4°C. The supernatant was transferred to glutathione-agarose beads (Sigma Aldrich) and incubated for 1 h at 4°C to purify the protein of interest. Glutathione-agarose beads were washed twice with PBS supplemented with proteinase inhibitor. In the final step, a 50:50 ratio of bead:PBS was prepared and beads containing the protein of interest were stored at 4°C. To verify the successful purification, a sodium dodecyl sulfate polyacrylamide gel electrophoresis (SDS-PAGE) gel was prepared and stained with Coomassie to analyze the purification as well as the concentration of the samples.

4.3.4.2 Immunoprecipitation (IP) and pull down of synaptic proteins

HEK293T cells were transfected with SRPK2-HA, SRPK2-GFP or SRPK2-kinase dead-GFP as described above (4.2.2) and harvested 48 h after transfection. Medium

was removed, and cells were washed once with PBS. After removal of PBS, cells were scraped off in 300 µl ice-cold lysis buffer (50 mM HEPES pH 7.4, 150 mM NaCl, 1% Triton X-100, proteinase inhibitor (Protease Inhibitor Cocktail Set III, EDTA-free, Millipore, 1:1000)) per 10 cm dish and lysed for 1 h at 4°C. Cell debris was spun down at 17,500 x g for 10 min at 4°C. Meanwhile, beads with the respective tag of the protein of interest (HA- (Life Technolgies) or GFP-magnetic beads (ChromoTek)) were washed twice with ice cold lysis buffer. Cell lysate was collected and transferred to magnetic beads for immunoprecipitation. After 4 h of incubation, beads were washed twice with low salt buffer (50 mM HEPES pH 7.4, 100 mM NaCl, 0.5% Triton X-100), twice with high salt buffer (50 mM HEPES pH 7.4, 500 mM NaCl, 0.5% Triton X-100), twice with low salt buffer and twice with PBS.

To analyze synaptic binding partners, synaptosomes were prepared from mouse brains as explained in section 4.3.3.2. Crude synaptosomes (P2) were lysed in CL114 lysis buffer (Logopharm) supplemented with proteinase inhibitor at 4°C. After 1 h, synaptosomes were centrifuged for 25 min at 17,500 x g at 4°C. The supernatant, containing the synaptic proteins, was incubated with immunoprecipitated SRPK2 or HA/GFP alone as a control for 4 h at 4°C. Afterwards, beads were washed five times with CL114 dilution buffer. Proteins were boiled in Laemmli buffer with β-mercaptoethanol for 5 min at 95°C. Binding of proteins was analyzed by immunoblots.

4.3.5 *In vitro* phosphorylation

4.3.5.1 Radiometric *in vitro* phosphorylation

Purified GST-fusion proteins were incubated with 500 ng purified SRPK2 and 1 mM ATP in kinase reaction buffer III (SignalChem) for 30 min at 30°C. The reaction was stopped by the addition of 10 µl 4X SDS sample buffer (200 mM Tris-HCl (pH 6.8) (Roth), 400 mM DTT (Thermo Fisher), 8% SDS (Roth), 0.4% bromophenol blue (Sigma Aldrich), 40% glycerol (Invitrogen)). Samples were transferred on a nitrocellulose membrane (GE Healthcare Life Sciences) and washed 3 times with 0.75% phosphoric acid (Sigma-Aldrich). Successful phosphorylation was measured using the Liquid Scintillation Counter (Beckman-Coulter).

4.3.5.2 *In vitro* phosphorylation with subsequent mass-spectrometry analysis

Kinase reaction was conducted as described in 4.3.5.1. To stop the reaction, pelleted beads were washed three times with ice-cold washing solution (50 mM HEPES, pH 8.4). The beads were resuspended in 40 µl reduction buffer (10 mM Tris(2-carboxyethyl)phosphine hydrochloride (TCEP, Sigma-Aldrich), 50 mM HEPES, pH 8.4) and incubated for 10 min at 85°C and 600 rpm. After the tube was placed back at RT, iodoacetamide (IAA) (Sigma-Aldrich) was added to a final concentration of 20 mM. The reaction was incubated for 30 min at RT and away from light. Subsequently, 40 µl of reduction buffer was added. To digest the proteins of interest, trypsin was added to a achieve a 1:20 ratio of trypsin:protein and incubated at 37°C for 4 h. Afterwards, the same amount of trypsin was added and the samples were incubated again at 37°C for 4 h. The beads were pelleted by a short centrifugation step and supernatant was collected. 40 µl of washing solution was added to the beads. After pelleting, the supernatant was collected and pooled with the first supernatant. Samples were frozen on dry ice and lyophilized overnight at 0.1 mbar and -55°C.

4.3.6 Mass spectrometry

4.3.6.1 Mass spectrometry of primary neurons

Mouse cortical neurons were transduced at DIV2-6 with rAAV U6-GFP, shSRPK2-GFP, SRPK2-GFP and lysed at DIV14-16 (2% SDS, 50 mM Tris/HCl pH 7.4, 2 mM EGTA (Roth), 2 mM EDTA (Roth), Complete Protease Inhibitor Cocktail, 2 mM PMSF (Sigma-Aldrich), 5 mM NaF (Sigma-Aldrich), 2 mM beta-glycerophosphate (Sigma-Aldrich), Phosphatase inhibitor Cocktail 2 (1:1000), PhosSTOP (Roche)). Lysed cells were frozen on dry ice. After a heat shock at 85°C for 10 min, lysates were sonicated at maximum 3 times for 10 s. Samples were refrozen on dry ice before being lyophilized.

To each sample 100 µl of water containing 10 mM TCEP was added. The samples were heated at 85°C for 10 min. IAA was added to 20 mM and samples were kept at 22°C for 30 min. Samples were precipitated by the chloroform-methanol-water method (Wessel and Flugge, 1984) and air dried at 37°C for 1 h. Samples were dissolved in 24 µl 7.8 M Urea with 50 mM HEPES and 4 µg of Lysyl Endopeptidase (Fujifilm/Wako, Japan) at pH 8.0 (adjusted with NaOH) and heated at 25°C for 8 h.

Samples were diluted to 192 µl in HEPES/NaOH pH 8.0 and 4 µg of trypsin was added. The samples were incubated at 37°C for 4 h.

The amount of peptide in each sample was measured using the absorption of 280 nm light (Implen Nanophotometer, Labgear, Australia). An aliquot containing 100 µg of peptide was labeled with a tandem mass tag (TMT) 10-plex reagent (Thermo Fisher Scientific), according to the manufacturer's instructions. There were two separate TMT10plex schemes: (i) five control samples (U6-GFP) were compared to five overexpression (SRPK2-GFP) samples and (ii) five control samples (U6-GFP) were compared to five knock-down samples (shSRPK2-GFP). The two sets of 10 tagged samples were separately combined to produce two 10-plex sample mixtures. These were acidified with formic acid. The volume was reduced by vacuum concentration and then made up in 1 ml of water with 0.1% trifluoracetic acid. The two samples were each desalted using a Sep-Pak tC18 3cc Vac Cartridge (200 mg sorbent, Waters).

The sample's eluate volume was reduced and then made up in a solution of 1 M glycolic acid, 5% trifluoracetic acid and 80% acetonitrile and applied to the "TiSH" method of phosphopeptide enrichment and hydrophilic interaction chromatography fractionation as described in detail by Engholm-Keller et al. (Engholm-Keller and Larsen, 2016). This method first separates multi-site phosphopeptide from mono-phosphorylated peptides and then fractionates the mono-phosphopeptides. The hydrophilic interaction chromatography used a 5-µm TSKGel Amide 80 resin (Tosoh, Japan) column and was performed as described previously (Engholm-Keller *et al.*, 2019).

The peptides from each hydrophilic interaction chromatography fraction and the multi-phosphorylated peptides were resolved by reversed phase chromatography on a 300 × 0.075 mm column packed with ReproSil Pur C18 AQ 1.9 µm resin (Dr Maisch, Germany) using an Ultimate 3000 RSLC nano system (Thermo Scientific, Germany). The chromatography buffer A was 0.1% formic acid in water and buffer B was 0.1% formic acid, 90% acetonitrile and 9.99% water and the flow rate was 250 nl/min. The gradient was from 5% to 25% buffer B in 69 min, then to 35% buffer B in 8 min and to 99% buffer B in 3 min. The column temperature was held at 50°C by a column oven (PRSO-V1, Sonation lab solutions, Germany). Peptides were detected by tandem mass spectrometry using a Q Exactive Plus hybrid quadrupole-orbitrap mass spectrometer. The nanospray flex ion source (Thermo Scientific,

Germany) spray operated at 2.3 kV. The capillary temperature was 250°C and the S lens radio frequency level was 60. The MS scan was from m/z 375 to 1500 at a resolution of 70,000 full width at half maximum with an automatic gain control target of 1,000,000 counts for a maximum ion time of 100 ms. For each MS scan, up to 11 of the most intense ions above a threshold of 46,000 counts were selected for an MS/MS scan. MS/MS scans were at a resolution of 35,000 full width at half maximum for a maximum ion time of 120 ms and automatic gain control target of 20,000 counts. The isolation window was 1.2 m/z, the fixed first mass was 120 m/s and the normalized collision energy was 34. Peptides with charge state <2+, >8+ or with unassigned charge were excluded. Dynamic exclusion of previously scanned peptides was for 20 s.

An estimated 2 µg of the non-titanium dioxide binding (non-phosphorylated) peptides of each 10-plex sample mixture was also analyzed by LC-MS/MS. The settings were the same as for the phosphopeptides except for the following. The gradient was from 5% to 28% buffer B for 126 min, then to 35% buffer B in 10 min and to 99% buffer B in 3 min. Up to 12 of the most intense ions were selected for MS/MS above a threshold of 50,000 counts for a maximum ion time of 110 ms. Dynamic exclusion was of previously scanned peptides was for 30 s.

The raw LC-MS/MS data was processed with MaxQuant v1.5.8.3 (Tyanova *et al.*, 2016) using the following settings. The fasta file was the Mus musculus reference proteome downloaded from UniProtKB on July 18, 2017 and containing 60,205 entries including protein isoforms. The reference proteome was combined with the default contaminants file and a reversed sequence database was used to assess the false discovery rate. Protease specificity was Trypsin/P with up to 3 missed cleavages. Carbamidomethyl (C) was a fixed modification and the TMT10plex reagents were designated isobaric labels. Deamidation (N and Q), oxidation (M), acetylation (protein N-terminus) and phosphorylation (S, T and Y) were variable modifications. A maximum of 5 modifications per peptide was allowed. The minimum score for modified peptides was 40. The minimum peptide length was 6 and maximum peptide mass was 7,000 Da. The peptide spectrum match, protein and modification site false discovery rate was 1%. A dependent peptide search was performed with a 1% false discovery rate. Modified peptides and their counterparts on-modified peptides were excluded from protein quantification. A second peptide search was enabled. The tolerance for MS and MS/MS spectra was 4.5 ppm and

20 ppm, respectively. All other settings were left as the default within MaxQuant v1.5.8.3.

4.3.6.2 Mass spectrometry of *in vitro* phosphorylated RIM1

The lyophilized peptide in each sample was desalted using a StageTip (Rappsilber *et al.*, 2007). The samples were analyzed by LC-MS/MS using the same equipment as for mass spectrometry of neuronal samples. The settings were the same as for the neuronal phosphopeptides except for the following differences. The gradient was from 5% to 32% buffer B in 34 min, then to 99% buffer B in 2 min. Up to 12 of the most intense ions were selected for MS/MS above a threshold of 55,000 counts for a maximum ion time of 110 ms. The isolation window was 1.4 m/z. The first fixed mass was 140 m/z. The normalized collision energy was 30. Dynamic exclusion was of previously scanned peptides was for 25 s.

The MaxQuant processing was the same as the neuronal samples except for the following differences. The fasta file was the Rattus norvegicus reference proteome downloaded from UniProtKB on Feb 5, 2018, containing 29,975 entries of canonical protein isoforms. Match between runs was enabled with a matching time window of 0.7 min and alignment time window of 20 min. Maximum peptide mass was 5000 Da. No isobaric masses were enabled, as quantification was done using the intensity of the phosphopeptides in the MS scan.

4.3.6.3 Processing of MaxQuant data

MaxQuant outputs were further processed using phosphoprocessR version 0.99.8 (available as R package on github here: https://github.com/awaardenberg/phosphoProcessR), in R version 3.5.1 (Gentleman *et al.*, 2004), which implements methods previously described (Waardenberg, 2017; Engholm-Keller *et al.*, 2019), with the following differences. Phosphopeptides were remapped to the same fasta file used for MaxQuant quantification (see above) and centered peptide sequences with a window of +/- 7AA around each phosphorylated site annotated. Phosphopeptides were retained if a site localization score ≥0.75 (class I) for at least one site within a phosphopeptide for one experiment (where an experiment was an intensity reading from a TMT label), was observed. For multi-phosphorylated peptides, all additional sites belonging to the peptide with a class I

site must have had a score greater than 0.5. Where multiple measurements were obtained for the same phosphopeptide, the median log2 transformed intensity of all measurements was used. Measurements that mapped to more than one unique protein identifier were assigned a unique multi-mapped identifier. For SRPK2 phosphoproteome data, only complete data (no missing values for any replicates) was used (without imputation), followed by quantile normalization (Dudoit *et al.*, 2002) and surrogate variable analysis (Leek and Storey, 2007), with a prior model describing 3 groups – SRPK2, shSRPK2 and control. Principle component analysis and hierarchical clustering was used for guiding the impact of correction. For differential phosphorylation analysis (DPA) of SRPK2 data, we fit a generalized linear model with Bayes shrinkage as implemented in limma version 3.36.5 (Ritchie *et al.*, 2015) (https://bioconductor.org/packages/release/bioc/html/limma.html) and compare shSRPK2 vs. Ctrl and SRPK2 vs. Ctrl together (total complete data) and individually (as independent datasets). Where analyzed independently, normalization and surrogate variable analysis were applied to only the conditions compared. All p-values reported for SRPK2/shSRPK2 vs the control were first calculated as a moderated t-test and then corrected for multi-hypothesis testing using the Benjamini and Hochberg (FDR) method (Benjamini and Hochberg, 1995).

For classification of RIM1 in vitro phosphorylation sites, MaxQuant data were remapped using phosphoprocessR without imputation or surrogate variable analysis and converted to a boolean, present or absent call, based on detection in RIM1 or control replicates. A one-tailed fishers exact test (Fisher, 1934) was used to test for increased detection relative to control, specifically for RIM1 sites (the protein pulled down).

4.3.6.4 SRPK2 motif

SRPK2 motifs were generated from annotated and in vitro data for RIMS1. Motif position weight matrices were built from inputting sequencing into the viewPWM function of KinSwingR. Previously published SRPK2 targets were used to generate a SRPK2 motif (Table 9.1, Daub *et al.*, 2002; Jang *et al.*, 2008; Hong *et al.*, 2012; Duarte *et al.*, 2013; Mosca *et al.*, 2017). For in vitro data, all RIMS1 sites with an FDR < 0.2 were retained for building a SRPK2 motif, utilizing the buildPWM function

in KinSwingR, with either “S” or “S/T” centered phosphorylation site peptides. The information content at each position (described as bits) of each PWM, was modeled as per equation 1 and visualized as a Shannon Entropy model (Schneider and Stephens, 1990), where bits of each position, $bits_p$, are described as the difference between the maximum information content, where n = 20 (number of amino acids) and uncertainty at each position, p, for amino acid, a.

$$bits_p = log_2\,(n) - (\sum_{a=a}^{t} f(a,\,p) log_2 f(a,p)) \qquad \text{(Eq. 1)}$$

Groups of amino acids are colored according to the shapely scheme, where each AA has a unique color and polar/non-polar AAs are brighter/dull.

4.3.7 Immunoblotting

Proteins were analyzed using SDS-PAGE. Therefore, the appropriate resolving gel for the protein of interest (6-15%) and a 5% stacking gel were used. Denatured proteins were separated and blotted on a PVDF or nitrocellulose membrane overnight at 45-65 mA at 4°C. The membrane was blocked with 5% milk in PBS with 0.1% Tween-20 (PBST) for 1 h except for the analysis of biotinylated proteins. Here, a different blocking solution consisting of 2.5% bovine serum albumin (BSA, Roth), 0.4% Triton X-100 in PBS was used. Primary antibodies were diluted as indicated in Table 4.7 in 1% milk in PBST and incubated for 2 h at RT. Subsequently, membranes were washed three times for 10 min to remove unbound antibodies. Secondary antibodies (Table 4.8) were diluted 1:20,000 in 1% milk in PBST and incubated for 1 h at RT. Streptavidin antibodies were diluted in blocking solution (2.5% BSA, 0.4% Triton X-100) for 1 h at RT. The membranes were imaged using a Odyssey CLx (LiCOR). Visualization and quantification of the membrane were performed by means of ImageStudio Lite Software (LiCOR). The following antibodies were used for immunoblotting (Table 4.7 and 4.8):

Protein	Species	Dilution	Company
SRPK2	Mouse	1:500	Santa Cruz (sc-136078)
RIM1	Rabbit	1:1,000	Synaptic System (143 023)
Synaptophysin	Rabbit	1:1,000	Abcam (ab52636)
RIM-BP2	Rabbit	1:1,000	Synaptic System (316 103)
ELKS1/2	Rabbit	1:1,000	Synaptic System (140 003)
Synapsin1/2	Mouse	1:1,000	Synaptic System (106 011)
β-actin	Mouse	1:10,000	Abcam (ab6276)
Liprin-α3	Rabbit	1:1,000	Self-made (Zürner et al., 2011)
Munc13-1	Mouse	1:500	Synaptic System (126 111)
Munc13-1	Rabbit	1:500	Synaptic System (126 002)
Rab3	Mouse	1:1,000	Synaptic System (107 011)

Table 4.7: Primary antibodies for immunoblotting

Name	Host	Dilution	Company
α-mouse, IRDye 680	Goat	1:20,000	LI-COR Biosciences (926-68070)
α-rabbit, IRDye 800	Goat	1:20,000	LI-COR Biosciences (926-32211)

Table 4.8: Secondary antibodies for immunoblotting

4.4 Histological and immunochemical methods

4.4.1 Immunocytochemical staining (ICC)

Cortical or hippocampal neurons were fixed at DIV14-16 with 4% PFA for 15 min at RT. Neurons were washed three times with PBS and incubated for 10 min with 0.3% Triton X-100 in PBS at RT to permeabilize the cells. Afterwards, blocking buffer (10% normal goat serum (NGS), 1% BSA, 0.1% Triton X-100 in PBS) was applied to block unspecific binding. Primary antibodies were diluted in blocking buffer and incubated overnight at 4°C (Table 4.9). Three washing steps with PBS removed the primary antibody. Secondary antibodies were incubated for 3 h at RT (Table 4.10). After the

incubation, neurons were washed three times and either mounted with of Mowiol 4-88 or used for STORM imaging. The following primary antibodies were used:

Protein	Dilution	Company
SRPK2	1:100	Santa Cruz (sc-136078)
RIM1	1:1000	Synaptic System (143 003)
Bassoon	1:5000	EnzoLifeScience (ADI-VAM-PS003)
RIM-BP2	1:500	Synaptic System (316 103)
ELKS1/2	1:1000	Synaptic System (140 003)
Synapsin1/2	1:3000	Synaptic System (106 004)
PSD-95	1:200	Neuromab (75-028)
Homer1	1:1000	Synaptic System (160 004)

Table 4.9: Primary antibodies for ICC stainings

Name	Dilution	Company
goat α-rabbit CF568	1:200	Sigma-Aldrich (SAB4600085)
goat α-mouse CF568	1:200	Sigma-Aldrich (SAB4600082)
goat α-mouse Alexa Fluor® 647	1:200	Life Technologies (A-21236)
goat α-guinea pig Alexa Fluor® 647	1:200	Life Technologies (A-21450)
goat α-rabbit pig Alexa Fluor® 647	1:200	Life Technologies (A-21244)
goat α-guinea pig Alexa Fluor® 488	1:200	Life Technologies (A-11073)
donkey α-guinea pig Cy3	1:400	Jackson ImmunoResearch (706-165-148)

Table 4.10: Secondary antibodies for ICC stainings

4.4.2 Immunohistochemistry (IHC) staining of slices

EtiCre:BioID, ProxCre:BioID and wild-type mice perfused with 4% PFA. Brains were dissected and incubated overnight in 4% PFA at 4°C. Brains were sliced in 50 µm coronal or sagittal sections and post fixed in 4% PFA overnight at 4°C. Slices were

washed 3 times with PBS and stored at 4°C. The staining procedure with primary and secondary antibodies was performed as mentioned above (4.4.1). Slices were mounted using Mowiol 4-88.

4.4.3 Confocal imaging and quantification of synaptic protein intensities

Hippocampal neurons were stained with synapsin to define synapses and co-stained with various AZ proteins. AZ proteins were labeled with Alexa-568 fluorophore and red fluorescent beads (InSpeck™Red beads 0.1%, ThermoFisher) were co-embedded. Images were acquired using a laser-scanning Nikon A1/Ti confocal microscope with a Plan APO IR 60x WI objective (numerical aperture (NA) 1.27) and the Nikon NIS-Elements 4.0 acquisition software. The analysis was performed in ImageJ (Schindelin *et al.*, 2012). Synapses were defined using 20% of the maximum intensity of the synapsin staining as the lower threshold. The synapsin staining was segmented and the synapse area was set to 0.06 μm^2 - 0.85 μm^2. The maximum intensity of the fluorescent beads was used to normalize the fluorescence intensity of AZ proteins. For each biological replicate, three technical replicates were imaged and averaged.

4.4.4 Direct stochastic optical reconstruction microscopy (dSTORM)

dSTORM imaging was performed on a Leica SR GSD 3D microscope (Leica Microsystems) with a 160x immersion oil objective (NA 1.47). The setup was equipped with 405- (30mW), 488- (300mW), 532- (500mW) and 642-nm (500mW) lasers. Excitation light was reflected to the sample via a quad band emission filter. The dSTORM video sequence was imaged with a sCMOS camera (pco.edge4.2, PCO). The microscope contained a suppressed motion (SuMo) stage to minimize stage drift.

Mouse primary neurons were fixed and stained as described in 4.4.1. Labeled neurons were incubated in GLOXY STORM imaging buffer (50 mM β-Mercaptoethylamine hydrochloride (MEA), 10% (v/v) of a 250 g/l solution of glucose, 0.5 mg/ml glucose oxidase, 40 mg/ml catalase in PBS, pH 7.6), (Nahidiazar *et al.*, 2016)) on depression slides and sealed with Twinsil silicone glue (Picodent). Overview images were acquired in the laser widefield mode using 10% laser power for 488- and 532 nm laser and 5% laser power for the 642 nm laser using 500 ms

exposure time each. For RIM1 acquisitions with the 642 nm laser, 50% laser power for 20 s was used for pumping the fluorescent molecules into the dark state. For acquisition, 150,000 frames at 500 Hz were acquired using 30% laser power. SRPK2 was also imaged with the 642 nm laser. For pumping, 50% laser power was used for 10 s. The image was acquired using 30% laser power for 200,000 frames at 500 Hz. Homer1 was imaged with the 488 nm laser. Here, 70% laser power was used for pumping for 20 s. For acquisition, 30% laser power was used and 40,000 frames at 100 Hz. The stochastically occurring blink events were detected in the Leica image acquisition software (LAS AF Version 1.9.0). The detection thresholds were chosen such that unspecific blink events were discarded and that detected events represented specific events that were used for the dSTORM image reconstruction. The detection thresholds were 8 photons/pixel for RIM1 and SRPK2 and 20 photons/pixel for Homer1. The detected blink events were fitted with a Gaussian fit. Repeatedly occurring blink events within a maximum xy distance of 70 nm with a maximum appearance of 10 frames were merged to one event. The event coordinates were used to generate a 2D density histogram with a pixel size of 20 nm.

4.4.5 dSTORM cluster analysis

The density histograms generated by the Leica image acquisition software were imported to ImageJ. The 2D density histogram was segmented according to grayscale pixel values with a lower threshold of 20 for RIM1 to define clustered RIM1 molecules. Additionally, only cluster larger than 800 nm^2 were included in the analysis. Smaller RIM1 molecules represent non-clustered RIM1 molecules.

Synapsin laser-widefield images were used to define synaptic areas. As described in 4.4.3, synapses were defined using 20% of the maximum grayscale intensity as a lower threshold. The generated synaptic areas were superimposed on the 2D density histogram. Synaptic clusters had to be completely in the synapsin-defined synaptic area, while extrasynaptic clusters had to be completely outside the synaptic area. Clusters that were partially overlapping with synapsin and therefore could not be identified as synaptic or extrasynaptic with certainty were excluded from the cluster analysis. The measured grey values of the 2D density histogram represent the number of molecule localizations. The number of localizations per cluster was measured for synaptic and extrasynaptic clusters as well as the cluster area, cluster

density and the overall number of clusters. The number of non-clustered RIM1 molecules was measured for the whole axon. Therefore, the GFP widefield image was segmented to define the axon. All RIM1 localizations were measured within the axon and local background measurements were used to subtract the background. The clustered RIM1 localizations were subtracted from all RIM1 localizations to calculate the non-clustered molecules.

To identify synaptic SRPK2 clusters, the density histograms of SRPK2 and Homer1 generated by the Leica Software were loaded in ImageJ and grey scale threshold of 10 for SRPK2 and 20 for Homer1 was used to distinguish clustered from non-clustered molecules. The nearest Homer1 cluster of each SRPK2 cluster was measured using the line tool in ImageJ. We defined SRPK2 clusters as presynaptic if they were within a 200 nm distance to a Homer1 cluster. SRPK2 clusters were defined as postsynaptic if they overlapped with at least 50% with a Homer1 cluster.

4.5 *In vivo* injections: P0-P3 animal injection

Newborn mice received a drop of Novalgin into their mouth 30 min prior to injection. Pups were placed into a glove to prevent direct contact to ice and then incubated for 50 sec on ice. When they stopped moving, they were injected with 1 µl rAAV1/2-GFP in the hippocampus in each hemisphere with maximum speed. The mice were warmed up on the 37 °C heat plate and put back into the cage to their mother.

4.6 Fluorescent activated synaptosome sorting (FASS)

For the FASS sorting a FACS Aria cell sorter III with a 70 µm nozzle was used and the sample was shaking at 300 rpm. For the Forward Scatter (FSC) a neutral density filter of 1.0 was used. Only the 488 laser was turned on. The Area Scaling was set to 1.18 and window extension to 0.0. The FSC Area Scaling was set to 0.96 and the sort precision was 0-16-0. The following optical parameters were used (Table 4.11):

Channel	Filter and gain
FSC	ND1.0, 340V
SSC	488 / 10 nm, 365 V
FITC (mVENUS)	530/30 nm, 700 V
PerCP (FM4-64)	695/40nm, 695 V

Table 4.11: Optical parameters for FASS

The threshold for the PerCP channel was set to 1000.

The noise baseline of the system was checked by loading PBS supplemented with 1.5 µg/ml FM4-64 and a flow rate of 3. The detected events should be less than 200 events/min. In case of higher noise detection, ultra pure water was run for 10 min at maximal flow rate before running again PBS with FM4-64 at flow rate of 3.
The auto fluorescence of synaptosomes was detected using WT (non-fluorescent) synaptosomes. Synaptosomes were diluted in PBS with proteinase inhibitor (Protease Inhibitor Cocktail Set III, EDTA-free, Millipore, 1:1000). To detect the synaptosomes, 1.5 µg/ml FM4-64 to label membranes was added and synaptosomes were run through the system with a flow rate of 3. The events should be less than 20,000 events/min. The gate P1 (Figure 4.1.A) was set that 80% of the events were included in the gate. P1 represents the non-aggregated synaptosomes and is further divided into gate P2 and P3 (Figure 4.1.B). P2 includes the auto fluorescent population, while P3 is set above P2 as close as possible but without including any of the events of the WT population (Figure 4.1.B). The events forming a diagonal with increased FSC and SSC are aggregated synaptosomes, which will be detected in P5 (Figure 4.1.A).

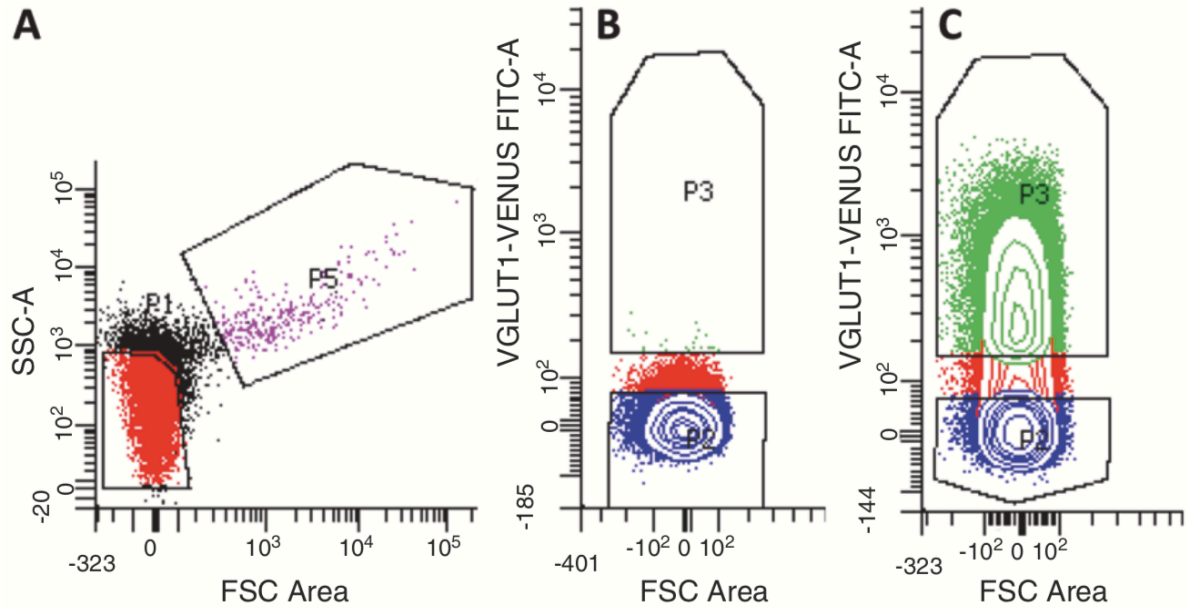

Figure 4.1: Analysis of VGLUT1^{venus} synaptosomes.

(A) All events are detected by FM4-64. P1 gate includes single particles and should consists of approximately 80% of the whole population. P5 includes aggregates, which form a diagonal. P1 population is further divided into P2 and P3. **(B)** P2 represents the non-fluorescent synaptosomes, while P3 is empty for WT synaptosomes. **(C)** Non-fluorescent of VGLUT^{venus} synaptosomes are detected in P2, while Venus-fluorescent synaptosomes are found in P3 (Luquet *et al.*, 2017).

The fluorescent synaptosomes are also supplemented with FM4-64 and then sorted at a flow rate of 3. For the fluorescent sample, a population is detected in P3 (Figure 4.1.C). The sample was run through the sorter for 1 min before the actual sort would start. Synaptosomes were collected in a 15 ml falcon.

After the falcon was filled up, a quality control was performed. Therefore, 500 µl of the sorted sample was transferred in to a new FACS tube and FM4-64 was added. The sample was run through the system for 1 min at a flow rate of 11, then 1 min at a flow rate of 3 before it was recorded for 1 min.

4.7 *In vivo* biotin application

Different biotin applications were performed to test for the highest biotinylation efficiency. Two different mouse lines were used. Et-iCre:BioID mice express the biotin ligase BirA in the CA3 pyramidal cells and their Schaffer Collateral synapses. Prox1Cre:BioID mice express BirA of the granule cells in the hippocampus and the

mossy fiber synapses. Subcutaneous injections were performed for seven consecutive days. Biotin was dissolved in a 25% PEG-400 solution and 24 mg biotin/kg was injected subcutaneously. For application in drinking water, 0.22 mg/ml Biotin was dissolved in autoclaved water and given for 7 days. Biotin food contained 800 mg/kg Biotin (ssniff) and was given for 14 consecutive days before animals were sacrificed. Animals were perfused for immunohistochemical stainings or hippocampi were used to prepare synaptosomes or samples for mass spectrometry.

To perform microdissection, brains were sliced in 300 µm thick slices and the respective area was microdissected and immediately transferred into an eppendorf tube on dry ice.

5. Results

5.1 Characterization of SRPK2 and its role in synaptic plasticity

5.1.1 Identification of SRPK2 as a synaptic protein

5.1.1.1 Expression of SRPK2 increases during synaptogenesis

The *Drosophila melanogaster* homolog of SRPK2, SRPK79D has been shown to regulate active zone assembly and to colocalize with Bruchpilot (Johnson *et al.,* 2009; Nieratschker *et al.*, 2009; Driller *et al.*, 2019). SRPK2 has been demonstrated to be present in synapses and colocalize with the presynaptic marker bassoon and the postsynaptic marker PSD-95 (data not shown, PhD thesis Ana-Maria Oprişoreanu, 2014). Here, we focused on SRPK's function in the presynapse because neuronal activity has been shown to change in particular the phosphorylation status of presynaptic active zone members (Engholm-Keller *et al.*, 2019). To analyze the expression profile of SRPK2 during brain development, we looked at different time points starting at postnatal day 0 (P0) until P30. Therefore, mice at the indicated time points were sacrificed and total brain homogenates were prepared to evaluate the protein levels of SRPK2 and several presynaptic proteins. SRPK2 levels increase during synaptogenesis and peak at P5-P15 as other synaptic proteins like RIM1 and ELKS1/2 (Figure 5.1).

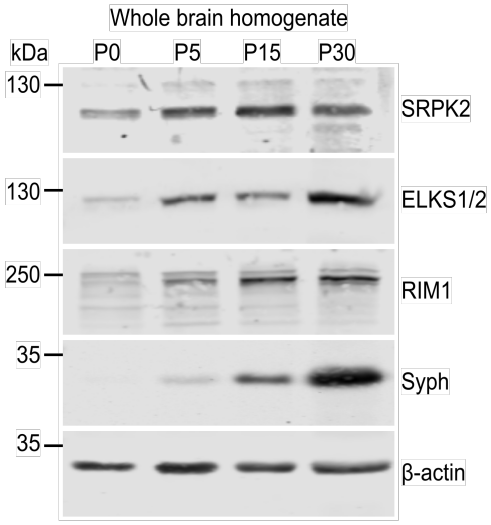

Figure 5.1: Developmental time course of SRPK2 expression.
Mice were sacrificed at postnatal days 0 (P0) to P30 and whole brain homogenates were prepared. Expression levels of synaptic proteins were analyzed using immunoblots. Syph = synaptophysin. N = 3.

5.1.1.2 SRPK2 is tightly integrated in the synaptic membrane fraction

Next, we wanted to investigate the localization of SRPK2 using subcellular fractionation of mouse brain tissue (Figure 5.2). Consecutive homogenization steps of the whole brain homogenate (WB) resulted in crude synaptosomes (P2). The synaptosomes were further treated with the detergent Triton X-100 to separate proteins that are tightly integrated in the synaptic membrane fraction like the CAZ proteins RIM1 and ELKS1/2, which are found in fraction P4, from TX-100 soluble proteins like Liprin-α3. SRPK2 demonstrated the highest abundance in the TX-100 resistant fraction P4 indicating that SRPK2 is an intrinsic protein of the synaptic membrane.

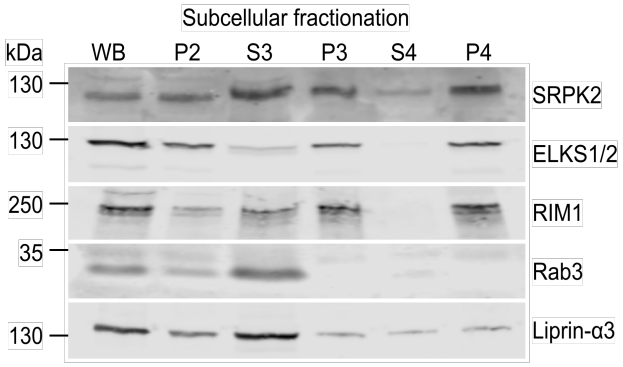

Figure 5.2: SRPK2 is enriched in the TX-100 resistant synaptic membrane fraction. Subcellular fractionation of mice brain homogenates was performed to analyze the association of SRPK2 with the pre- or postsynaptic cytomatrix. WB = Whole brain homogenate, P2 = crude synaptosomes, S3 = Cytosolic synaptic fraction, P3 = Synaptic plasma membrane, S4 = TX-100 soluble fraction, P4 = TX-100 resistant synaptic membrane fraction. N = 3.

5.1.1.3 Modulation of SRPK2 protein level at the synapse using viral vectors

To study the role of SRPK2 on presynaptic active zone structure, we used viral vectors for an shRNA mediated knock-down (KD) and overexpression (OE) of SRPK2 in primary neurons. Therefore, cortical neurons were transduced with purified recombinant adeno-associated virus (rAAV) coding for shSRPK2-GFP, SRPK2-GFP or only GFP as a control. At *day in vitro* (DIV) 14-16, neurons were lysed and protein levels were analyzed using immunoblots (Figure 5.3.A). Overexpression of SRPK2 resulted in a significant increase of SRPK2 protein levels around 5-fold (4.8 ± 0.93 normalized to control). Interestingly, not only SRPK2-GFP was increased but also endogenous SRPK2 levels were elevated. Knock-down of SRPK2 successfully reduced the protein level by 84% (0.16 ± 0.016 normalized to control).

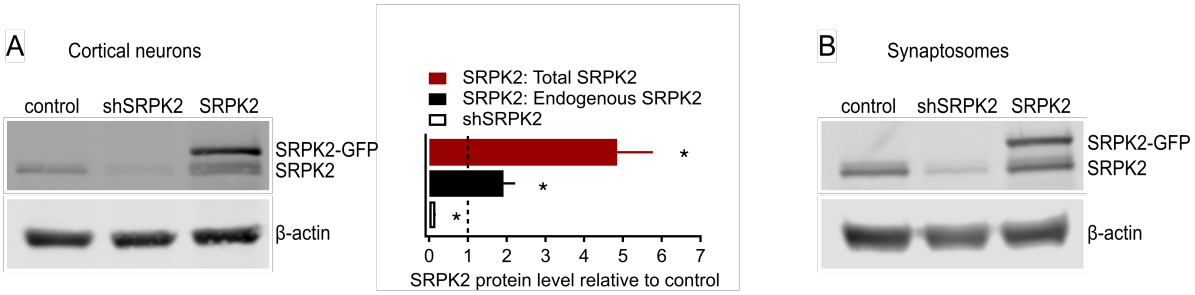

Figure 5.3: Modulation of SRPK2 expression in primary neurons.
(A) Cortical neurons were transduced with U6-GFP, shSRPK2-GFP or SRPK2-GFP rAAVs and lysed at DIV14. SRPK2 overexpression resulted in significantly increased and knock-down of SRPK2 in reduced SRPK2 protein levels. All data are shown as mean ± SEM. N = 5. *p < 0.05, One-Way ANOVA, Holm-Sidak correction for multiple comparisons. **(B)** Synaptosomes were prepared to analyze SRPK2 changes at the synapse after transduction. N = 2.

To analyze the change of protein levels at the synapse, synaptosomes from cortical neurons were prepared. Immunoblotting revealed that SRPK2 protein levels were modulated at the synapse (Figure 5.3.B). In conclusion, this demonstrates that the viral vectors can be used in neuronal cultures to modulate SRPK2 expression and study its role in AZ organization and synaptic plasticity.

5.1.2 The SRPK2 phosphoproteome

5.1.2.1 Identification of the SRPK2 phosphoproteome using mass spectrometry

So far, only specific targets of SRPK2 were studied such as tau (Hong *et al.*, 2012), a delta-secretase (AEP) involved in the cleavage of APP and tau (Wang *et al.*, 2017) or different viral proteins (Daub *et al.*, 2002; Duarte *et al.*, 2013). However, no general screen for SRPK2 targets in neurons has been conducted until now. Thus, we overexpressed or knocked-down SRPK2 in primary cortical neurons, lysed them at DIV14-16 and identified the SRPK2 phosphoproteome by mass spectrometry (Figure 5.4.A, MS work performed by the group of Mark Graham, Sydney, Australia).

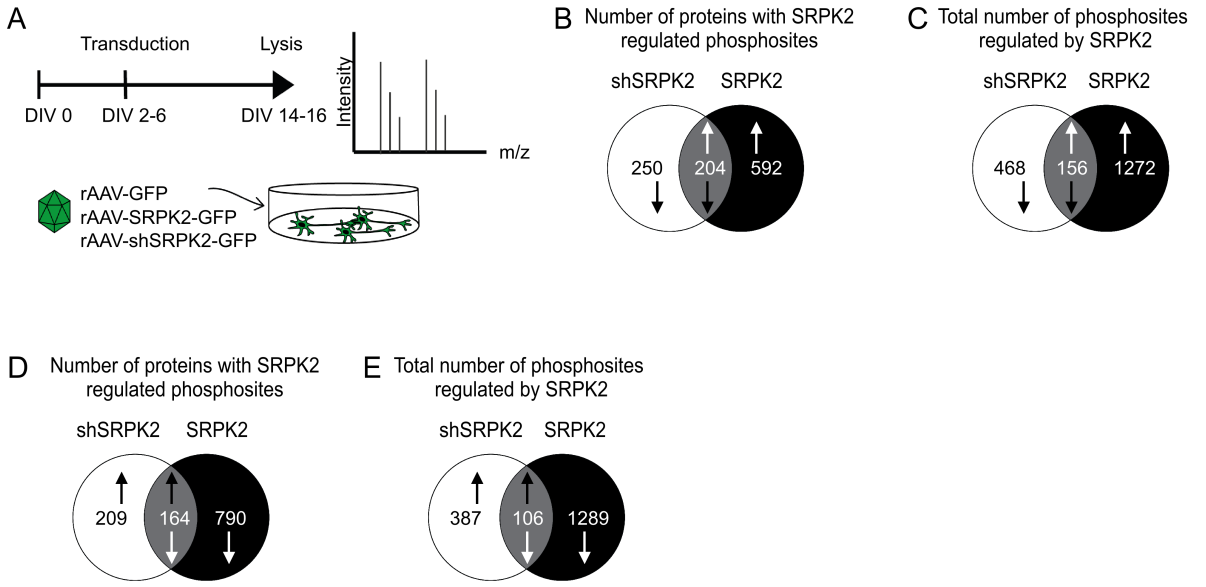

Figure 5.4: Identification of neuronal SRPK2 targets using mass spectrometry.
(A) Workflow for mass spectrometry: Primary cortical neurons were transduced with U6-GFP control, shSRPK2-GFP or SRPK2-GFP rAAVs and lysed at DIV14-16. Phosphorylation sites were detected using mass spectrometry. **(B)** Number of proteins with SRPK2 regulated phosphorylation sites that were significantly upregulated for SRPK2 overexpression or downregulated by shSRPK2. **(C)** Number of phosphorylation sites that were significantly upregulated for SRPK2 overexpression or downregulated by shSRPK2. **(D)** Number of proteins with phosphorylation sites that were significantly downregulated by SRPK2 overexpression or upregulated by shSRPK2. **(E)** Number of phosphorylation sites in proteins that were significantly downregulated by SRPK2 overexpression or upregulated by shSRPK2. Moderated t-test for B-E.

We detected 592 proteins that revealed upregulated phosphorylation sites for SRPK2 OE compared to control, while 204 proteins showed downregulated phosphorylation sites in the knock-down (Figure 5.4.B). On top, 204 proteins displayed upregulated phosphorylation sites for SRPK2 OE and simultaneously downregulated phosphorylation sites for knock-down of SRPK2. Multiple proteins exhibited several regulated phosphorylation sites (Figure 5.4.C). In total, 1272 phosphorylation sites were exclusively upregulated by SRPK2 OE and 468 phosphorylation sites downregulated in the SRPK2 knock-down. However, 156 phosphorylation sites were upregulated when SRPK2 was overexpressed and simultaneously downregulated in the SRPK2 knock-down. A similar number of proteins and phosphorylation sites were regulated in the opposing direction in both conditions meaning upregulated for the

SRPK2 knock-down and downregulated when SRPK2 was overexpressed (Figure 5.4.D and 5.4.E). This data indicates that SRPK2 controls the phosphorylation status of a large number of neuronal proteins either by direct phosphorylation or indirectly via other kinases and phosphatases.

5.1.2.2 Synaptic proteins are phosphorylated by SRPK2

The SRPK family has been so far primarily investigated with regard to the phosphorylation of components of the spliceosome. To characterize the targets of SRPK2, we performed a gene ontology enrichment analysis (Figure 5.5). Three different analyses were performed to acquire an overview of proteins whose phosphorylation status was regulated by SRPK2. The categorization by biological process highlighted that proteins involved in mRNA splicing are phosphorylated by SRPK2, which was expected from literature of non-neuronal cells, but also many proteins involved in synaptic processes such as synaptic vesicle priming or regulation of synaptic plasticity were detected (Figure 5.5.A). The regulated proteins were widely distributed regarding their molecular function (Figure 5.5.B). Interestingly, many SRPK2 targets are localized at synaptic compartments like the presynaptic AZ or postsynaptic density (PSD) (Figure 5.5.C).

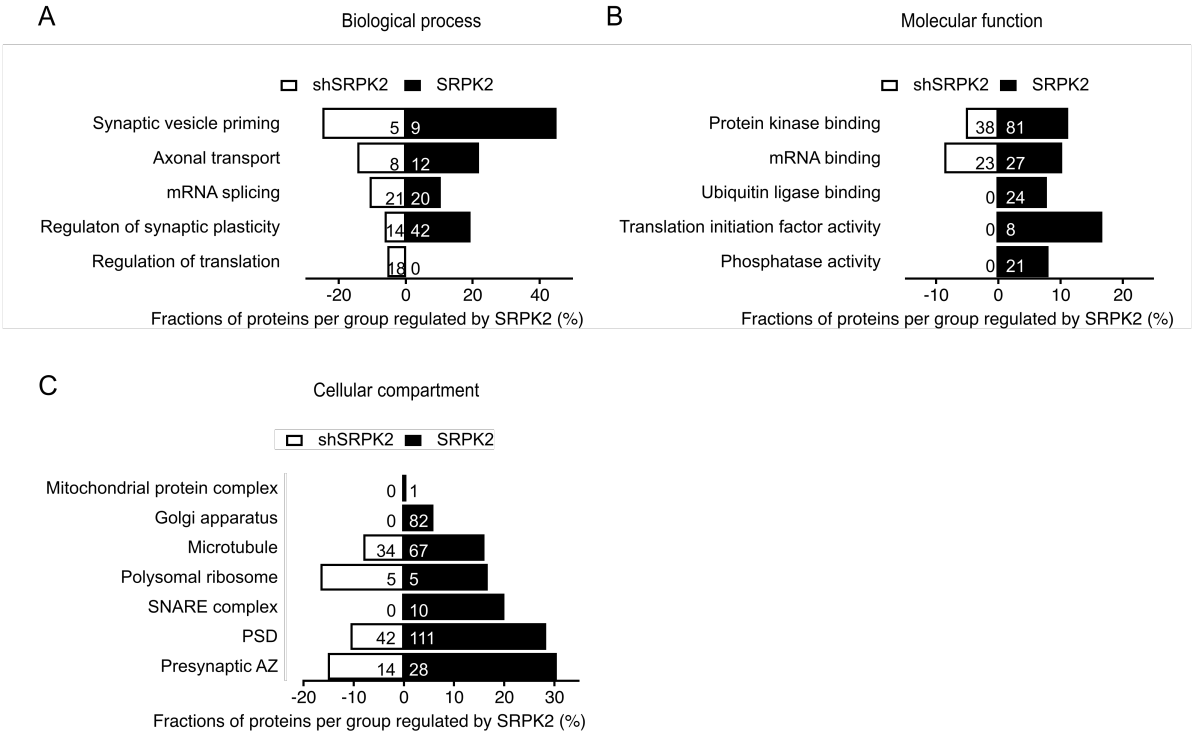

Figure 5.5: Characterization of SRPK2 targets.
(A-C) Gene ontology enrichment analysis of SRPK2 targets that were upregulated by SRPK2 overexpression and downregulated when SRPK2 was knocked-down. Proteins were categorized with respect to their biological process (A), molecular function (B) and cellular compartment (C). Numbers indicate the total number of proteins that were regulated per group.

Our gene ontology enrichment analysis of the molecular function revealed that several SRPK2 targets are involved in protein kinase binding or phosphatase activity. To analyze if SRPK2 regulates other kinases or phosphatases, which potentially regulate different de- and phosphorylation signaling cascades, the kinases and phosphatases with the most regulated phosphorylation sites were identified by Ash Waardenberg (Figure 5.6). Many kinases and phosphatase that exhibited the highest regulation in their phosphorylation status have already been linked to presynaptic function like Calcium/Calmodulin Dependent Serine Protein Kinase (CASK), cyclin-dependent kinase-like 5 (CDKL5), BR Serine/Threonine Kinase 1 (Brsk1) and WNK Lysine Deficient Protein Kinase 1 (Wnk1), which exhibited the highest upregulated phosphorylation sites after SRPK2 overexpression. Similarly, the top downregulated kinases in the SRPK2 knock-down revealed kinases with presynaptic function: Microtubule Associated Serine/Threonine Kinase 1-4 (Mast1-4), Bcr (SAD) kinase, Tau-tubulin kinase 2 (Ttbk2) and Calcium/Calmodulin Dependent Protein Kinase II beta (CamKIIb). The kinases with the most regulated phosphorylation site for both SRPK2 overexpression and knock-down was CASK (Figure 5.6.A). The counterpart for the phosphatases was the Protein phosphatase 6 Regulatory Subunit 3 (PPP6r3) (Figure 5.6.B). This data highlights the potential regulatory role of SRPK2 for kinases and phosphatases. Therefore, some regulations in the phosphorylation status of proteins that we detected in our phosphoproteomic experiment might be caused indirectly by other kinases or phosphatases that are activated or deactivated by SRPK2.

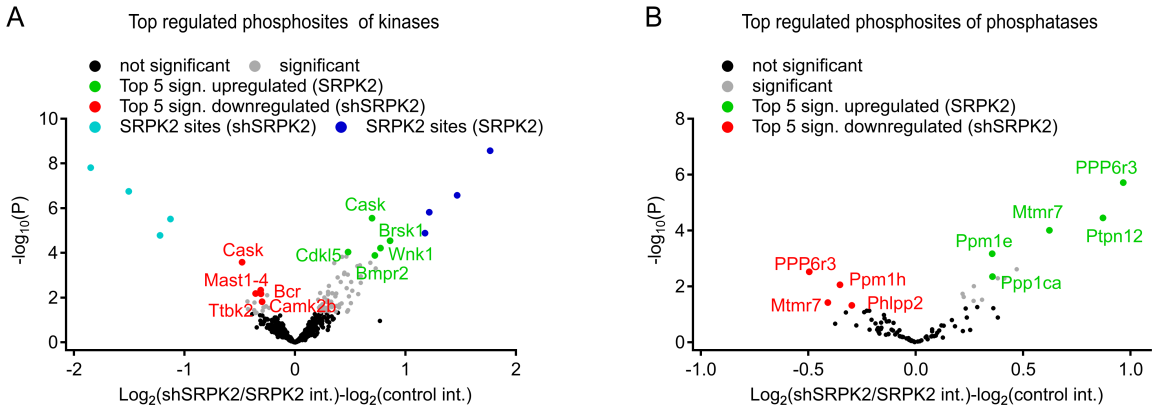

Figure 5.6: SRPK2 regulates phosphorylation network.

(A and B) Volcano plots of all significantly upregulated proteins when SRPK2 was overexpressed and downregulated proteins for SRPK2 knock-down. Top 5 regulated kinases (A) and phosphatases (B) are indicated for SRPK2 overexpression (green) and SRPK2 knock-down (red).

To analyze the enrichment of synaptic targets of SRPK2, we used the SynGO classification (Koopmans *et al.*, 2019) (Figure 5.7). In total, the phosphorylation status of 19.65% of synaptic proteins was regulated by SRPK2 overexpression and 6.33% in the SRPK2 knock-down. In the presynapse 94 out of 482 proteins exhibited a change in their phosphorylation status in the SRPK2 overexpression compared to 34 proteins in the knock-down of SRPK2. A similar amount of postsynaptic proteins was regulated by SRPK2 (117 for SRPK2 overexpression and 34 for SRPK2 knock-down out of 592). Predominantly the phosphorylation status of proteins of the presynaptic AZ (AZ) was regulated (25/89 for SRPK2 OE, 10/89 for SRPK2 KD). Two other categories with multiple regulated proteins were synaptic vesicles associated proteins (SV, 17/110 for SRPK2 OE, 7/110 for SRPK2 KD) and proteins located at the presynaptic membrane (PrSM, 23/128 for SRPK2 OE, 3/128 for SRPK2 KD). In the postsynapse, mainly proteins of the postsynaptic specialization (PSS, 66/300 for SRPK2 OE, 20/300 for SRPK2 KD) displayed a regulation in their phosphorylation status. Proteins located at the synaptic cleft or categorized as organelles like endoplasmic reticulum (ER) were not detected.

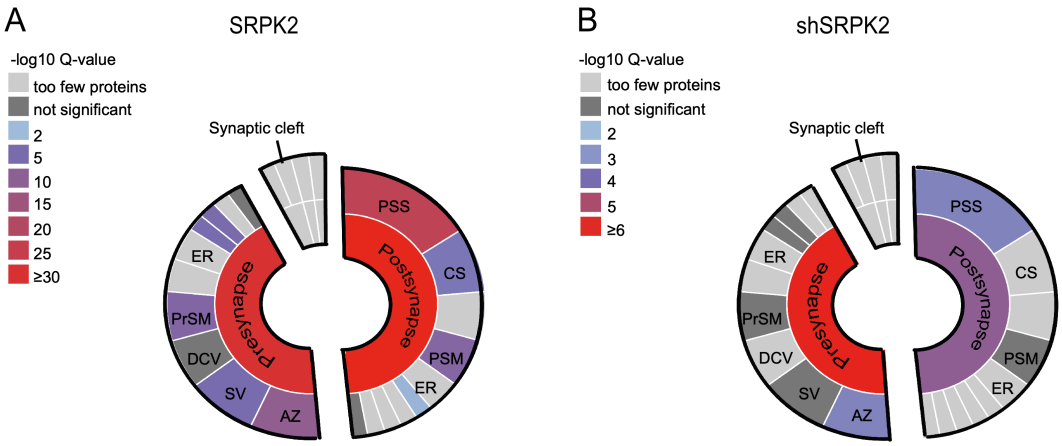

Figure 5.7: Synaptic proteins are phosphorylated by SRPK2.
Overview about significantly regulated proteins using the SynGO classification (Koopmans *et al.*, 2019). **(A)** Proteins with upregulated phosphorylation sites by SRPK2. **(B)** Proteins with downregulated phosphorylation sites in SRPK2 knock-down. AZ: Active zone, SV: Synaptic vesicle, DCV: Dense core vesicle, PrSM: Presynaptic membrane, ER: Endoplasmic reticulum, PSS: Postsynaptic specialization, CS: Cytoskeleton, PSM: Postsynaptic membrane.

As we had found that SRPK2 is an integral part of the synaptic membrane (Figure 5.2), we examined the regulation of the phosphorylation status of AZ proteins by SRPK2 (Figure 5.8.A and 5.8.B). Several AZ proteins exhibited phosphorylation sites that were regulated in neurons overexpressing SRPK2 and/or in the SRPK2 knock-down. Due to the different length of the proteins (for example: RIM1: 1463 amino acids (aa), ELKS1 (Erc1): 1120 aa, bassoon (BSN): 3938 aa, piccolo (Pclo) 5068 aa), we calculated the detected regulated phosphorylation sites as the percentage of the total phosphorylation sites (Figure 5.8.A) and per amino acids (Figure 5.8.B). RIM1 showed the highest percentage of regulated phosphorylation sites and therefore is a prime candidate for a SRPK2 target.

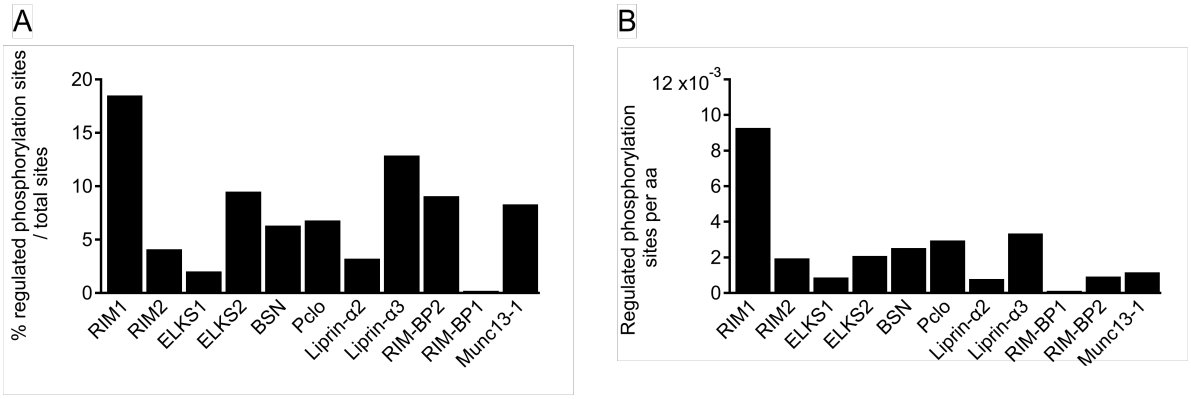

Figure 5.8: SRPK2 changes the phosphorylation status of several AZ proteins.
(A) Regulated phosphorylation sites of indicated presynaptic SRPK2 targets with respect to their total number of phosphorylation sites for SRPK2 overexpression and SRPK2 knock-down. **(B)** Regulated phosphorylation sites of indicated proteins with respect to their number of amino acids for SRPK2 overexpression and SRPK2 knock-down.

The analysis revealed several phosphorylation sites in RIM1 that were upregulated in the SRPK2 OE (Figure 5.9). Only at three sites (S287, S1023:1027, S1027) the phosphorylation status was significantly decreased for the knock-down but interestingly two sites (S287 and S1023, green) were also found to be upregulated in the SRPK2 OE condition, while S1027 was exclusively regulated in the knock-down of SRPK2 (blue). Surprisingly, none of the detected phosphorylation is located in a structured domain but all are found in the disordered and low complexity region of RIM1.

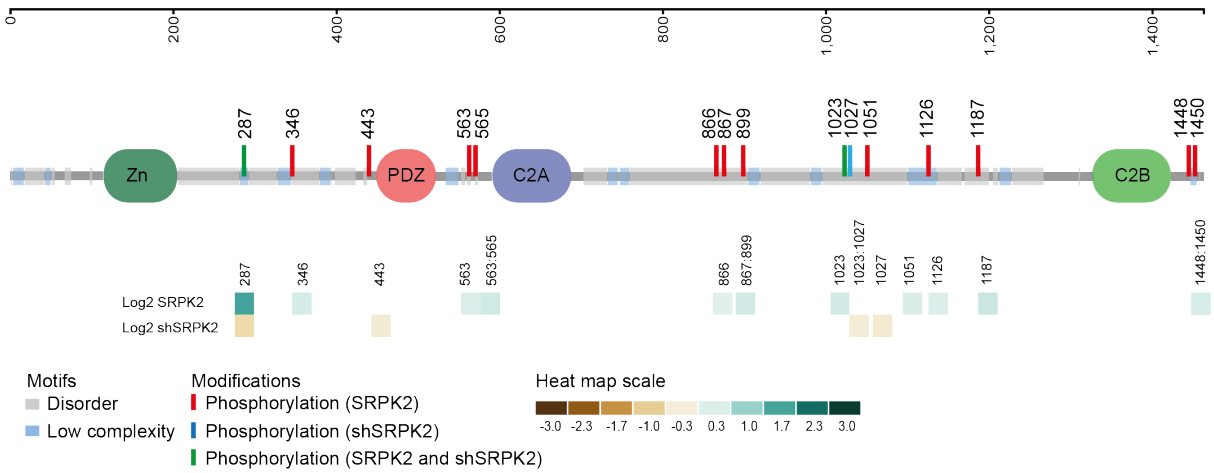

Figure 5.9: RIM1 phosphorylation sites were regulated by SRPK2.
Domain structure of RIM1 with regulated phosphorylation sites. Heat map indicates Log_2 values (SRPK2/control intensity or shSRPK2/control intensity). Residues are indicated using mouse nomenclature of RIM1.

As SRPK79D in *Drosophila melanogaster* phosphorylated Bruchpilot, we were wondering whether we also detect phosphorylation sites in ELKS1 or ELKS2 and if these are homologs to the ones found in Bruchpilot (Driller *et al.*, 2019). However, we detected only one upregulated phosphorylation site (S415) in ELKS1 in our experiments for SRPK2 overexpressing neurons (Figure 5.10.A). For ELKS2, we detected two upregulated phosphorylation sites (S33 and S946, Figure 5.10.B). While S33 showed an increase in phosphorylation for SRPK2 overexpression, the increased phosphorylation of S946 was detected in the SRPK2 knock-down. However, none of the regulated phosphorylation sites were the homologues sites that were found in *Drosophila melanogaster* (Driller *et al.*, 2019).

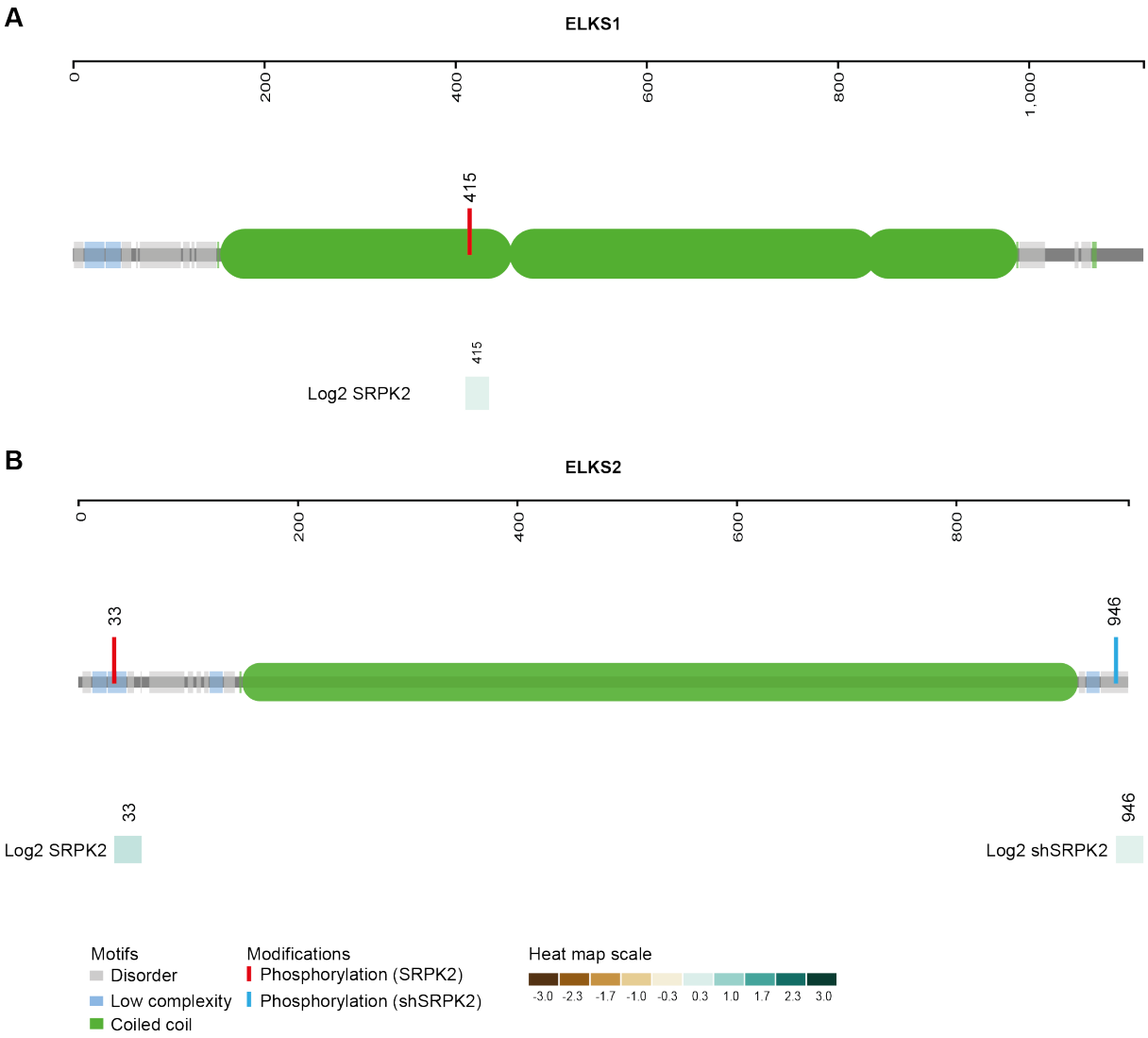

Figure 5.10: SRPK2 regulates ELKS1 and ELKS2 phosphorylation.

(A) Domain structure of ELKS1 with regulated phosphorylation site. Heat map indicates Log_2 values (SRPK2/control intensity). **(B)** Domain structure of ELKS2 with regulated phosphorylation site. Heat map indicates Log_2 values (SRPK2/control intensity for S33 and shSRPK2/control intensity for S946). Residues are indicated using mouse nomenclature of ELKS1/2.

5.1.2.3 RIM1 is a direct target of SRPK2

5.1.2.3.1 Generation of GST-fusion peptides and domains of RIM1

Our phosphoproteomic analysis revealed several phosphorylation sites in RIM1 that were regulated by SRPK2 pointing to RIM1 as a downstream effector. Due to the physiological conditions in the cultures, in which also other kinases were present,

secondary effects could not be excluded. Thus, it is possible that SRPK2 induced the phosphorylation of RIM1 by phosphorylating other kinases. To prove that RIM1 is a direct target of SRPK2, we performed radioactive *in vitro* phosphorylation. Short peptides fused to glutathione-S-transferase (GST) were cloned with the potentially phosphorylated residue in the middle of the peptide (P0 position) to identify specific phosphorylation sites in RIM1 (Figure 5.11.A and 5.11.B). In total, 12 GST-RIM1 peptides with a length of 13-15 amino acids were overexpressed in BL21 *Escherichia coli*. Additionally, a positive control consisting of only RS dipeptides (RSRS) and a negative control without any serine, threonine or tyrosine were cloned. Myelin-basic protein (MBP) was additionally used as a positive control since it is a known target of SRPK1 (Gui *et al.*, 1994) and its yeast homologue Dsk1 (Tang *et al.*, 1998). Surprisingly, none of the peptides were phosphorylated (Figure 5.11.C). One explanation could be that RIM1 is not phosphorylated by SRPK2 at these residues. However, the positive control (RSRS) was also not phosphorylated. Another possibility is that the C-terminus behind the tested serines at P0 position is not long enough for SRPK2 to bind the peptide because it consisted only of 6 amino acids. SRPK2 phosphorylates its targets from C-terminus to N-terminus (Ghosh and Adams, 2011) and the short peptide might hinder the binding and subsequent phosphorylation.

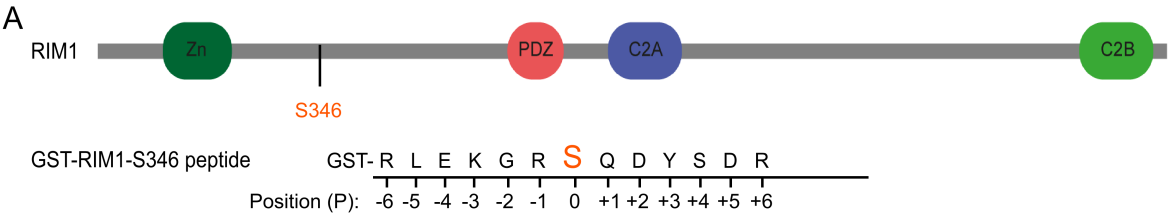
A
RIM1
Zn
PDZ
C2A
C2B
S346
GST-RIM1-S346 peptide
GST- R L E K G R S Q D Y S D R
Position (P): -6 -5 -4 -3 -2 -1 0 +1 +2 +3 +4 +5 +6

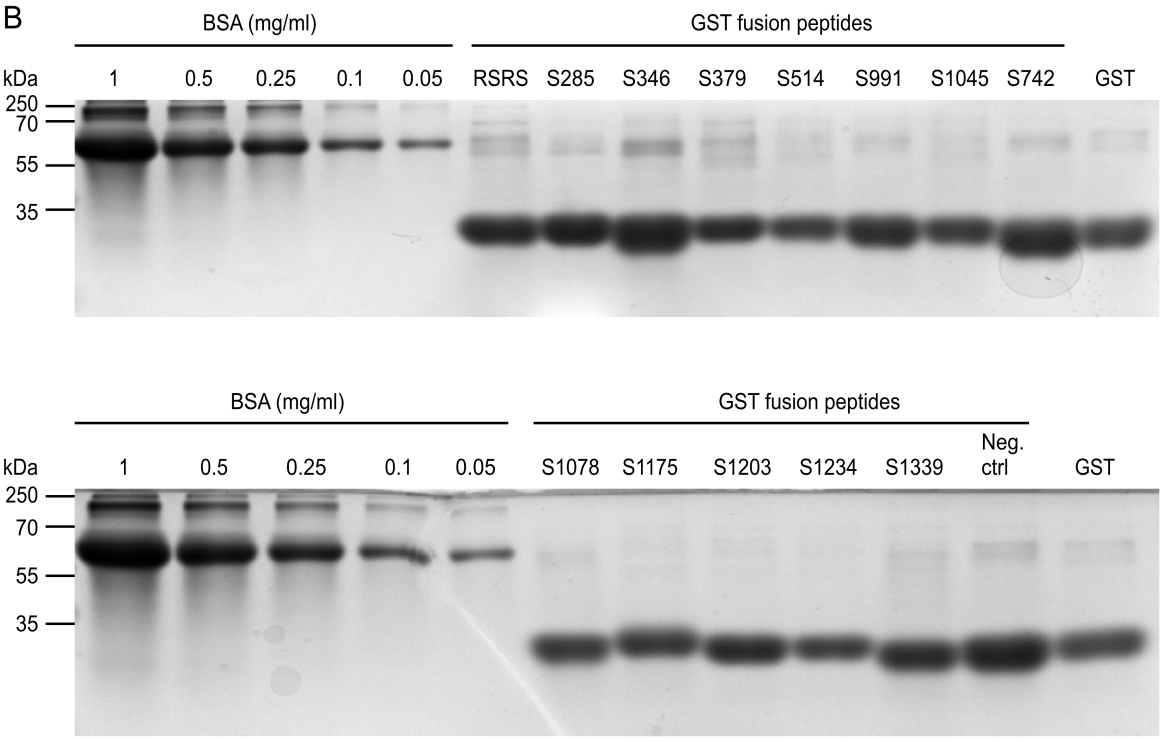
B
BSA (mg/ml)
GST fusion peptides
kDa
1 0.5 0.25 0.1 0.05
RSRS S285 S346 S379 S514 S991 S1045 S742 GST
250
70
55
35
BSA (mg/ml)
GST fusion peptides
kDa
1 0.5 0.25 0.1 0.05
S1078 S1175 S1203 S1234 S1339 Neg. ctrl GST
250
70
55
35

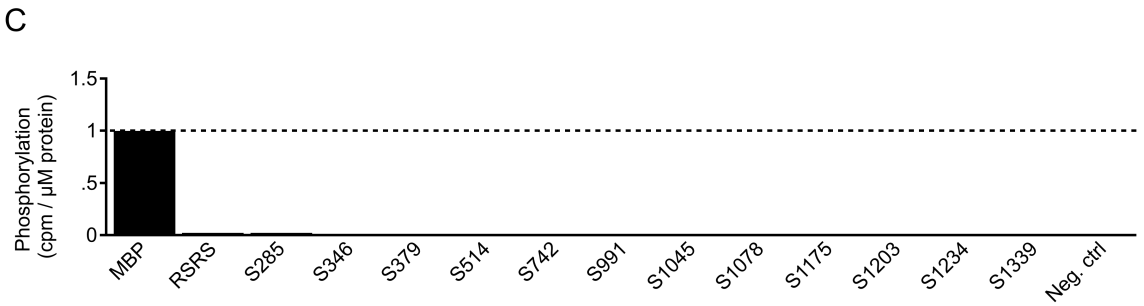
C
Phosphorylation (cpm / µM protein)
1.5
1
.5
0
MBP
RSRS
S285
S346
S379
S514
S742
S991
S1045
S1078
S1175
S1203
S1234
S1339
Neg. ctrl

Figure 5.11: SRPK2 does not phosphorylate RIM1 peptides.
(A) Cartoon depicting the nomenclature of the cloned RIM1 peptides. Serine of interest is positioned in the middle of the peptide (Position 0: P0). Positions of amino acids located N-terminal to the serine are labeled with position +1 (P+1) up to +6 (P+6), while positions C-terminal of the serine are indicated with negative numbers (P-1 to P-6). **(B)** RIM1 peptides were overexpressed in BL21 *Escherichia coli.* Coomassie gels indicating that RIM1-peptides were approximately set to a concentration of 0.5 mg/ml. Residues are labeled using rat nomenclature of RIM1. **(C)** Successful *in vitro* phosphorylation of myelin-basic protein (MBP) but not of RIM1 peptides by SRPK2. Data are shown as mean ± SEM. N = 2.

5.1.2.3.2 SRPK2 directly phosphorylates RIM1

To avoid this problem, RIM1 was divided into two fragments, the Zn-PDZ domains (1-663 amino acids) and the C2A-C2B domains (685-1615 amino acids) (Figure 5.12.A). The domains were fused to GST and *in vitro* phosphorylated using radioactive phosphate (Figure 5.12.B and 5.12.C). Both fragments were phosphorylated by SRPK2, with a higher phosphorylation rate for the C2A-C2B domains. This points to a higher abundance of phosphorylation sites within the C2-domains. Next, RIM1 was divided into four fragments to identify the highest abundance of phosphorylation sites within the protein (Figure 5.12.A and 5.12.D). All fragments were phosphorylated by SRPK2 (Figure 5.12.E). The highest phosphorylation rate was identified in fragment 3, which contained the C2A domain. In conclusion, the *in vitro* phosphorylation proved that RIM1 is a direct target of SRPK2 and is phosphorylated at multiple sites.

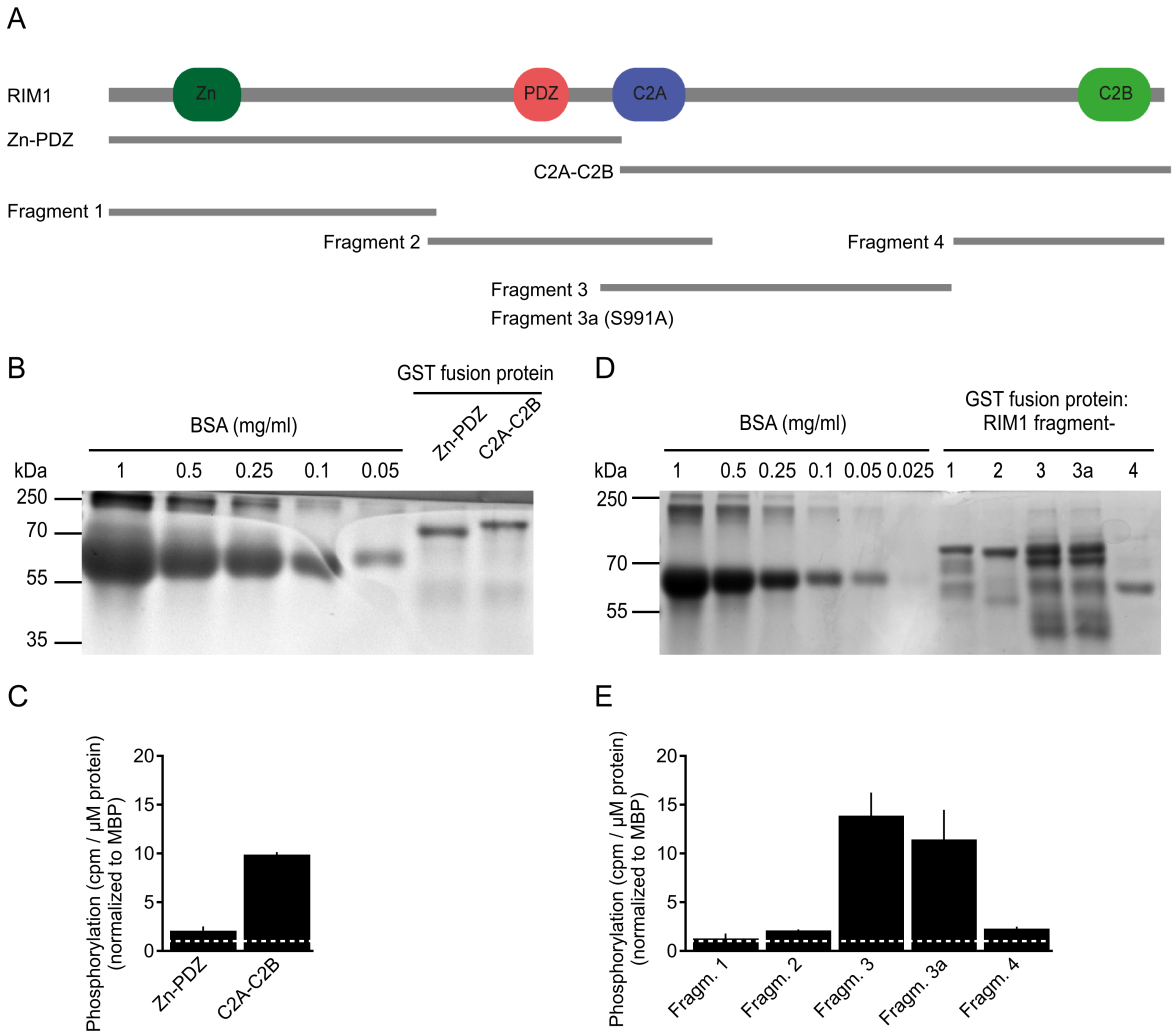

Figure 5.12: SRPK2 directly phosphorylates RIM1.

(A) Structure of RIM1 and cartoon depicting the fragments that were fused to GST. **(B)** GST-RIM1 domains were overexpressed in BL21 *Escherichia coli* and *in vitro* phosphorylated by SRPK2. **(C)** Radioactive quantification of *in vitro* phosphorylation of GST-Zn-PDZ and GST-C2A-C2B with SRPK2. N = 4. Data are shown as mean ± SEM. **(D)** GST-RIM1 fragments were overexpressed in BL21 *Escherichia coli* and *in vitro* phosphorylated by SRPK2. **(E)** Radioactive quantification of *in vitro* phosphorylation of Fragments 1-4 fused to GST with SRPK2. N = 3. Data are shown as mean ± SEM. Myelin-basic protein (MBP) was used as a positive control for all *in vitro* phosphorylation assays.

5.1.2.3.3 Identification of direct phosphorylation sites in RIM1

Our next goal was to identify specific phosphorylation sites in RIM1. Therefore, GST-Zn-PDZ and GST-C2A-C2B were *in vitro* phosphorylated and phosphorylation sites

were identified using mass spectrometry (MS performed by Mark Graham and bioinformatic analysis by Ash Waardenberg, Sydney, Australia). The MS analysis identified several direct phosphorylation sites in RIM1 by SRPK2 (Figure 5.13.A). In total, 21 phosphorylation sites were identified. Between the Zn and PDZ domain 11 phosphorylation sites were detected and 10 between the C2 domains. The sites marked in black were only found in the *in vitro* phosphorylation assay while the red phosphorylation sites indicate the overlap with sites that were found in SRPK2 overexpressing neurons. In our data set, a preference of SRPK2 to phosphorylate serines was found, as 20 out of 21 phosphorylation sites were serines. Only a single regulated threonine (T243) was detected. None of the identified sites was within a structural domain of RIM1 but in low complexity regions between the domains.
Phosphorylation sites that were regulated in neurons either overexpressing SRPK2 or in the SRPK2 knock-down but not identified as a direct phosphorylation site in the *in vitro* phosphorylation assay (Figure 5.13.A), represent indirect phosphorylation sites (Figure 5.13.B).

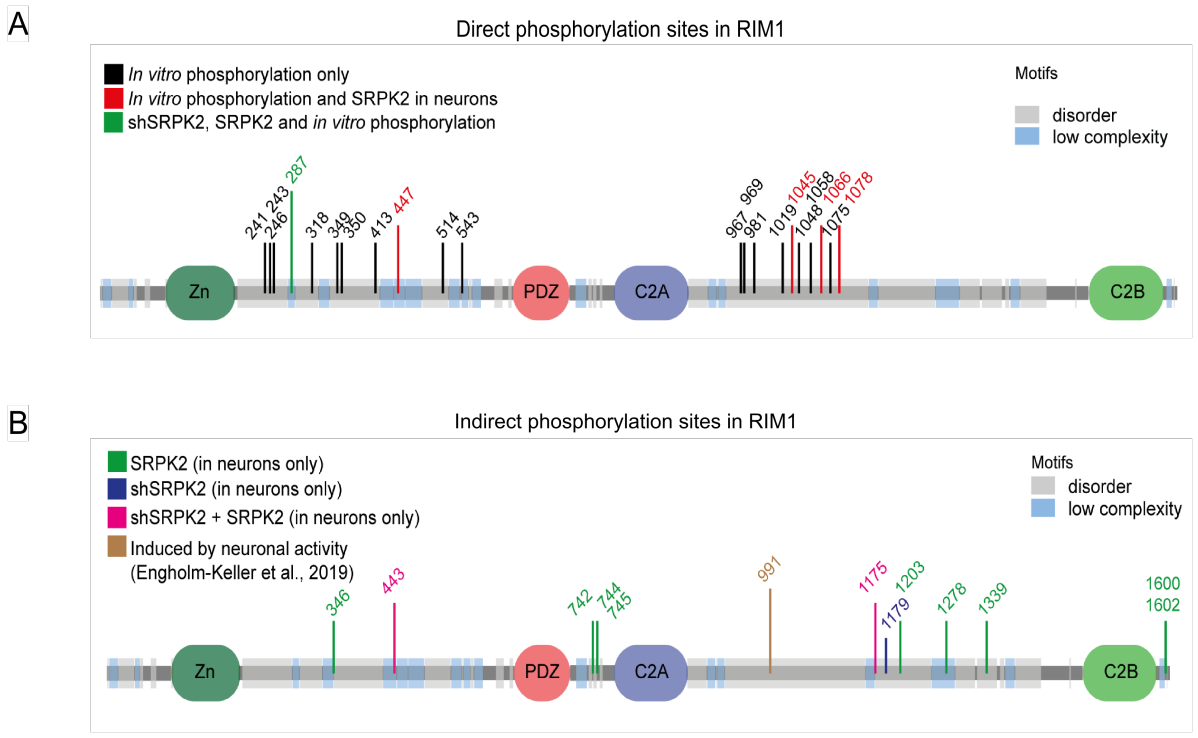

Figure 5.13: Identification of direct RIM1 phosphorylation sites by SRPK2.
(A) Direct RIM1 phosphorylation sites (rat nomenclature) were identified by *in vitro* phosphorylation of GST-Zn-PDZ and GST-C2A-C2B by SRPK2 and subsequent mass spectrometry analysis. All indicated sites were identified in the *in vitro* phosphorylation assay. Red sites were additionally found in SRPK2 overexpressing neurons and green highlights sites that were in addition downregulated in SRPK2 knock-down. **(B)** Indirect RIM1 phosphorylation sites. Green sites were upregulated in neurons when SRPK2 was overexpressed while blue sites were downregulated in SRPK2 knock-down. Pink indicates sites that combined both, upregulation for SRPK2 overexpression and downregulation for SRPK2 knock-down. S991 (brown) was identified by Engholm-Keller et al. (Engholm-Keller *et al.*, 2019) as an activity-regulated site.

5.1.3 Synaptic interacting partners of SRPK2

5.1.3.1 SRPK2 binds specifically RIM1 and ELKS1/2

Next, we wanted to identify down-stream effectors of SRPK2. Therefore, SRPK2-HA was overexpressed in HEK293T cells and immunoprecipitated. Simultaneously, synaptosomes from brain homogenates were prepared and lysed. SRPK2-HA was used to pull down presynaptic active zone members. Surprisingly, only RIM1 and ELKS1/2 were bound by SRPK2 (Figure 5.14.A). The interaction of SRPK2 with RIM1 (2.7 % ± 1.83 of the input) was stronger than with ELKS1/2 (0.5% ± 0.29 of the input) (Figure 5.14.B). Other AZ proteins like RIM-BP2, Munc13-1 and Liprin-α3 were not bound by SRPK2.

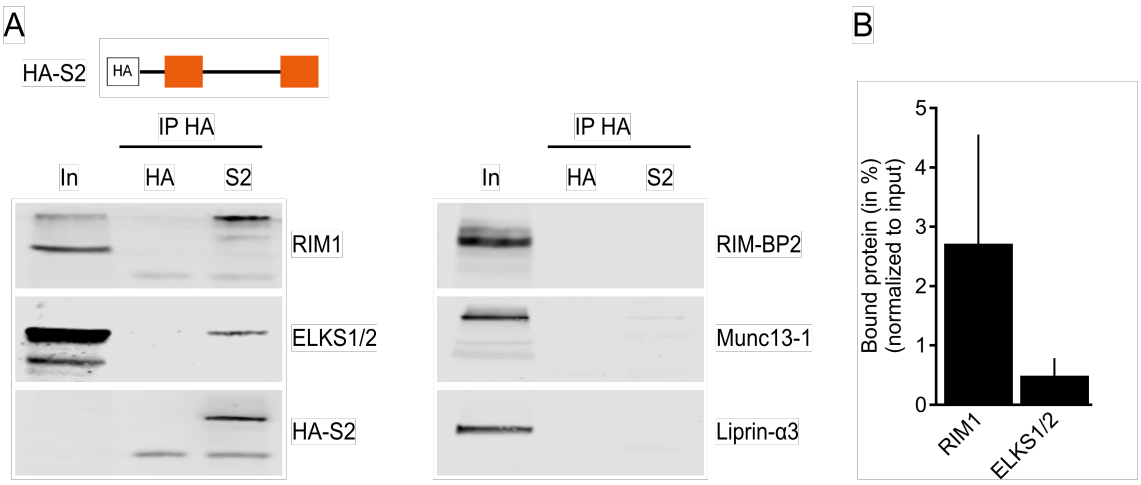

Figure 5.14: SRPK2 specifically binds RIM1 and ELKS1/2.
(A) SRPK2-HA and HA-tag were immunoprecipitated from HEK293T cells, incubated with lysed mouse synaptosomes and to pull down synaptic interaction partners. Immunoblots were incubated with antibodies against various CAZ components, N = 3 for each protein, except ELKS1/2 N = 4. **(B)** Quantification of binding normalized to input. Data are shown as mean ± SEM.

5.1.3.2 Kinase activity stabilizes the interaction of SRPK2 with RIM1 and ELKS1/2

Furthermore, the importance of the kinase activity of SRPK2 for the interaction with RIM1 and ELKS1/2 was evaluated. Therefore, a kinase-dead version of SRPK2 was cloned (S2-kDead) in which lysine 108 was replaced by arginine (Jang *et al.*, 2008). GFP-tagged SRPK2-WT and SRPK2-kDead as well as GFP as a control were overexpressed in HEK293T cells. All three samples were immunoprecipitated and subsequently employed to pull down synaptic proteins prepared from lysed synaptosomes. The binding of SRPK2 to RIM1 and ELKS1/2 was reduced in SRPK2-kDead compared to SRPK2-WT (RIM1: 0.71 ± 0.14 normalized to SRPK2-WT; ELKS1/2: 0.53 ± 0.12, Figure 5.15.A). The lack of binding to RIM-BP2, Munc13-1 and Liprin-α3 was confirmed in this set of experiments. The reduced binding of SRPK2 to RIM1 and ELKS1/2 highlights the importance of the kinase activity of SRPK2 for the interaction with other proteins.

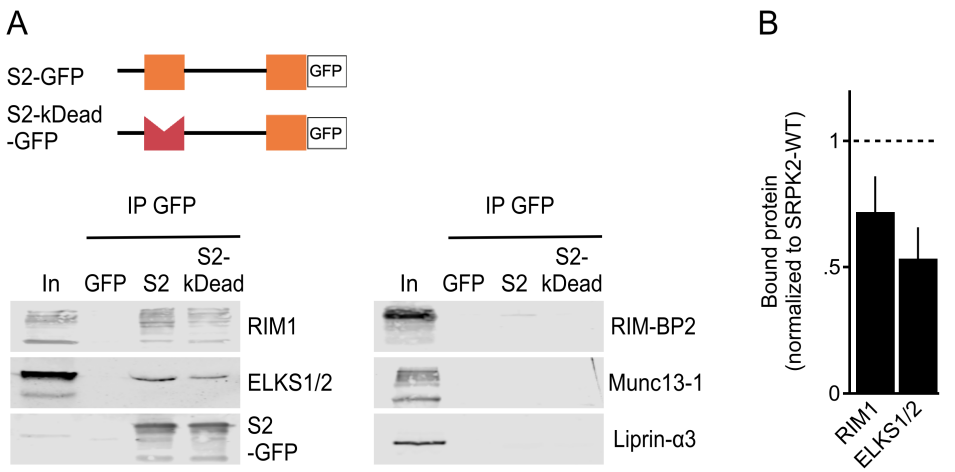

Figure 5.15: Kinase activity of SRPK2 stabilizes binding to RIM1 and ELKS1/2.
(A) SRPK2 bound RIM1 and ELKS1/2 in a kinase activity dependent manner. SRPK2-WT-GFP (S2-WT-GFP), SRPK2-kinase dead (S2-kDead)-GFP and GFP alone were immunoprecipitated from HEK293T cells and used to pull down synaptic interaction partners from lysed synaptosomes. N = 3 for each protein, except for ELKS1/2 N = 5. **(B)** Quantification of the binding of SRPK2 WT and SRPK2 kinase-dead to RIM1 and ELKS1/2. Data are shown as mean ± SEM.

5.1.3.3 Binding of RIM1 does not depend on specific phosphorylation sites

Phosphorylation is known to stabilize protein-protein interactions (reviewed in Nishi *et al.*, 2014). Thus, we wanted to analyze if specific phosphorylation sites in RIM1 would influence the binding of SRPK2. We focused on three different serines: S742, S991 and S1045 (rat nomenclature). Serine 745 was found to be regulated in the first phosphoproteomic screen in both overexpression and knock-down of SRPK2 (Figure 5.9, Serine 563 in the mouse nomenclature). We chose S991 because of its activity-dependent regulation (Engholm-Keller *et al.*, 2019). Additionally, we analyzed S1045 because it is a direct target of SRPK2 (Figure 5.13). For all three phosphorylation sites of interest, we investigated a phospho-deficient mutation to alanine (A) and a phospho-mimicking mutation to glutamate (E) with regard to SRPK2 binding. SRPK2 was co-expressed with the indicated RIM1 mutants in HEK293T cells. The efficiency of the RIM1-SRPK2 binding was evaluated using a co-immunoprecipitation (Figure 5.16). Interestingly, the binding of SRPK2 to RIM1 did not depend on one of the analyzed phosphorylation sites. The binding efficiency revealed a large scatter between experiments, however, no mutation clearly effected the interaction between SRPK2 and RIM1.

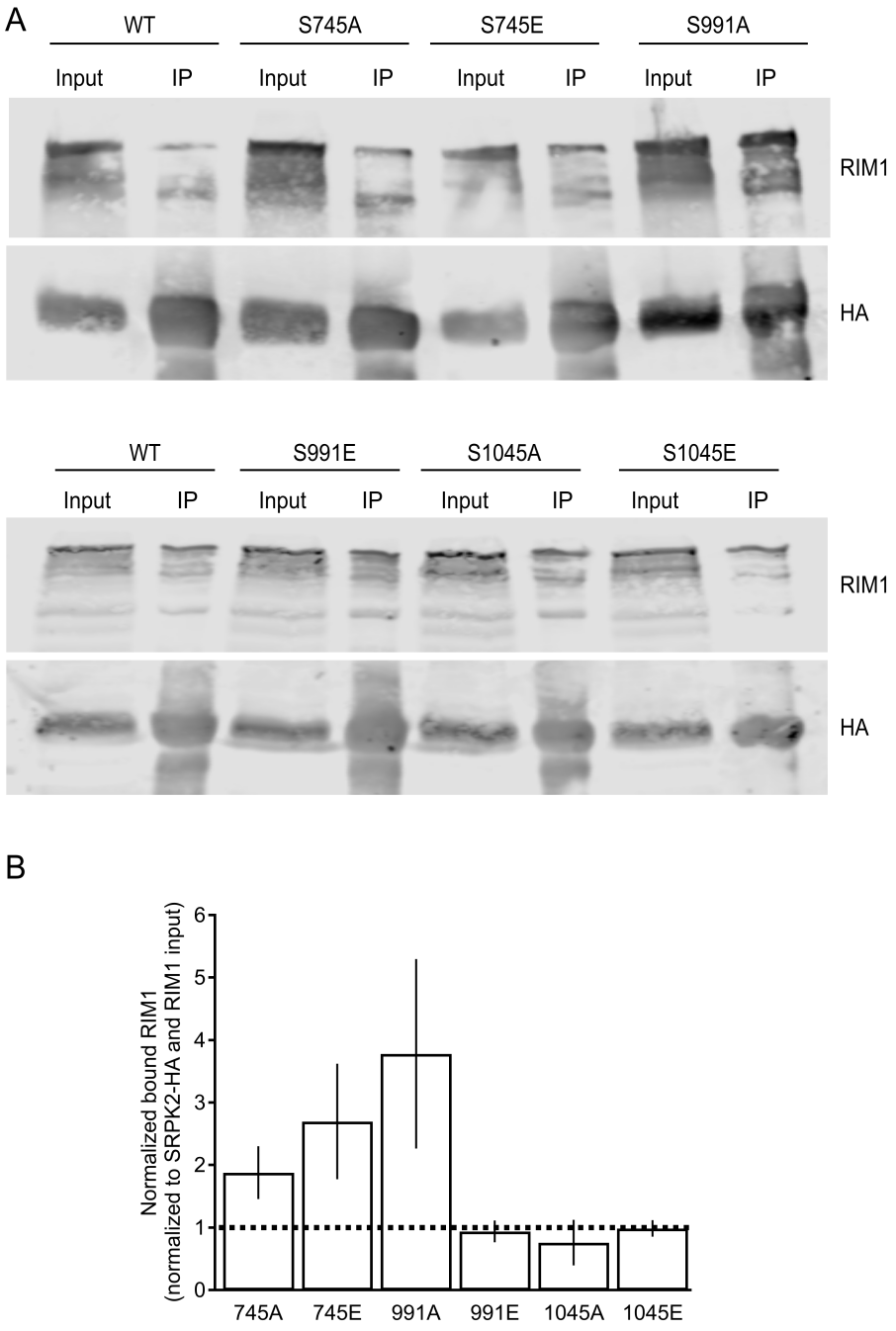

Figure 5.16: SRPK2-RIM1 binding does not depend on a specific phosphorylation site. **(A)** SRPK2 was overexpressed in HEK293T cells with the indicated phospho-deficient (A) and phospho-mimicking (E) mutants of RIM1. RIM1 mutants were co-immunoprecipitated with SRPK2 and binding of the RIM1 mutants was analyzed using immunoblots. **(B)** Quantification of SRPK2 binding to RIM1 mutants was normalized to RIM1-WT. N = 3. Data are shown as mean ± SEM. One-Way ANOVA, Holm-Sidak correction for multiple comparisons.

5.1.4 SRPK2 regulates abundance of AZ proteins

5.1.4.1 Whole cell protein levels of AZ proteins are regulated by SRPK2

We identified SRPK2 as an integral part of the synaptic membrane fraction (Figure 5.2) and demonstrated that it phosphorylates and interacts with RIM1 and ELKS1/2 (Figure 5.9, 5.10, 5.12 - 5.16). Thus, we wanted to investigate whether SRPK2 regulates the AZ composition as observed in *Drosophila melanogaster* (Johnson *et al.,* 2009; Nieratschker *et al.*, 2009). SRPK2 was overexpressed or knocked-down in cortical neurons and changes in protein levels of different AZ proteins were analyzed. Cortical neurons were lysed at DIV14-16 and whole cell protein levels were assessed by immunoblotting (Figure 5.17). SRPK2 overexpression resulted in a significant increase of RIM1 normalized to the control (2.63 ± 0.64). ELKS1/2 (1.61 ± 0.098) and synaptophysin (Syph) (1.64 ± 9.23) were also significantly increased when SRPK2 was overexpressed. Other AZ proteins like synapsin, liprin-α3, Munc13-1 and RIM-BP2 were not regulated by SRPK2. No protein was significantly changed in the SRPK2 knock-down.

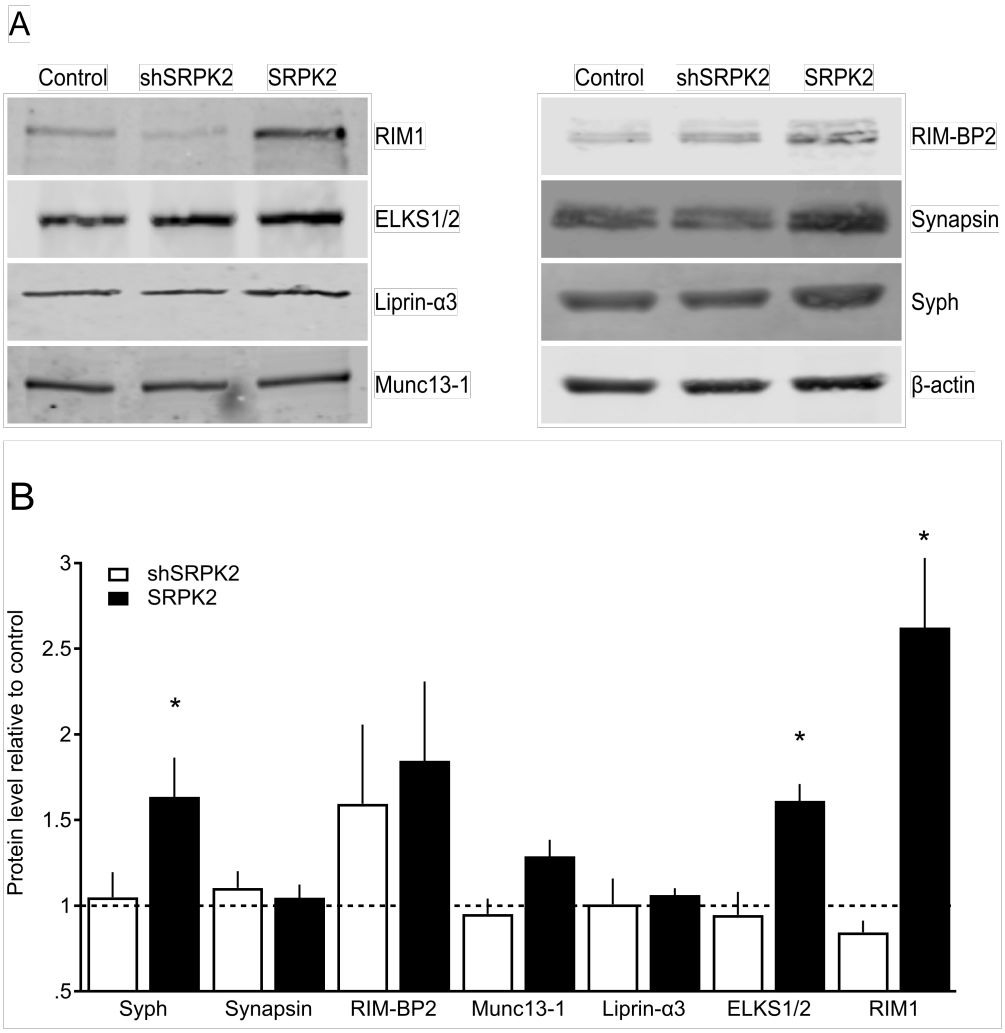

Figure 5.17: SRPK2 regulates protein levels of several AZ proteins.

(A) Cortical neurons were transduced with U6-GFP, shSRPK2-GFP or SRPK2-GFP rAAVs and lysed at DIV15. Whole cell protein levels were studied using immunoblot analysis. **(B)** SRPK2 OE resulted in significantly increased levels of RIM1, ELKS1/2 and synaptophysin. N = 5 for Synapsin, Synaptophysin (Syph), ELKS1/2, N = 4 for RIM1, N = 3 for RIM-BP2, Munc13-1, Liprin-α3. Data are shown as mean ± SEM. * $p < 0.05$, ns $p > 0.05$, One-Way ANOVA, Holm-Sidak correction for multiple comparisons.

5.1.4.2 Quantification of synaptic proteins using immunocytochemistry

The results of Figure 5.17 pointed to a regulatory role of SRPK2 for AZ protein levels. However, the data reflect the whole cell protein levels of the respective proteins. To analyze whether SRPK2 modifies synaptic protein levels, we decided to use immunocytochemical (ICC) stainings. Initially, we had to choose for a protein defining the synaptic area. Both synaptic vesicle proteins synapsin and synaptophysin were

suitable markers and were initially used for the study. Synaptophysin, however, was later withdrawn from the analysis because it is regulated by SRPK2 (Figure 5.17). Images were acquired as z-stacks with 5 planes in 0.3 µm steps using a confocal microscope with a 60X objective. For the analysis, images were imported to ImageJ and a maximum projection of the stack was prepared. First, the background was subtracted and the maximum intensity of synapsin was determined. The maximum intensity represented the higher threshold to define a synapse. The lower threshold was determined using a certain percentage of the maximum intensity. Different thresholds were applied and representative thresholds are shown in Figure 5.18. For the analysis, 20% of the maximum intensity was chosen as the lower threshold to define a synapse as a higher threshold like 30% excluded some synapses and reduced the synaptic area too much. A lower threshold like 10% of the maximum intensity included too much background and enlarged the synaptic area.

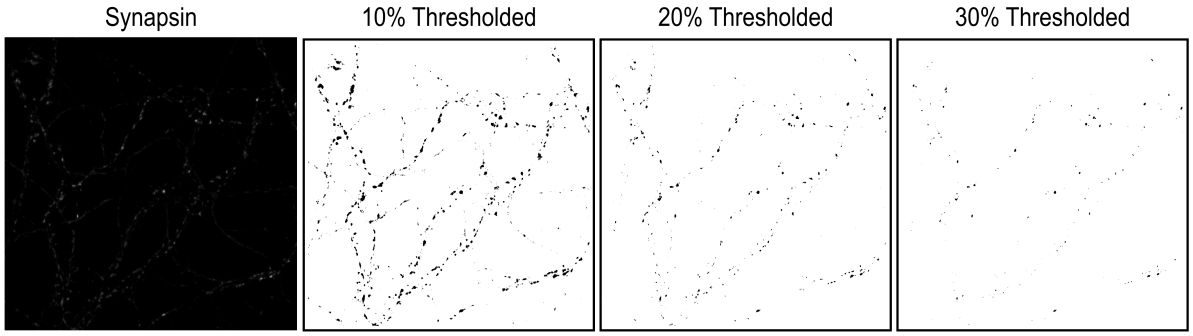

Figure 5.18: Threshold evaluation of synapsin staining using different intensity thresholds.

Hippocampal neurons were stained with synapsin. The maximum intensity was determined and different percentages of the maximum intensity were tested as the lower threshold.

The 20% thresholded synapsin staining was used to determine synapses using the 'Analyze particle' command (Figure 5.19.A). Only synapses with an area between 0.06 – 0.85 µm^2 were included. The synapsin-defined synapses are illustrated in red in Figure 5.19.B, in which they are superimposed on the thresholded synapsin image.

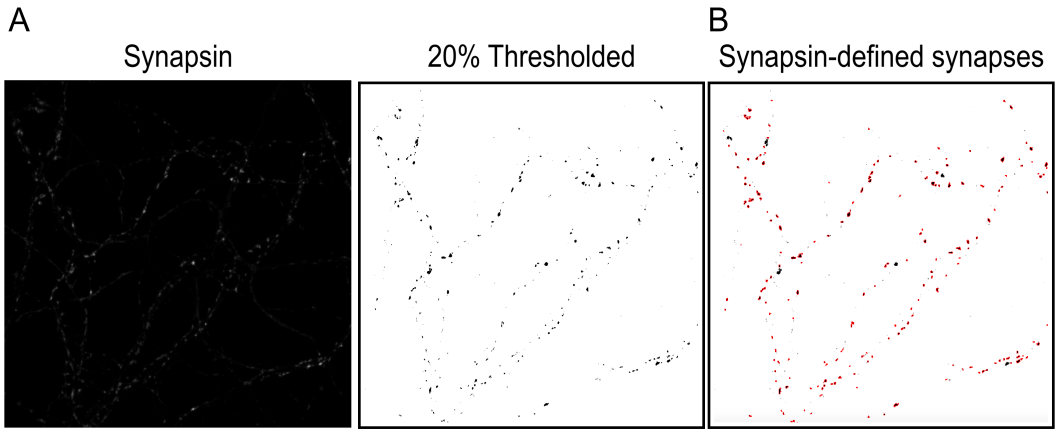

Figure 5.19: Definition of synapses using synapsin as a synaptic marker.
(A) Synapsin staining was used to define synapses. To define synaptic areas, 20% of the maximum intensity was used to set the lower threshold. **(B)** Synapsin-defined synapses in red are superimposed on the 20% thresholded synapsin staining.

To analyze synaptic AZ protein levels, synapsin was co-stained with various AZ proteins like RIM1 (Figure 5.20.A). The coverslips were mounted with fluorescent beads to normalize the measured fluorescence of the AZ proteins. One fluorescent bead can be seen in the RIM1 image. Synapses were defined as described above and subsequently superimposed on the AZ protein image (Figure 5.20.B). The fluorescence was measured within the synapses and then normalized to the maximum intensity of the fluorescent bead.

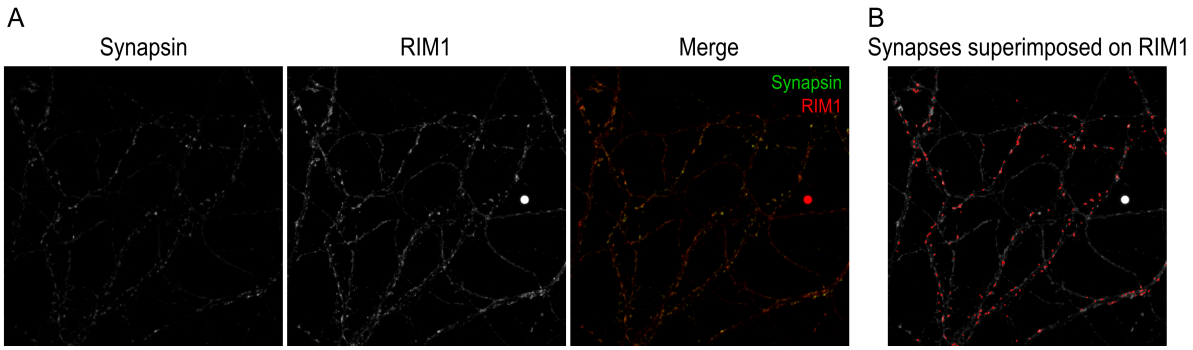

Figure 5.20: Analysis of synaptic AZ protein levels using ICC.
(A) Synapsin and RIM1 were co-stained. Red fluorescent beads were co-mounted to normalize the AZ protein fluorescence. **(B)** Synapsin-defined synapses were superimposed on RIM1 staining and RIM1 intensity was measured within the synapses. RIM1 intensities were normalized to the maximum intensity of the fluorescent bead.

5.1.4.3 SRPK2 changes synaptic RIM1 levels

Hippocampal neurons were transduced with GFP-control, shSRPK2-GFP or SRPK2-GFP rAAVs and fixed at DIV14. We focused for our analysis on four different AZ scaffold proteins: RIM1, bassoon, RIM-BP2 and ELKS1/2 (Figure 5.21.A-D).

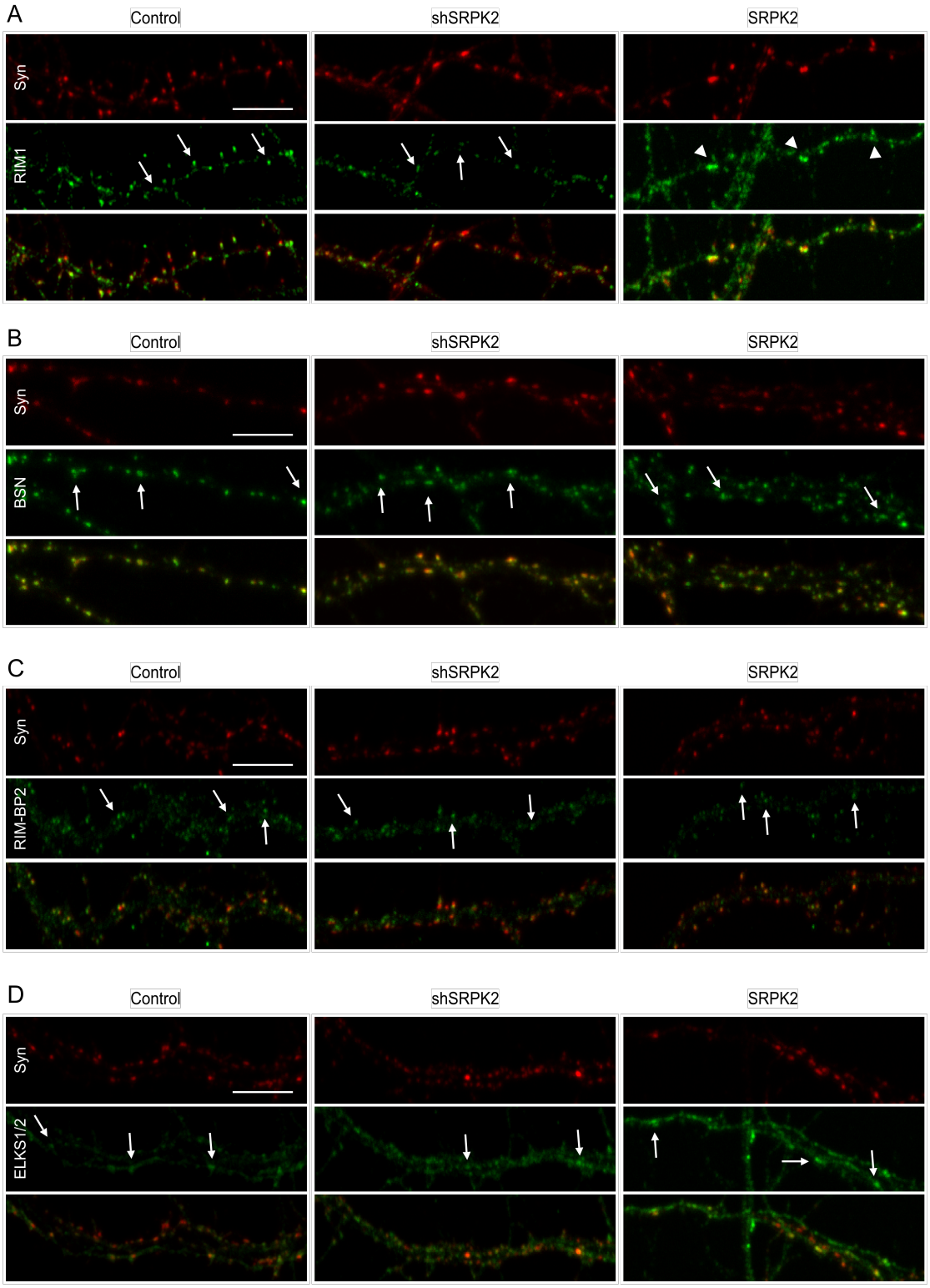

Figure 5.21: Overview of synaptic levels of different AZ proteins.
(A – D) Hippocampal neurons were transduced with U6-GFP, shSRPK2-GFP or SRPK2-GFP rAAVs and fixed at DIV15. Synapsin was co-stained with RIM1 (A), bassoon (B), RIM-BP2 (C) and ELKS1/2 (D). The fluorescence of the AZ proteins was measured in synapsin-defined synapses. Arrows indicate synapses with unaltered fluorescence intensity compared to control. Arrowheads indicate increase in fluorescence intensity. Scale bar: 10 µm.

Analysis of the ICC stainings showed no regulation of synaptic bassoon, RIM-BP2 or ELKS1/2 by SRPK2 (Figure 5.22). Synaptic RIM1 levels, however, were significantly increased when SRPK2 was overexpressed (1.36 ± 0.23 normalized to ctrl). The knock-down of SRPK2 reduced synaptic RIM1 but the change was not significant ($p = 0.09$). Our data suggests that SRPK2 regulates AZ protein levels and specifically impacts synaptic RIM1 level.

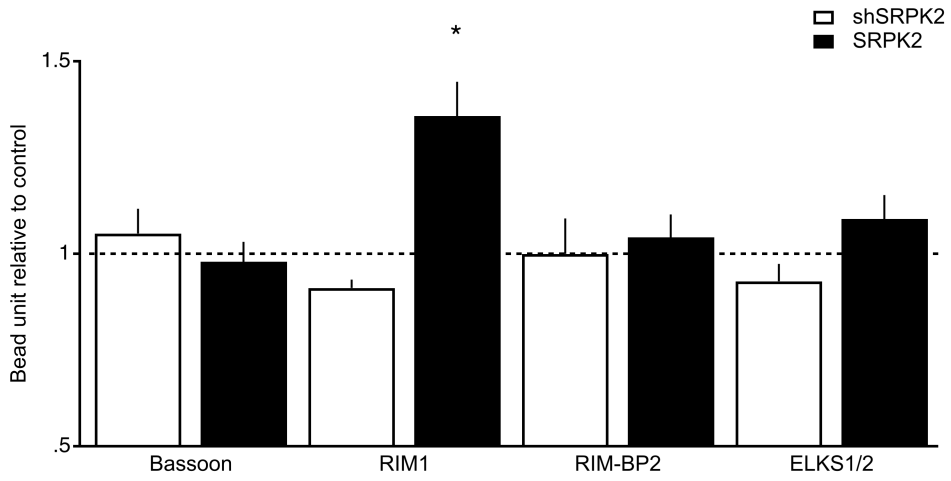

Figure 5.22: SRPK2 increases synaptic RIM1 levels.
Fluorescence intensities of AZ proteins within synapses were normalized to fluorescent beads. Data are shown as mean ± SEM. RIM1: N = 6 independent cultures, RIM-BP2 and ELKS1/2: N = 7, bassoon: N = 4. For each culture, 3 images were averaged for each rAAV transduction. * $p < 0.05$, ns $p > 0.05$, One-Way ANOVA, Holm-Sidak correction for multiple comparisons.

5.1.4.4 Synapse size is not determined by SRPK2

Additionally to the regulating role of SRPK2 on AZ protein levels, we wanted to address the question whether SRPK2 controls the size of synapses. Therefore, we analyzed the size of the synapses for the knock-down and overexpression of SRPK2

compared to the GFP control. The synapse size was 0.27 µm^2 ± 0.019 in the control and no change was observed in the knock-down or overexpression of SRPK2 (Figure 5.23).

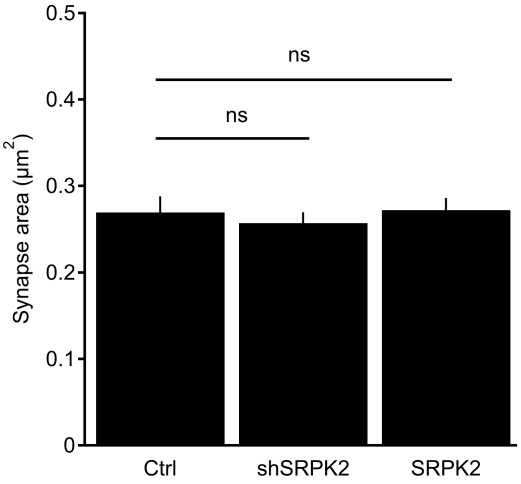

Figure 5.23: SRPK2 does not change the synapse size.

The area of synapses was quantified for 6 independent cultures with 3 technical replicates each. Data are shown as mean ± SEM. * $p < 0.05$, ns $p > 0.05$, One-Way ANOVA, Holm-Sidak correction for multiple comparisons.

5.1.4.5 SRPK2 does not modulate RIM1 transcription

SRPK2 is able to change the transcription of proteins (Jang *et al.*, 2008). To investigate whether SRPK2 regulates RIM1 transcription, SRPK2 was knocked-down or overexpressed in hippocampal neurons and mRNA was isolated. Afterwards, cDNA was synthesized and quantitative real time PCR was performed to analyze RIM1 mRNA levels (Figure 5.24). Interestingly, no significant change in RIM1 transcription was detected when SRPK2 levels were altered.

Therefore, the increase of RIM1 is not due to changes of the mRNA levels but due to a change on the protein level, which might be achieved by a higher stabilization of the phosphorylated RIM1 or an increased transport to the synapse.

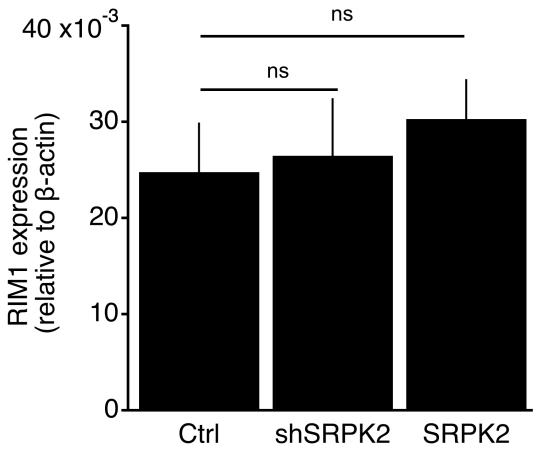

Figure 5.24: RIM1 transcription is not regulated by SRPK2.

Cortical neurons were transduced with U6-GFP, shSRPK2-GFP or SRPK2-GFP rAAVs and lysed at DIV15. Quantitative real time PCR was performed for three biological replicates. For each biological replicate, three to four technical replicates were used for the real time PCR. * $p < 0.05$, ns $p > 0.05$, One-Way ANOVA, Holm-Sidak correction for multiple comparisons.

5.1.4.6 SRPK2 regulates RIM1 stability

To investigate whether SRPK2 alters RIM1 degradation, we used emetine to irreversible block the elongation step during translation. Emetine was applied at DIV14/15 for 6 h before neurons were lysed and protein levels were analyzed using immunoblots (Figure 5.25). Emetine treatment did not change RIM1 protein levels in the control neurons. SRPK2 overexpression resulted in an increase of RIM1 protein levels as described previously (Figure 5.17). The inhibition of the translation significantly reduced RIM1 protein levels in SRPK2 overexpressing neurons compared to untreated neurons (Figure 5.25.B). Therefore, SRPK2 increases the degradation of RIM1. Nevertheless, the increased RIM1 levels in SRPK2 overexpressing neurons in the untreated condition compared to control neurons indicate that SRPK2 simultaneously increases RIM1 levels. This data shows that SRPK2 regulates both the translation as well as the degradation of RIM1.

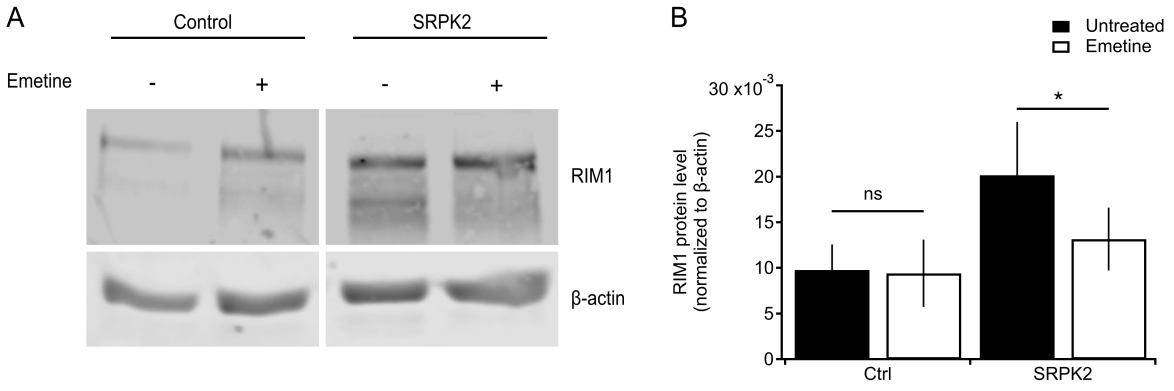

Figure 5.25: SRPK2 regulates RIM1 stability.

(A) Neurons were transduced with GFP- or SRPK2-GFP expressing rAAVs at DIV2-6. At DIV14/15, neurons were treated with 50 µM emetine or untreated for 6 h and subsequently lysed. **(B)** Quantification of protein levels. Data are shown as mean ± SEM. * $p < 0.05$, ns $p > 0.05$, paired ratio t-test. N = 5.

5.1.4.7 Specific phosphorylation sites in RIM1 do not impact RIM1 stability

To assess the importance of specific phosphorylation sites in RIM1 on the stability, we used again the phospho-mutants of RIM1 of serine 745, 991 and 1045 as previously (Figure 5.16). RIM1-WT, alanine- and glutamate-mutants of S745, S991 or S1045 were overexpressed in HEK293T cells and incubated with 50 µM emetine for 6 h to block translation. HEK293T were lysed and protein levels were assed using immunoblots (Figure 5.26). Inhibition of the translation resulted in a reduction of RIM1-WT levels compared to untreated cells (Figure 5.26.B, RIM1-WT: 0.78 ± 0.07). A similar reduction was observed for the phospho-mimicking mutant of S991 (S991E: 0.78 ± 0.02), while the phospho-mimicking mutant of S745E exhibited the most stabilizing effect (S745E: 1.07 ± 0.21). However, no significant increase for any tested phospho-mutant was observed. Thus, the three tested phosphorylation sites do not stabilize RIM1 protein level.

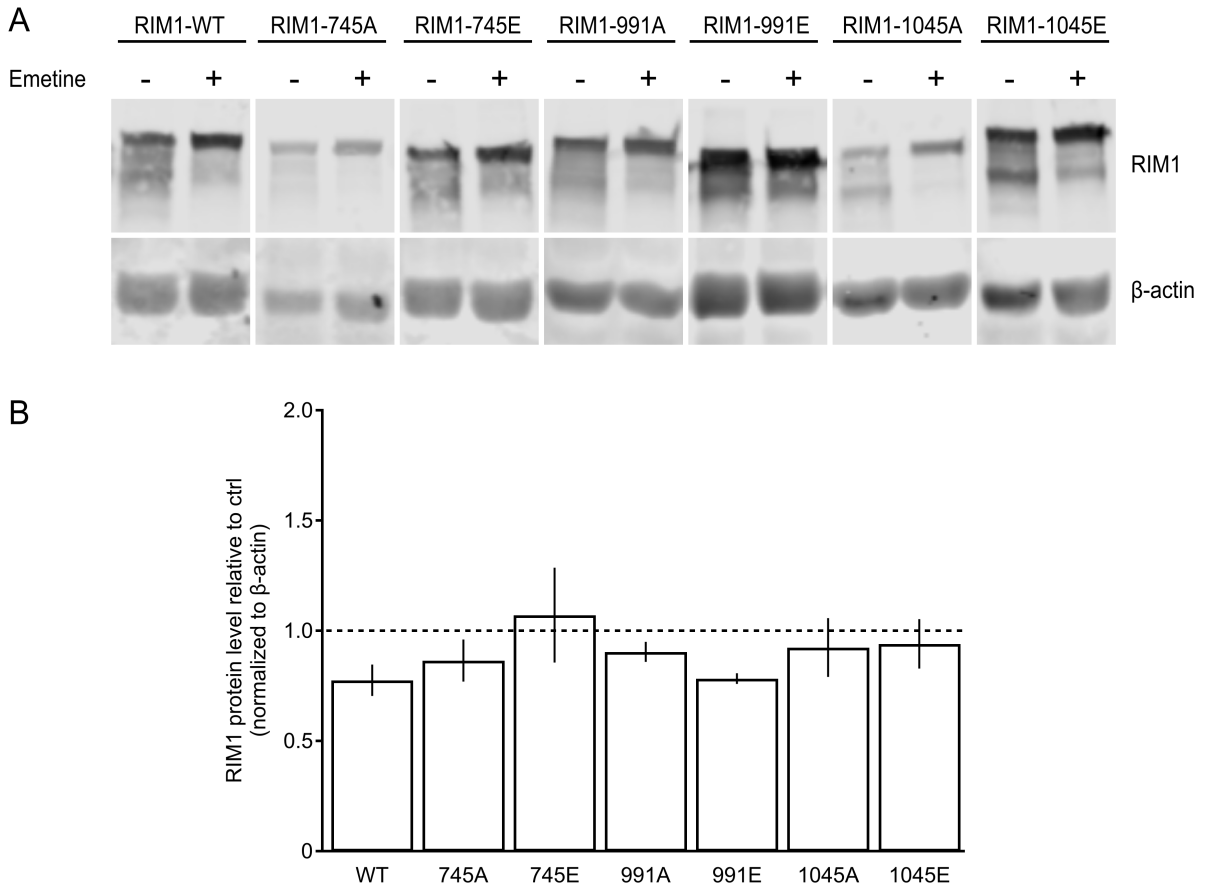

Figure 5.26: Specific phosphorylation sites in RIM1 do not impact RIM1 stability.
(A) RIM1-WT or indicated phospho-mutants were overexpressed in HEK293T cells. To inhibit the translation, cells were incubated with 50 µM emetine for 6 h. Cells were subsequently lysed and protein levels were assessed using immunoblots. **(B)** Quantification of RIM1 protein levels. All data are shown as mean ± SEM. N = 3. One-Way ANOVA, Holm-Sidak correction for multiple comparisons.

5.1.5 RIM1 clustering is controlled by SRPK2

5.1.5.1 Establishment of dSTORM cluster analysis

In the last years, superresolution microscopy facilitated researchers to look at the synapses on a nanoscale level. Work from the Blanpied laboratory showed that RIM1 nanoclusters at the synapse represent synaptic vesicle release sites (Tang *et al.*, 2016). Therefore, we wanted to investigate whether SRPK2 has an impact on the clustering of RIM1. For each investigated protein, the detection threshold of the

stochastically occurring blink events had to be determined. Different thresholds were investigated but for the analysis 8 photons/pixel were used for RIM1 because this settings excluded unspecific blink events. For our analysis, the distinction between synaptic and extrasynaptic clusters was important to analyze the impact of SRPK2 on RIM1 clusters in the synapse. Therefore, synapsin was used to determine the synaptic area. We followed the same approach as in the confocal analysis meaning we used 20% of the maximum synapsin intensity as a lower threshold to define a synapse (Figure 5.27).

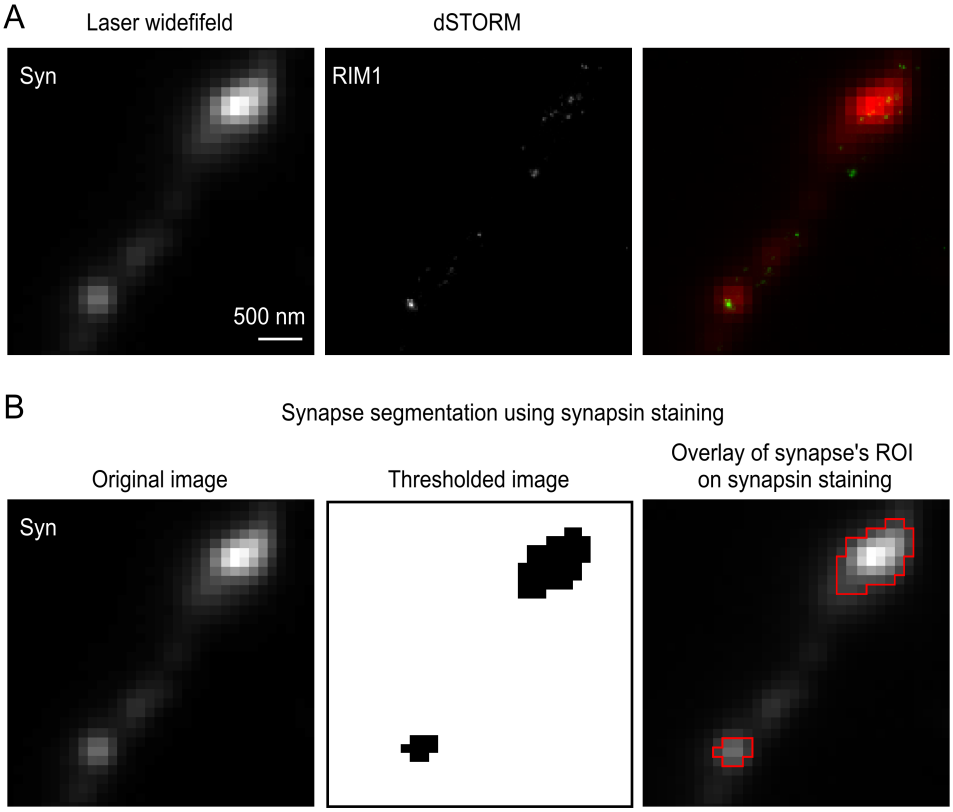

Figure 5.27: Definition of synapses using synapsin laser-widefield images.
(A) Co-staining of synapsin and RIM1. Synapsin was imaged using laser-widefield while RIM1 is illustrated using the density histogram of the dSTORM acquisition. **(B)** The maximum intensity of synapsin was measured and 20% of the grey scale value (left image) was used as a lower threshold to define a synapse illustrated in the middle image. Defined synapses are superimposed in red on the synapsin staining (right image).

The dSTORM image of RIM1 is represented as a density histogram indicating how many localizations were detected per pixel with a pixel size of 20 nm. The density histogram was imported to ImageJ and different thresholds of the RIM1 grey values were tested to identify an appropriate threshold to distinguish between non-clustered

and clustered RIM1 localizations. A lower threshold of 20 was used to exclude non-clustered RIM1 localizations from the analysis. Additionally, the clusters had to be larger than 800 nm^2 to be included in the cluster analysis. The defined RIM1 clusters were superimposed on the density histogram to indicate which RIM1 localizations represent clustered RIM1 localizations and which are non-clustered RIM1 localizations (Figure 5.28).

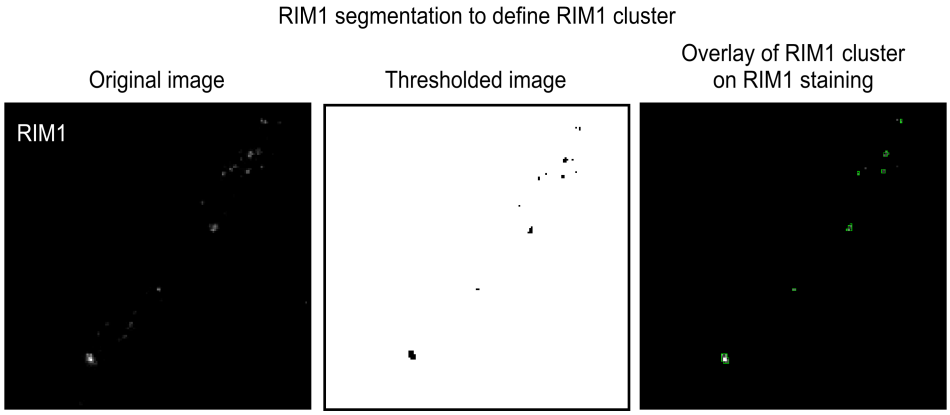

Figure 5.28: Definition of clustered RIM1 localizations.
Density histogram of RIM1 was used to distinguish between clustered and non-clustered molecules (left image). A grey value of 20 was used as lower threshold to define clustered RIM1 molecules, which are depicted in the middle image. Defined RIM1 clusters were superimposed in green on the density histogram of RIM1 (right).

To distinguish between synaptic and extrasynaptic RIM1 clusters, only RIM1 clusters that were completely in the synapsin-defined area (red) were counted as synaptic (Figure 5.29). In contrast, extrasynaptic clusters had to be completely outside of the synapse. RIM1 clusters that partially overlapped with the synapse were excluded from the analysis.

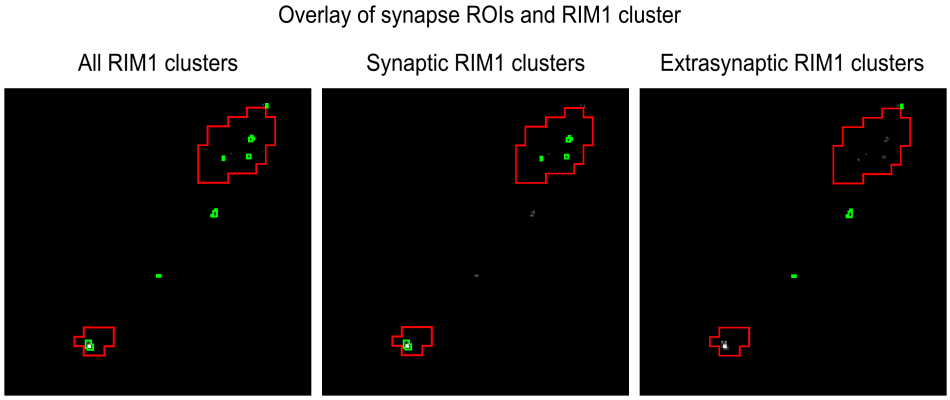

Figure 5.29: Distinction between synaptic and extrasynaptic clusters.
Synapsin-defined synapses were used to distinguish between axonal and synaptic RIM1 clusters (left image). Synaptic RIM1 clusters had to be completely inside the synapse (middle image). Extrasynaptic RIM1 clusters had to be completely outside of the synapse (right).

5.1.5.2 SRPK2 changes RIM1 clustering

Cortical neurons were transfected with shSRPK2-GFP, SRPK2-GFP or GFP. The transfection allowed tracing an individual axon, which was necessary because it was shown in *Drosophila melanogaster* that Bruchpilot was accumulated in the axon in the SRPK79D mutant (Johnson *et al.,* 2009; Nieratschker *et al.*, 2009). Co-staining of synapsin and RIM1 was conducted to perform the cluster analysis described in 5.1.5.1 (Figure 5.30).

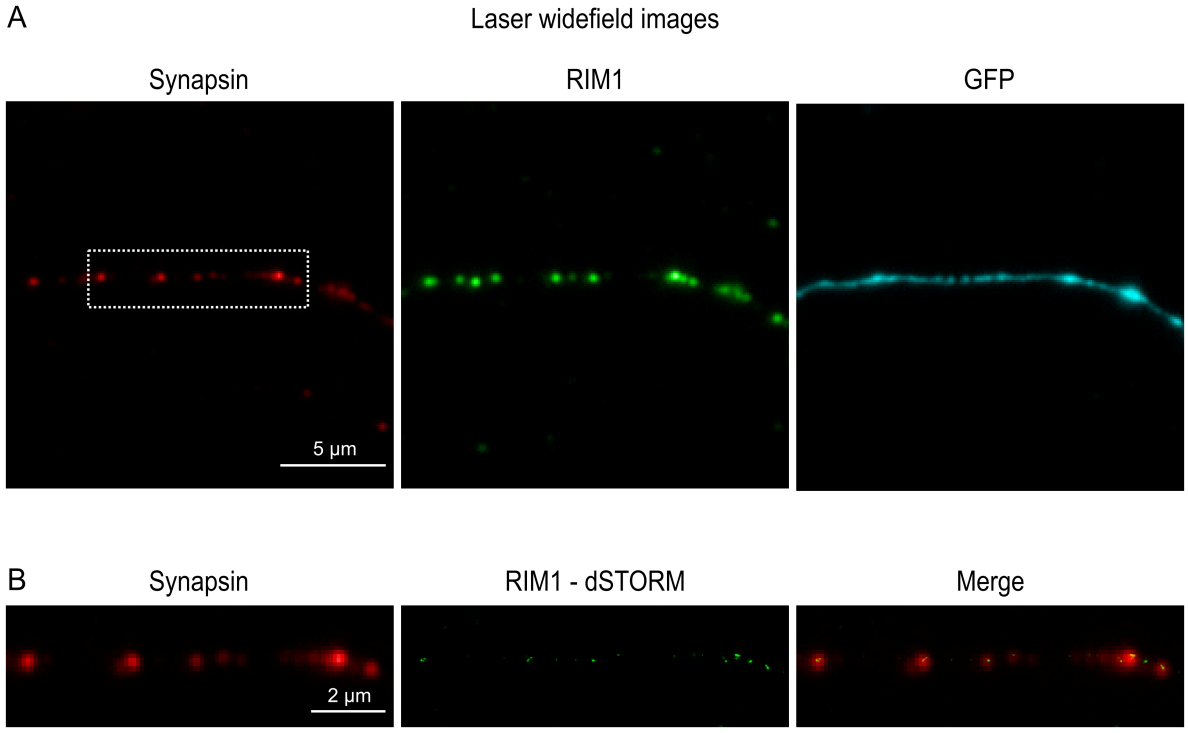

Figure 5.30: RIM1 clusters are located at the synapse.
(A) Co-staining of synapsin and RIM1 in GFP transfected neurons. A single axon was used to analyze RIM1 clusters. **(B)** Zoom-in of laser widefield synapsin and RIM1 dSTORM image.

Figure 5.31.A represents a single synapse and synaptic RIM1 clusters are superimposed on the synapsin staining. For a better visualization, the second panel represents a zoom-in on the synapse and only RIM1 clusters are depicted. Clustered RIM1 localizations that were superimposed on the synapse are highlighted in green while non-clustered RIM1 localizations are represented in gray.

RIM1 clusters were analyzed with respect to SRPK2 expression and a significant increase of synaptic RIM1 localizations in the SRPK2 overexpression was detected compared to the control (3.01 ± 1.2 normalized to ctrl, Figure 5.31.B). This data is in line with the confocal analysis of synaptic RIM1 in which increased RIM1 protein levels were demonstrated (Figure 5.22). Additionally, the knock-down of SRPK2 resulted in a significant decrease of synaptic RIM1 localizations by 67% (0.33 ± 0.06 normalized to ctrl). The change of synaptic RIM1 localizations by SRPK2 was also detectable in density maps with a radius of 15 nm (Mathematica scripts were generated by Terry McGovern). The increase of RIM1 localizations can be explained by different factors: The number of clusters could be changed as well as the area or the density of the clusters. Indeed, SRPK2 changed the number of RIM1 clusters per

synapse. In the control 1.5 ± 0.2 RIM1 clusters per synapse were detected (Figure 5.31.C). SRPK2 overexpression resulted in a significant increase to 4.3 ± 0.9 RIM1 clusters per synapse. In contrast, the knock-down SRPK2 decreased the cluster number significantly to 0.7 ± 0.2. In contrast, neither the RIM1 cluster area (Figure 5.31.D) nor the cluster density (Figure 5.31.E) was significantly changed by SRPK2.

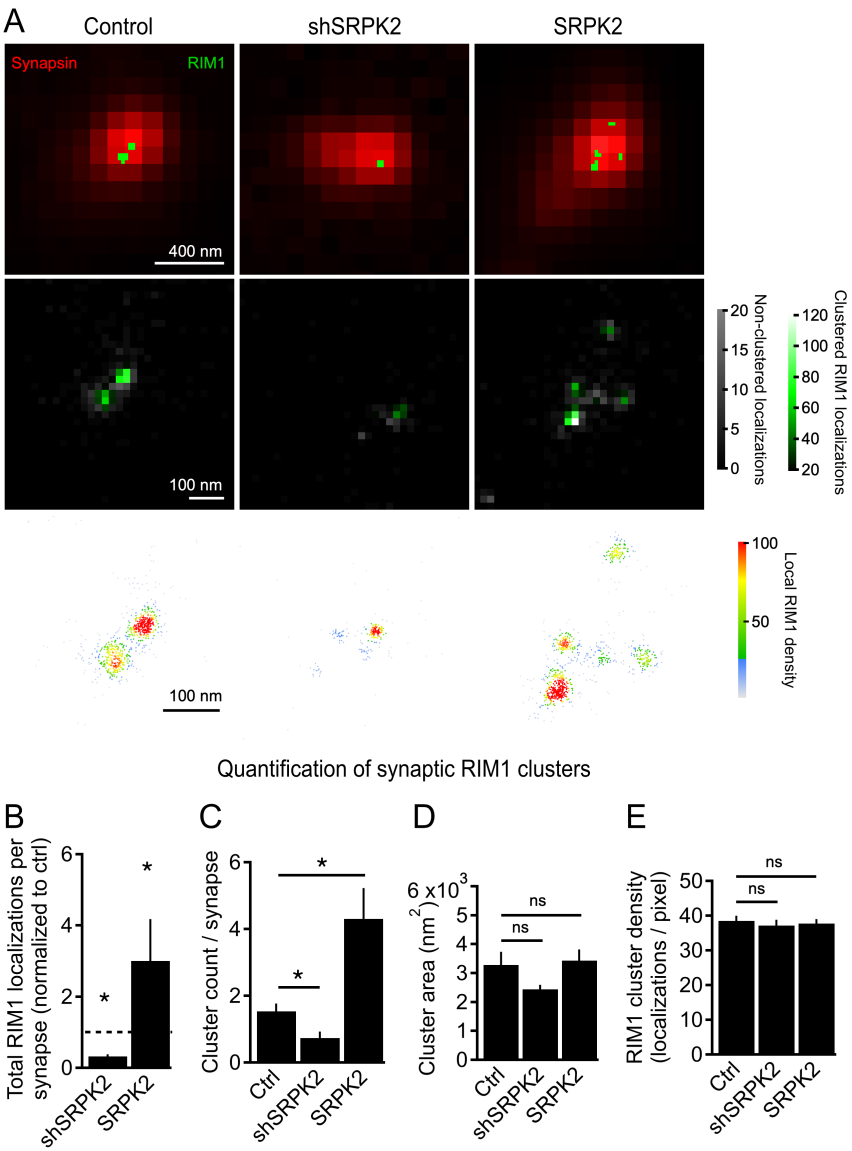

Figure 5.31: SRPK2 regulates synaptic RIM1 clusters.
(A) Neurons, transfected with GFP (Ctrl), shSRPK2-GFP or SRPK2-GFP, were immunostained for synapsin and RIM1. Detected synaptic RIM1 cluster (green) were superimposed on laser widefield synapsin staining (red). Second row indicates clustered RIM1 molecules (green) and non-clustered RIM1 molecules (grey scale). The lowest row shows density maps using a radius of 15 nm. **(B)** Total RIM1 localizations per synapse compared to control. **(C)** Number of RIM1 clusters per synapse. **(D)** Cluster area of synaptic RIM1 clusters. **(E)** RIM1 cluster density. All data are shown as mean ± SEM. N = 6. * $p < 0.05$, ns $p > 0.05$, One-Way ANOVA, Holm-Sidak correction for multiple comparisons.

The extrasynaptic RIM1 clusters were also investigated due to the axonal accumulation of Bruchpilot in *Drosophila melanogaster* (Johnson *et al.,* 2009; Nieratschker *et al.*, 2009). Here, the number of clusters was counted per axon since the axon length between the different conditions was not significantly changed (Ctrl: 12.3 µm ± 1.2, shSRPK2: 12.5 µm ± 0.7, SRPK2: 11.3 µm ± 1.2, Figure 5.32A). The number of RIM1 localizations per axon compared to the control was significantly increased for SRPK2 overexpression (4.01 ± 1.6, Figure 5.32.B). No change was observed for the SRPK2 knock-down (1.01 ± 0.3). Next, the number of RIM1 clusters per axon was analyzed (Figure 5.32.C). In the control 13.1 ± 3.7 clusters per axon were detected per axon, while overexpression of SRPK2 significantly increased the cluster number to 24 ± 2.9 clusters. Knock-down of SRPK2 resulted in a decrease of the RIM1 cluster number per axon to 8.7 ± 2.6, which was not significant ($p = 0.19$). Similar to the synaptic RIM1 clusters, neither the cluster area of extrasynaptic RIM1 clusters (Figure 5.32.D) nor the cluster density (Figure 5.32.E) was regulated by SRPK2.

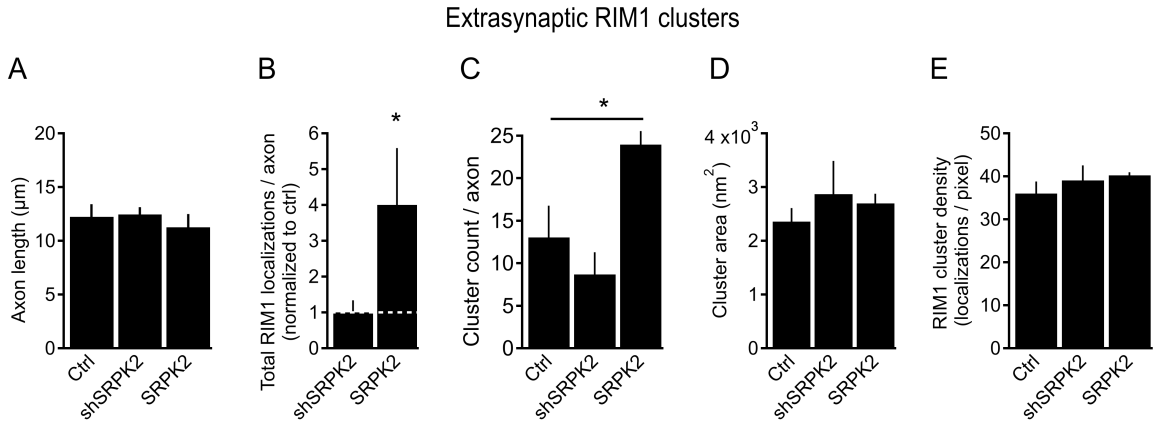

Figure 5.32: SRPK2 expression increases extrasynaptic RIM1 localizations.

(A) Axon length per acquisition **(B)** Total extrasynaptic RIM1 localizations per acquisition. **(C)** Number of extrasynaptic RIM1 clusters per acquisition. **(D)** Cluster area of extrasynaptic RIM1 clusters. **(E)** RIM1 cluster density. All data are shown as mean ± SEM. N = 6. * $p < 0.05$, ns $p > 0.05$, One-Way ANOVA, Holm-Sidak correction for multiple comparisons.

In summary, the data points to a mechanism in which SRPK2 stabilizes synaptic and extrasynaptic RIM1 clusters by phosphorylation. The stabilization results in an increased number of RIM1 clusters, which characterize release sites at the synapse.

5.1.5.3 Distribution of cluster size is not changed by SRPK2 expression

Our data demonstrated that the mean RIM1 cluster size was not changed (Figure 5.31.D), thus we investigated whether the distribution in cluster size was changed. To analyze whether SRPK2 shifts the distribution to smaller or bigger clusters, the cumulative frequency of the cluster area was calculated (Figure 5.33). However, no significant change in the distribution of synaptic and extrasynaptic RIM1 clusters was observed by modifying SRPK2 expression.

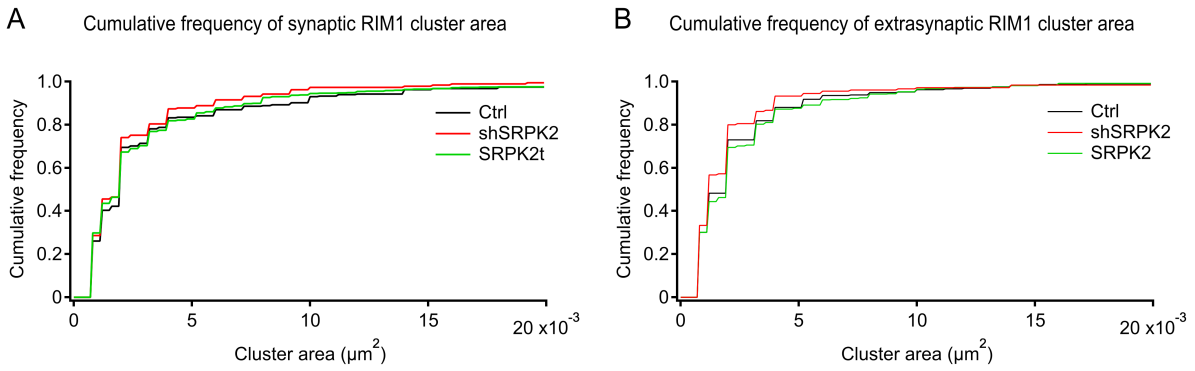

Figure 5.33: SRPK2 does not change the distribution of the RIM1 cluster size.
(A) Cumulative histogram of the cluster area of synaptic RIM1 clusters. **(B)** Cumulative histogram of the cluster area of extrasynaptic RIM1 clusters. Kolmogorov-Smirnov (K/S) test, $p > 0.05$. N = 6.

5.1.5.4 SRPK2 does not regulate non-clustered RIM1 molecules

To investigate the impact of SRPK2 on the non-clustered RIM1 molecules, the axon was segmented using the GFP laser-widefield image. All RIM1 localizations within the axon were measured. A region of interest (ROI) was drawn next to the axon to evaluate the local background. The background was subtracted from the measured RIM1 localizations resulting in the number of localizations that represent both non-clustered and clustered RIM1 molecules. The number of non-clustered RIM1 localizations was calculated by subtracting the number of clustered RIM1 localizations from the number of all RIM1 localizations. In total, 57% $\pm$ 4.4 of all RIM1 localizations were non-clustered in the control condition. Overexpression of SRPK2 resulted in a small reduction to 54% $\pm$ 2.4 of non-clustered RIM1 molecules. In knock-down of SRPK2 the fraction of non-clustered molecules was higher than in the control (68% $\pm$ 4.1) (Figure 5.34).

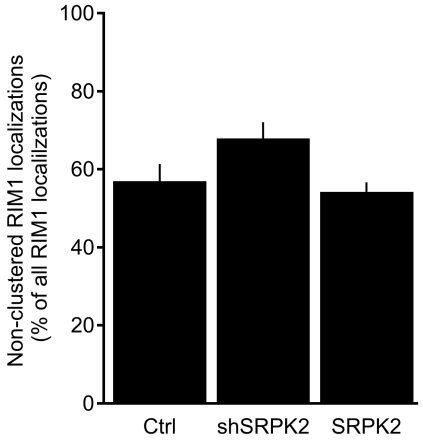

Figure 5.34: SRPK2 does not regulate non-clustered RIM1 localizations.
All RIM1 localizations per axon were measured and non-clustered RIM1 localizations were analyzed by subtraction of the clustered molecules from all RIM1 localizations. N = 6. Data are shown as mean ± SEM.

5.1.6 Role of SRPK2 in presynaptic homeostatic plasticity

5.1.6.1 SRPK2 protein levels are not altered in silenced cultures

It has been shown that homeostatic adaption of the neuronal network involves the remodeling of the neuronal network in both mammals and *Drosophila melanogaster* (Lazarevic *et al.*, 2011; Böhme *et al.*, 2019). Protein levels of the presynaptic cytomatrix were downregulated in silenced neurons (Lazarevic *et al.*, 2011). Therefore, the regulation of SRPK2 protein levels in response to activity was addressed. Neurons were treated with tetrodotoxin (TTX) for 48 h to induce homeostatic plasticity (HP) and SRPK2 levels were analyzed using immunoblotting (Figure 5.35.A). SRPK2 levels decreased in silenced neurons that were treated with TTX for 48 h but the change was not significant (Untreated: 0.17 ± 0.05, HP: 0.11 ± 0.05, Figure 5.35.B).

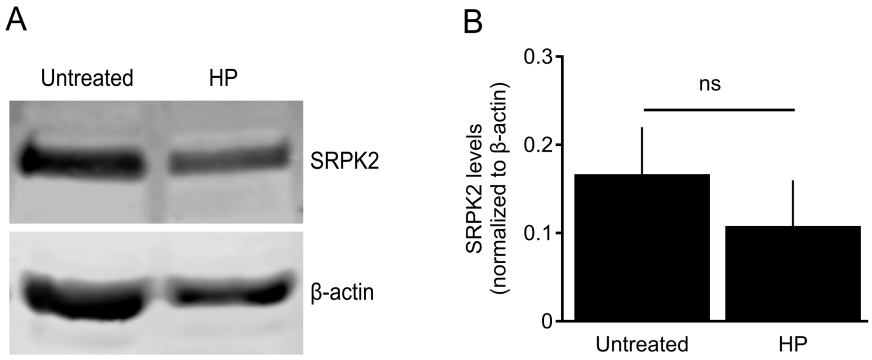

Figure 5.35: SRPK2 protein levels are not changed in silenced cultures.
(A) Neurons were incubated for 48 h with TTX (1 µM) and were lysed at DIV14-16. SRPK2 levels were analyzed using immunoblots. **(B)** No significant reduction of SRPK2 protein levels after HP induction. All data are shown as mean ± SEM. N = 4. * $p < 0.05$, ns $p > 0.05$, paired ratio t-test.

5.1.6.2 Presynaptic homeostatic plasticity induces translocation of SRPK2 to the presynapse

We used dual-color dSTORM to study the clustering of SRKP2 at the synapse with respect to neuronal activity. SRPK2 was co-stained with the postsynaptic marker Homer1 to distinguish between axonal and presynaptic SRPK2 clusters by imaging a single axon in cortical cultures. Homer1 is localized up to 100 nm from the synaptic

cleft in the postsynapse (Dani *et al.*, 2010). The exact localization of SRPK2 in the synapse has not been investigated so far. Our data supports that SRPK2 is an integral component of the presynaptic AZ (Figure 5.2). The density histograms of SRPK2 and Homer1 generated by the Leica Software were loaded in ImageJ and a grey scale threshold of 10 for SRPK2 and 20 for Homer1 was used to distinguish clustered from non-clustered molecules. The nearest Homer1 cluster of each SRPK2 cluster was measured using the line tool in ImageJ.

The distances for other AZ proteins to the synaptic cleft have already been reported. RIM1 is with ~35 nm localized closer to the synaptic cleft than Piccolo ~90 nm (Dani *et al.*, 2010). We defined SRPK2 clusters as presynaptic if they were within a 200 nm distance to a Homer1 cluster because SRPK2 would then be localized in a similar range as other AZ proteins. Presynaptic SRPK2 clusters are indicated in green while axonal clusters, which exhibit a larger distance than 200 nm to the closest Homer1 cluster are highlighted in yellow (Figure 5.36.A). Density maps with a radius of 15 nm were generated for a better visualization of the SRPK2 density. To investigate the impact of presynaptic homeostatic plasticity on presynaptic SRPK2 clusters, neuronal cultures were treated with TTX for 48 h to induce HP. Interestingly, only one synaptic SRPK2 cluster per synapse was detected (Figure 5.36.B)

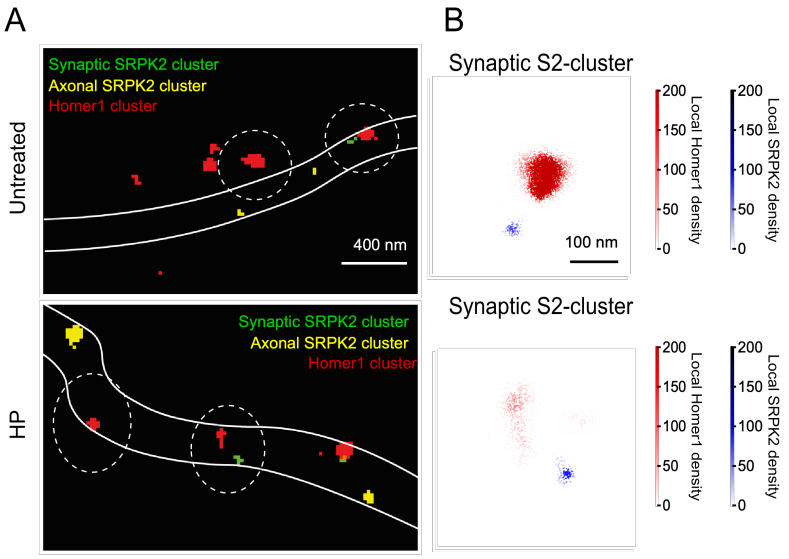

Figure 5.36: Definition of presynaptic SRPK2 clusters using dual-color dSTORM.
(A) Cortical neurons, untreated (Untr.) or incubated with 1 µM TTX for 48 h to induce HP, were stained with Homer1 and SRPK2 at DIV14/15. A single axon was imaged and dual-color dSTORM was used to localize Homer1 and SRPK2 clusters. Density histograms of both channels were loaded in ImageJ and an appropriate threshold for each staining (SRPK2: 10, Homer: 20) was used to define clustered molecules. The distance between SRPK2 and Homer1 clusters was measured using the line tool in ImageJ. Presynaptic SRPK2 clusters (green) are within a 200 nm distance to a Homer1 cluster (dotted line). **(B)** Density maps were generated using a radius of 15 nm.

All detected SRPK2 clusters were counted and the percentage of presynaptic SRPK2 clusters was calculated (Figure 5.37). Presynaptic silencing by incubation with TTX resulted in a significant increase of presynaptic clusters (Untr.: 35.12% ± 5.23, HP: 57.21% ± 4.91, Figure 5.37.A). Axonal SRPK2 clusters were significantly decreased (Untr.: 55.69% ± 3.75, HP: 36.2% ± 5.13), while no change was detected for postsynaptic SRPK2 clusters. The overall cluster count of SRPK2 clusters was unchanged (Figure 5.37.B) as well as the SRPK2 cluster area (Figure 5.37.C). Presynaptic homeostatic plasticity resulted in a significant decrease of Homer1 cluster area (Figure 5.37.D) without changing the Homer1 cluster count (Figure 5.37.E). This data indicates that SRPK2 undergoes a structural remodeling during homeostatic plasticity resulting in more presynaptic SRPK2 clusters.

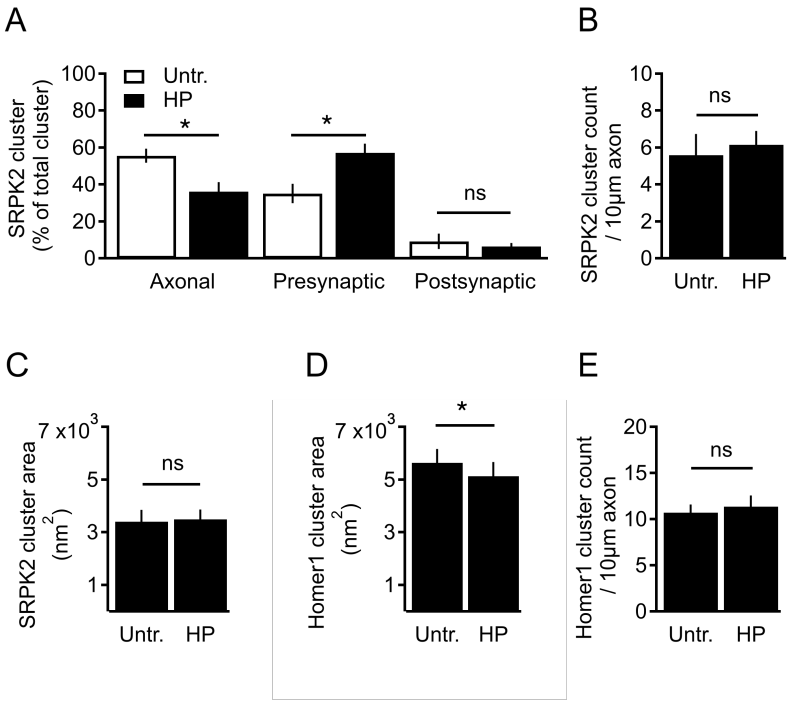

Figure 5.37: Presynaptic homeostatic plasticity increases presynaptic SRPK2 clusters. **(A)** Cortical neurons were incubated with TTX at DIV12-13 and fixed after 48 h. Neurons were stained with Homer1 and SRPK2. A single axon was imaged and dual-color dSTORM was used to localize Homer1 and SRPK2 clusters. The distance between SRPK2 and Homer1 clusters was measured using the line tool in ImageJ. Presynaptic SRPK2 clusters are within a 200 nm distance to a Homer1 cluster. Postsynaptic SRPK2 clusters overlap at least to 50% with a Homer1 cluster. All other SRPK2 clusters were characterized as axonal. **(B)** Quantification of number of SRPK2 clusters per 10 µm axon. **(C)** Quantification of SRPK2 cluster area. **(D)** Quantification of the Homer1 cluster area. **(E)** Quantification of the Homer1 cluster count per 10 µm axon. All data are shown as mean ± SEM. N = 6. * $p < 0.05$, ns $p > 0.05$, paired ratio t-test.

5.1.6.3 Presynaptic homeostatic plasticity increases synaptic RIM1 clusters

In our laboratory, it was recently shown that RIM1 is necessary to induce homeostatic plasticity (data not shown, PhD thesis Annika Mayer, unpublished; PhD thesis Alexander Müller, 2019). The importance of RIM1 to mediate homeostatic plasticity as well as its remodeling during homeostatic plasticity (Lazarevic *et al.*, 2011) triggered us to use superresolution microscopy to investigate the clustering of RIM1 during presynaptic homeostatic plasticity. Therefore, cortical neurons were treated with TTX for 48 h before fixation at DIV15. RIM1 was co-stained with synapsin and a single axon was imaged to investigate synaptic RIM1 clusters (Figure

5.38.A and 5.38.B). The cluster analysis was conducted as described in 5.1.5.1 using synapsin as a synaptic marker. Presynaptic homeostatic increased synaptic RIM1 clusters significantly compared to control neurons (Untr.: 2.44 ± 0.15, HP: 3.45 ± 0.39, Figure 5.38.C). All in all, the superresolution data points to a rearrangement of RIM1 and SRPK2 during presynaptic homeostasis that might mediate the increased neurotransmitter release during presynaptic homeostatic plasticity.

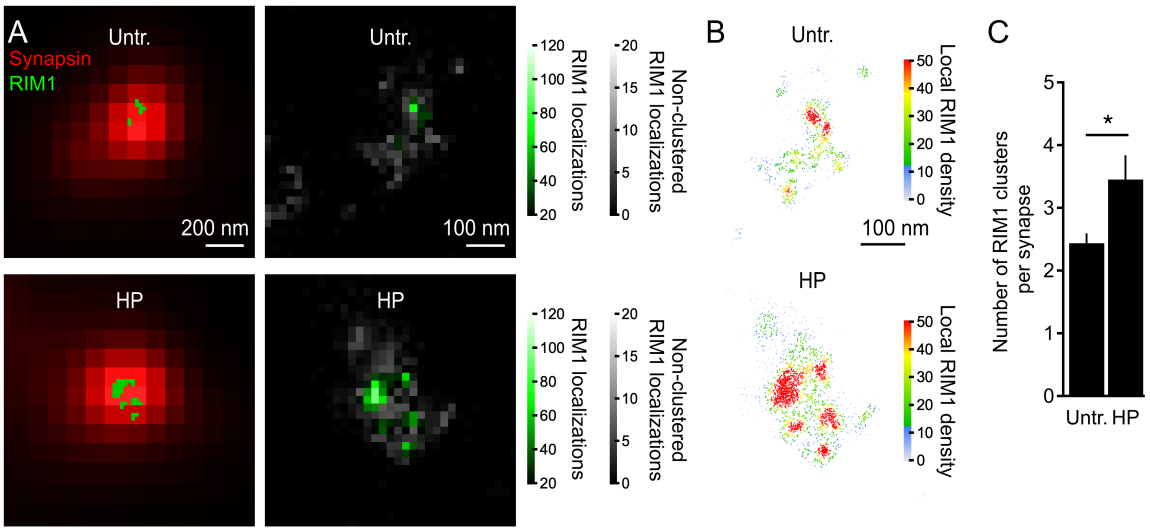

Figure 5.38: Presynaptic homeostatic plasticity increases synaptic RIM1 clusters.
(A) Cortical neurons were incubated with TTX at DIV12-13 and fixed after 48 h. Neurons were stained with synapsin and RIM1. A single axon was imaged and laser-widefield synapsin staining was used to define synapses as described in 5.1.5.1. **(B)** Density maps were generated using a radius of 15 nm. **(C)** Quantification for number of RIM1 clusters per synapse. All data are shown as mean ± SEM. N = 6. * $p < 0.05$, paired ratio t-test.

5.2 The differential proteome of synapses with and without RIM-dependent presynaptic plasticity

The variation in the proteome of distinct synapses became of interest as long-term plasticity (LTP) is differently regulated in Schaffer collateral and Mossy fiber (MF) synapses in the hippocampus (reviewed in Castillo, 2012). LTP expression in the CA3 pyramidal synapses requires the activation of postsynaptic NMDA receptors (Tsien *et al.*, 1996). In contrast, LTP in MF synapses is NMDA receptor independent and is expressed in a presynaptic manner (Zalutsky and Nicoll, 1990). MF LTP is mediated by the activation of protein kinase A (Weisskopf *et al.*, 1994). This form of plasticity is also found in cerebellar parallel fiber synapses (Salin *et al.*, 1996; Linden and Ahn, 1999). Expression of RIM1α is required for presynaptic LTP in MF synapses and cerebellar parallel fibers (Castillo *et al.*, 2002). However, short-term plasticity of MF synapses was not altered in RIM1α knock-out mice (Castillo *et al.*, 2002). The RIM1α dependence was not found for LTP in CA3 pyramidal cells (Schoch *et al.*, 2002). Moreover, short-term plasticity was impaired in RIM1α knock-out mice in CA3 pyramidal cells (Schoch *et al.*, 2002).
The expression of distinct types of LTP and different impacts on plasticity of the RIM1 KO raises the question about potential variances in the proteome of both synapses.

5.2.1 Establishment of fluorescence activated synaptosome sorting (FASS)

In the last years proteomic studies about the synapse identified multiple synaptic proteins which are enriched in the active zone or on synaptic vesicles (Schrimpf *et al.*, 2005; Takamori *et al.*, 2006; Filiou *et al.*, 2010). However, it was not possible to analyze the proteome of one specific synapse type rather than using a mixture of synapses. The laboratory of Etienne Herzog in Bordeaux established a new technique to enrich synapses of specific origin using a FACS sorter (Biesemann *et al.*, 2014). The target synapses are recognized by their green fluorescent signal by the sorter and sorted to enrich the synaptosomes of interest. In classical FACS, the sorter is triggered with the forward scatter (FSC) because cells are big enough to be differentiated by size. Synaptosomes however, are too small to be detected using the

FSC. Therefore, the synaptosomes were incubated with the dye FM4-64, which stains membranes and thereby enables the identification of small structures like synaptosomes using fluorescence (Biesemann *et al.*, 2014).
In our lab, we used a NG2-CreER-PSD95mVenus mouse line to establish the enrichment of NG2 synapses. Different settings were tested for the FACS ARIA III machine that enabled us to sort with a high precision and a low level of noise. Synaptosomes were prepared from whole brain homogenates. To separate synaptosomes from other contaminants like myelin, gliosomes and non-synaptic fragments, a sucrose gradient was prepared and the synaptosome fraction was recovered as described in Biesemann et al. (Biesemann *et al.*, 2014).

The wild-type sample was used to calibrate the system and as a negative control since there were no fluorescent synaptosomes present. The gate P1 includes all single synaptosomes while the gate P4 represents aggregated synaptosomes (Figure 5.39.A). The threshold for FM4-64 was set to 1000 to ensure that we sorted synaptosomes and that debris that might exhibit autofluorescence was not included in the sort. The synaptosome gate P1 was further divided into P2 and P3 (Figure 5.39.B). The difference between synaptosomes in P2 and P3 was the mVenus intensity, which is now depicted on the y-axis. The wild-type synaptosomes did not contain any fluorescence. Thus, all synaptosomes of P1 had to be in P2 (99.98 %). The gate of P3 is drawn in a way that no wild-type synaptosomes were detected in the gate P3. To verify that we sorted synaptosomes, we also analyzed the intensity of the FM4-64, which labeled synaptosomes (Figure 5.39.C).

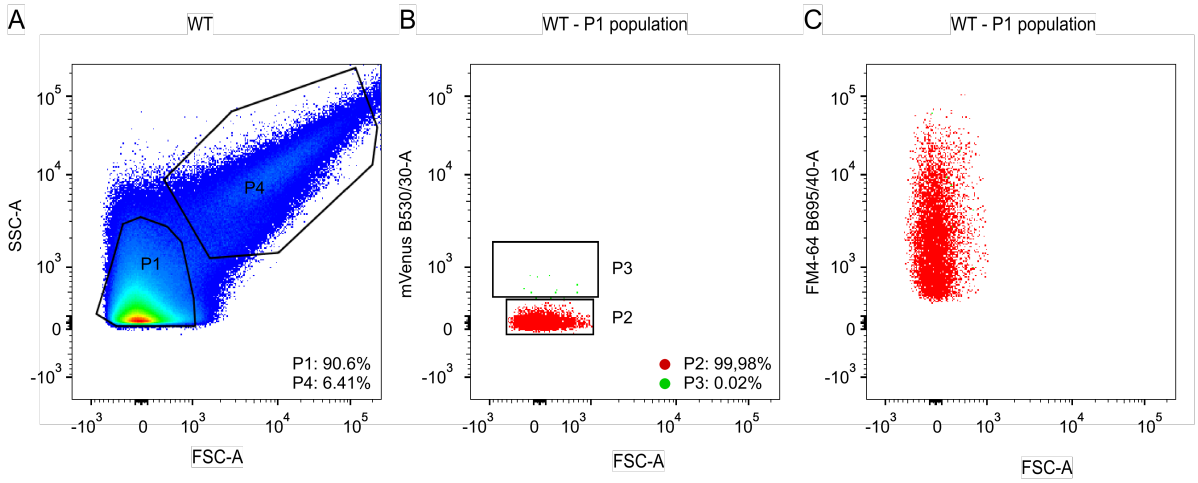

Figure 5.39: Wild-type synaptosomes determine the autofluorescence of synaptosomes.
(A) Synaptosomes were prepared from wild-type mice and analyzed using the forward scatter (FSC) and side scatter (SSC). Gate P1 represents single synaptosomes while P4 contains aggregated synaptosomes. Red indicates highest and blue lowest abundance of particles. **(B)** Gate P1 was separated into P2 and P3 using the mVenus fluorescence. **(C)** All synaptosomes labeled with F4-64 dye.

The same settings were used for NG2-Cre:PSD95mVENUS synaptosomes (Figure 5.40.A). In contrast to wild-type synaptosomes, mVENUS-positive synaptosomes were detected that represented 0.66 % of the whole P1 synaptosome population (Figure 5.40.B).

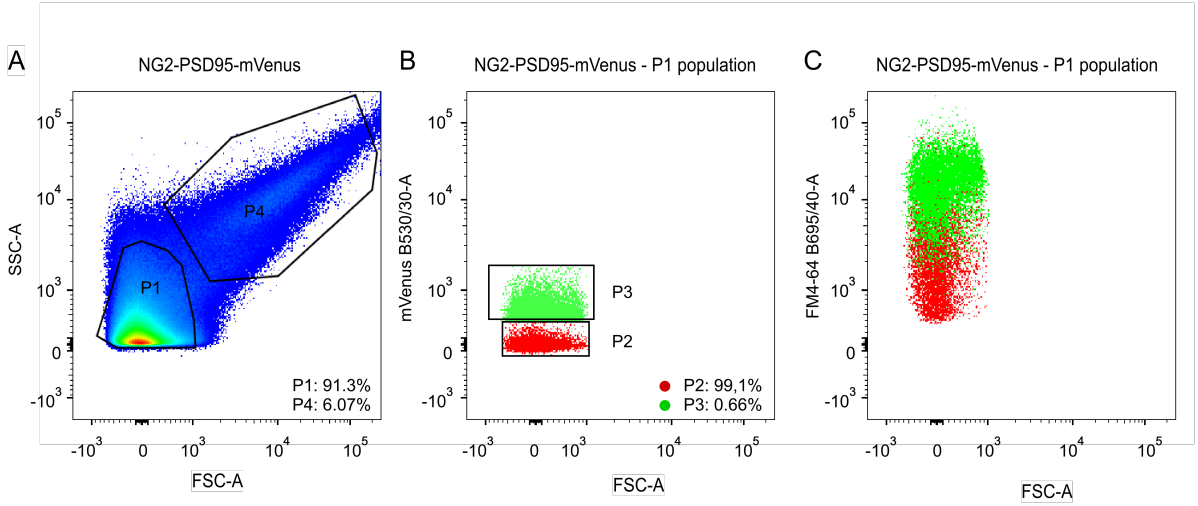

Figure 5.40: Detection of a small fraction of NG2-Cre:PSD95-mVenus synaptosomes.
(A) Synaptosomes were prepared from NG2-Cre:PSD95-mVenus mice and analyzed using the forward scatter (FSC) and side scatter (SSC). Gate P1 represents single synaptosomes while P4 contains aggregated synaptosomes. **(B)** Gate P1 was separated into P2 and P3 using the mVenus fluorescence. **(C)** All synaptosomes labeled with F4-64 dye.

A fraction of the sorted synaptosomes was used for reanalysis (Figure 5.41.A). The reanalysis is important to estimate the enrichment of the target synapses. The sorted synaptosomes were run through the sorter for 1 min to analyze the enrichment of

NG2-Cre:PSD95-mVenus synaptosomes. In our sample we were able to enrich the NG2-Cre:PSD95-mVENUS synaptosomes to 34.4% (P3, Figure 5.41B).

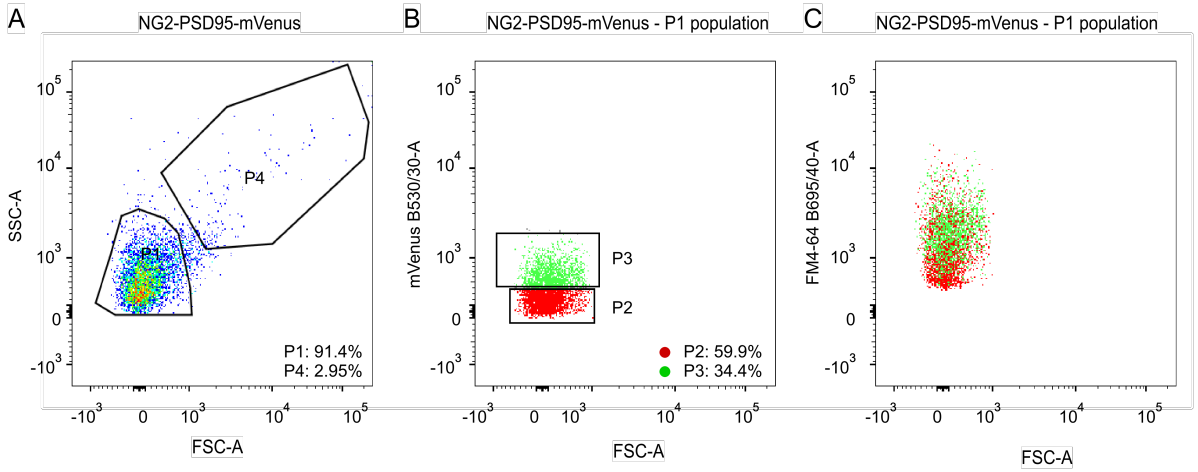

Figure 5.41: Reanalysis of sorted NG2-Cre:PSD95-mVenus synaptosomes

(A) Sorted NG2-Cre:PSD95-mVenus synaptosomes were reanalyzed using the forward scatter (FSC) and side scatter (SSC). Gate P1 represents single synaptosomes while P4 contains aggregated synaptosomes. **(B)** Gate P1 was separated into P2 and P3 using the mVenus fluorescence. **(C)** All synaptosomes labeled with F4-64 dye.

5.2.2 Generation of BioID mice lines

5.2.2.1 Biotinylation in CA3 pyramidal cells and dentate gyrus granule cells in the hippocampus

The molecular basis of the signaling pathways in specific synapses is still under investigation. Proximity-labeling approaches were used to identify for example inhibitory postsynaptic proteins (Uezu *et al.*, 2016). In this study, they made use of the biotinligase BirA that biotinylates proteins within a distance of 10 to 50 nm. The fusion of BirA to gephyrin enabled the isolation and identification of the inhibitory postsynaptic proteome.

To delineate the proteome of Mossy fiber and Schaffer collateral synapses, we decided to use mouse lines with protein biotinylation in the synapses of interest. Therefore, we crossed either Prox1-Cre (expressing Cre in dentate gyrus granule cells) or Et-iCre (expressing Cre in CA3 pyramidal cells) with BioID mice, which

express a myc-tagged biotin ligase (BirA) in a Cre-dependent manner. The biotinylation of proteins was facilitated by biotin application for several consecutive days. We decided to administer the biotin via food because the solubility of biotin is very low (0.22 mg/ml in H_2O) while the food contained 800 mg/kg. The animals were fed with the biotin food for 14 consecutive days before being sacrificed to evaluate the biotinylation levels by immunohistochemical stainings. The BirA expression was confirmed via myc staining while the biotinylation was visualized using streptavidin (Figure 5.42). Wild-type animals did not show any biotinylation or myc staining in the hippocampus after the biotin administration. A moderate streptavidin signal in the CA3 region was detected in the Et-iCre:BioID mice which colocalized with the detected myc staining. Somata of the pyramidal cells in CA3 were clearly visible. However, the Schaffer collateral synapses projecting to the CA1 were not detected. In contrast, in the Prox1-Cre:BioID mice the signal for both stainings was strong in the somata of the granule cells as well as in the Mossy fiber synapses.

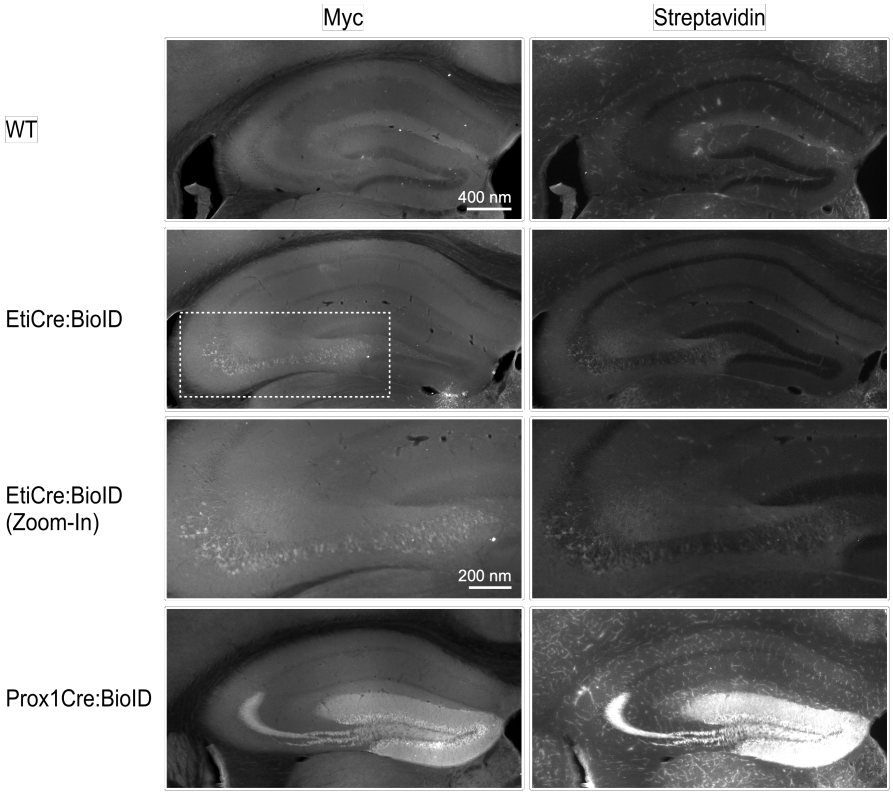

Figure 5.42: Successful BirA expression in BioID mouse lines.

Myc-tagged BirA was expressed in dentate gyrus granule cells (Prox1Cre:BioID) or CA3 pyramidal cells (Et-iCre:BioID). Myc staining was used to highlight BirA expression and streptavidin to visualize biotinylation. WT: N = 2, Et-iCre:BioID: N = 4, Prox1Cre:BioID: N = 3.

5.2.2.2 Successful biotinylation in synaptosomes

The analysis of the synaptic proteome of the mentioned hippocampal synapses requires a successful biotinylation of proteins in the synapses. To investigate the biotinylation of proteins in the synapse, synaptosomes (P2) were prepared from hippocampus homogenate (HH) of the respective BioID mice after 14 days of biotin food application. Synaptosomes and hippocampus homogenates were lysed and denatured to verify the BirA expression and biotinylation using immunoblot analysis (Figure 5.43). BirA-myc expression was not detected in both wild-type samples. However, streptavidin revealed two distinct bands at 130 kDa and approximately 80 kDa, which most likely represent endogenously biotinylated carboxylases (Niers *et al.*, 2011). A strong increase in biotinylation was detected for both BioID mouse lines. Moreover, the expression of BirA-myc was confirmed using the myc-antibody.

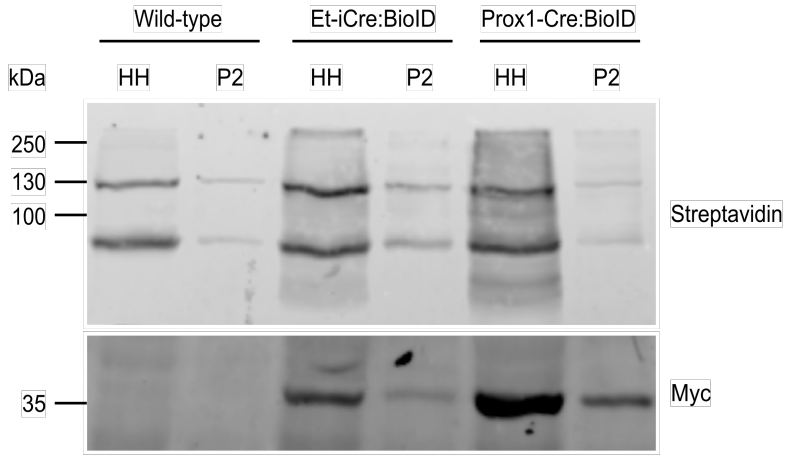

Figure 5.43: Successful BirA expression and biotinylation in the synapses in BioID mouse lines.

Hippocampi of indicated mouse lines were isolated and homogenized (HH). HH was used to prepare synaptosomes (P2). Samples were lysed and denatured to analyze proteins using immunoblots. Streptavidin was used to visualize biotinylated proteins and myc-antibody to verify BirA-myc expression. N = 3.

5.2.2.3 Optimization of synaptosome fractionation for mossy fiber synapses

Synaptosome preparations have been established in the past and are suited for most of the diverse synapses present in the brain. However, MF synapses of granule cells are special synapses as they are distinct from other synapses in various points. MF are larger than other synapses with a volume of 2 – 13 µm^3 (mean 8.24, rat,

(Rollenhagen and Lübke, 2010)) compared to Schaffer collateral synapses, which range from 0.02 to 1.73 μm^3 (mean 0.36, rat, (Rollenhagen *et al.*, 2018)). One bouton contains on average 20 AZ and 16,000 synaptic vesicles (Rollenhagen and Lübke, 2010), whereas Schaffer collateral synapses of pyramidal neurons exhibit only 1-2 release sites and on average 800 synaptic vesicles (Rollenhagen *et al.*, 2018). In the past, other synaptosome fractionations were used to isolate MF synapses (Lonart and Südhof, 1998). The MF fractionation protocol includes an additional centrifugation step at high speed that might lead to a higher efficiency to spin down the bigger MF synapses. Here, we compared two synaptosome fractionations to evaluate, which preparation would be better suited to isolate MF synapses (Figure 5.44.A). We used nectin-3 and synaptoporin (also called Synaptophysin 2) as MF markers (Mizoguchi *et al.*, 2002; Lee *et al.*, 2013). Nectin-3 protein levels were normalized to β-actin to compare both fractionations. Interestingly, the MF synaptosome fractionation did not display a higher nectin-3 amount verifying that our established synaptosome fractionation is suitable to isolate MF synapses (Figure 5.44.B and 5.44 C).

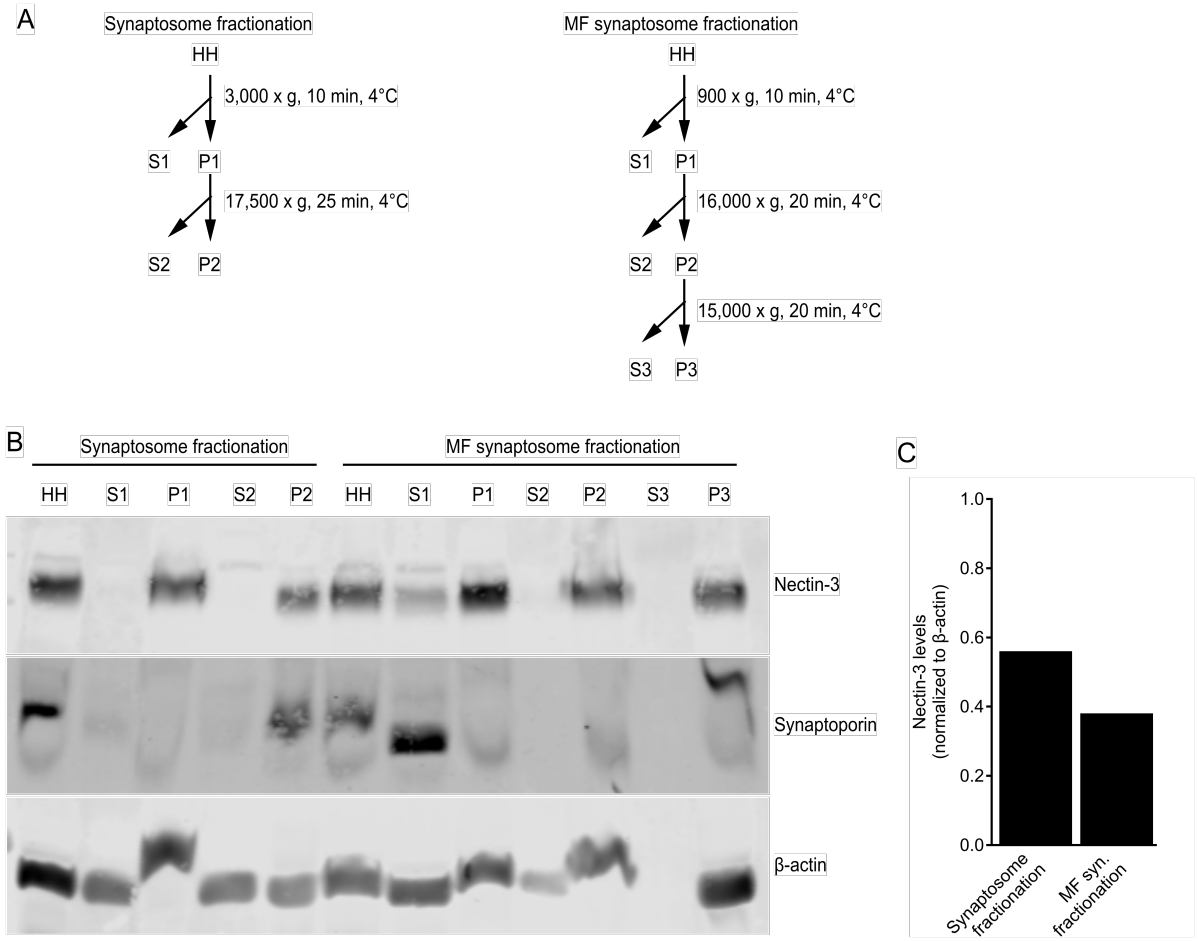

Figure 5.44: Successful synaptosome fractionation of MF synapses.

(A) Schematic overview of the two compared protocols. **(B)** Indicated fractions of both synaptosome fractionations were analyzed using immunoblots. **(C)** Quantification of nectin-3 protein levels. N = 2.

5.2.2.4 First results of a synapse-specific proteome

For our proteomic analysis of the granule cells and CA3 pyramidal cells, we decided to use microdissections of the dentate gyrus (DG) and CA3 region (Prox1Cre:BioID) or CA3 and CA1 region (EtiCre:BioID). This procedure gives the advantage to produce two samples per mouse line: The soma (DG for Prox1Cre:BioID and CA3 for EtiCre:BioID) and the synapse fraction (CA3 for Prox1Cre:BioID and CA1 for EtiCre:BioID). The amount of required protein was established by pooling several mice to analyze the proteome of the regions of interest (data not shown) and we decided to run a first test run with all samples. Therefore, we pooled the indicated microdissected region of the hippocampi of six mice and performed an

immunoprecipitation using streptavidin beads followed by the trypsinization. The samples were measured by Mariella Hurtado Silva (laboratory of Mark Graham, Sydney, Australia). More proteins were detected in the synapse sample (CA3: 4482 proteins, Figure 5.45.A) compared to the soma sample (DG: 2725 proteins) in the granule cells (Prox1Cre:BioID line). For the CA3 pyramidal cells (EtiCre:BioID) we detected more proteins in the soma (CA3: 3225 proteins) than in the synapse sample (CA1: 1813 proteins). To analyze the detected proteins, we used the SynGO classification (Koopmans *et al.*, 2019) (Figure 5.45.B). For the granule cells, the soma sample covered 55.80% of synaptic proteins and the synapse sample 69.84%. A comparable percentage for the soma sample was detected for the CA3 pyramidal cells (60.42%), while the synapse sample covered 43.39% of the synaptic proteins.

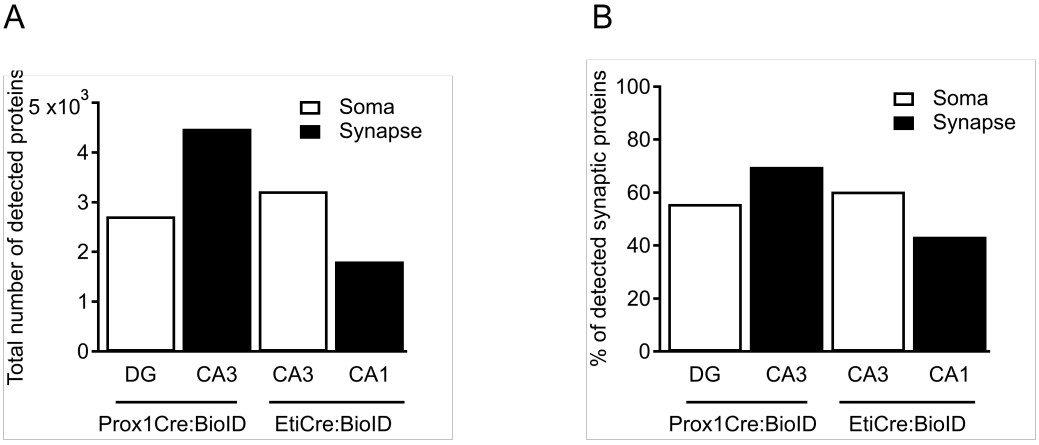

Figure 5.45: Overview about detected proteins after biotinylation in specific synapses. **(A)** Indicated region of the hippocampus was microdissected and subsequently lysed to perform an immunoprecipitation to isolate biotinylated proteins. Proteins were analyzed using mass spectrometry. **(B)** The detected proteins (A) were analyzed using SynGO classification (Koopmans *et al.*, 2019) to analyze the percentage of synaptic proteins of the total number of detected proteins. N = 1.

Next, we performed a functional categorization of the synaptic proteins using the SynGO classification (Koopmans *et al.*, 2019) (Figure 5.46). A strong enrichment in the presynapse was detected in the active zone (AZ), synaptic vesicles (SV) and the presynaptic membrane (PrSM) for all four samples. In the postsynapse, the highest enrichment for all samples was detected in the postsynaptic specialization (PSS). However, a similar enrichment in the postsynaptic membrane (PSM) compared to the presynaptic membrane was detected in all four samples. Moreover, the cytoskeleton

proteins were enriched in the postsynapse. Interestingly, no enrichment was detected in the synaptic cleft for all samples.

This data indicates that our experimental procedure and sample preparation is successful to analyze to synaptic proteins of the soma and synapse of specific synapse types.

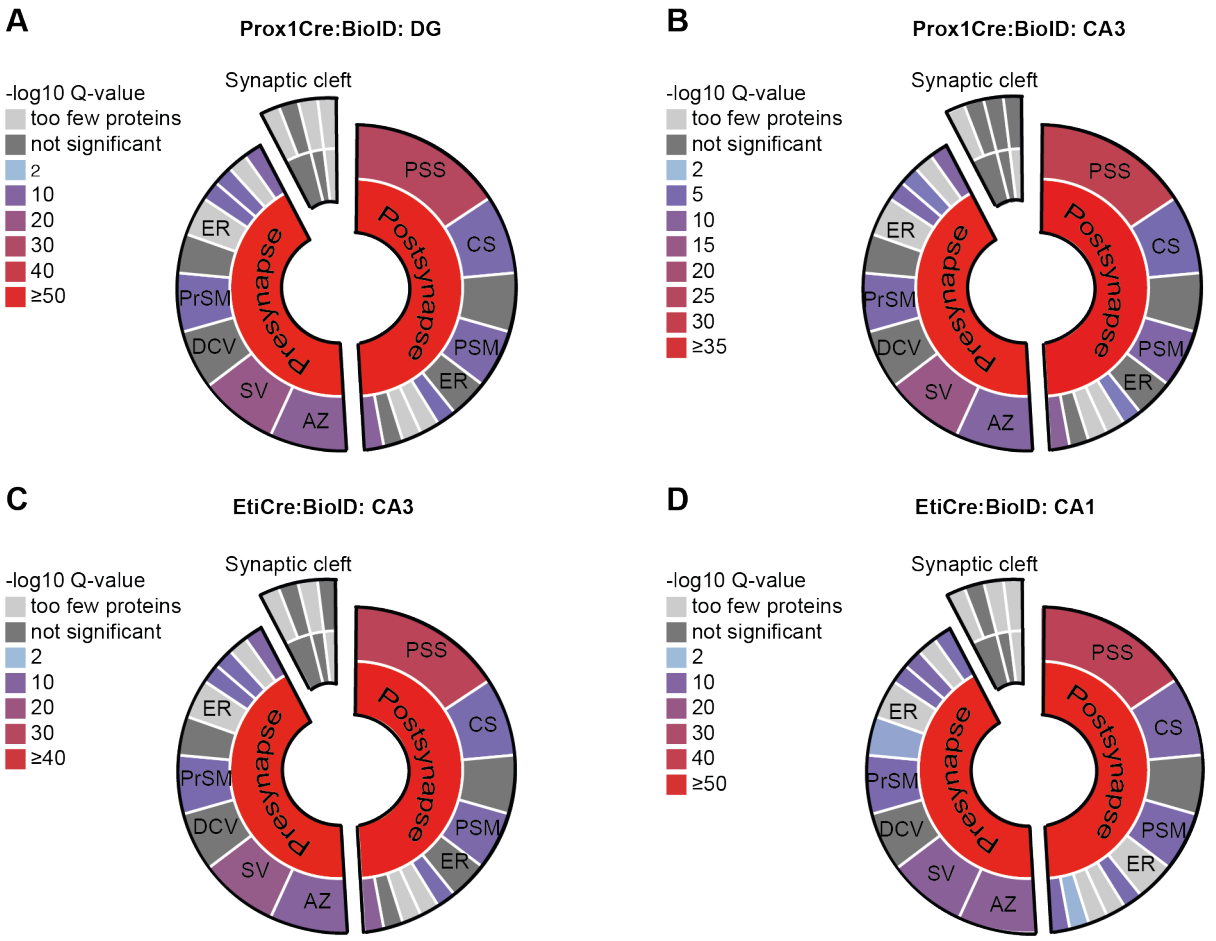

Figure 5.46: Functional categorization of synaptic proteins.

(A-D) Synaptic proteins were categorized using SynGO classification (Koopmans *et al.*, 2019). **(A)** Soma of dentate gyrus granule cells. **(B)** Synapse fraction of dentate gyrus granule cells. **(C)** Soma of CA3 pyramidal cells. **(D)** Synapse fraction of CA3 pyramidal cells. AZ: Active zone, SV: Synaptic vesicle, DCV: Dense core vesicle, PrSM: Presynaptic membrane, ER: Endoplasmic reticulum, PSS: Postsynaptic specialization, CS: Cytoskeleton, PSM: Postsynaptic membrane. N = 1.

6. Discussion

6.1 SRPK2: a new player in presynaptic plasticity

The communication in neuronal networks is conducted by the release of neurotransmitter (NT) at the presynapse. The proteins at the presynapse involved in priming, docking and fusion of NT-filled synaptic vesicles have been intensively studied in the last 30 years and the key proteins that orchestrate these processes were identified. Recently, the importance of posttranslational modifications in the regulation of this dynamic process have emerged. Several studies have highlighted the impact of protein phosphorylation during neuronal activity and synaptic plasticity (Kohansal-Nodehi *et al.*, 2016; Engholm-Keller *et al.*, 2019).

In this study, we have uncovered a novel role for the kinase SRPK2 in organization of active zone ultrastructure and synaptic plasticity in mammalian CNS synapses. Using mass spectrometry, we describe for the first time the neuronal phosphoproteome of this kinase and identified RIM1 as a direct target of SRPK2. Biochemical assays demonstrated the interaction of SRPK2 with different active zone proteins. Our data indicated SRPK2 as a regulator for synaptic release and presynaptic plasticity by controlling the abundance and nanoclusters of RIM1.

6.1.1 Identification of the SRPK2 phosphoproteome

We used primary cultured neurons and modified SRPK2 expression levels to determine the neuronal phosphoproteome of SRPK2. The SRPK2 regulated phosphoproteome in neurons comprises 1046 proteins with regulated phosphorylation sites (Figure 5.4.B). Among the 796 proteins that exhibited an increased phosphorylation of at least one phosphorylation site, we were able to confirm tau as a target of SRPK2 as described previously (Hong *et al.*, 2012). Our screen demonstrated that SRPK2 regulates proteins that are involved in multiple biological processes such as mRNA splicing as expected from the literature. The role of SRPK2 with respect to mRNA splicing is well characterized (Giannakouros *et al.*, 2011). The importance of phosphorylation of the SR proteins in this process was

shown by the expression of phosphatase PP1, which inhibited the spliceosome assembly (Mermoud *et al.*, 1994).

In addition, the involvement of SRPK2 with unexpected, synaptic processes like synaptic plasticity or synaptic vesicle priming was identified (Figure 5.5). Many synaptic proteins (94 (SRPK2) or 34 (shSRPK2) out of 482 proteins in the presynapse; 117 (SRPK2) or 34 (shSRPK2) out of 592 in the postsynapse) exhibited a regulation of their phosphorylation status by SRPK2 (Figure 5.7). Among these synaptic proteins several AZ members were targets of SRPK2: RIM1, RIM2, ELKS1, ELKS2, bassoon, piccolo, liprin-α3, RIM-BP2 and Munc13. So far, only ELKS1 and ELKS2 had been identified as a target of SRPK2 (Driller *et al.*, 2019). Whether other proteins besides ELKS1/2 and RIM1 are direct targets of SRPK2, has to be determined in future experiments. Apart from AZ proteins, many kinases and phosphatases are phosphorylated by SRPK2 (Figure 5.6). The phosphorylation of kinases can enhance or reduce the activity and thereby lead to indirect effects of SRPK2 on the phosphorylation of AZ proteins. Pak1 for example exhibited an increase in the phosphorylation status for serine 174 that is linked to an enhancement of its activity (Kong *et al.*, 2009).

Recently, Bruchpilot was identified as a direct target of SRPK79D in *Drosophila melanogaster* (Driller *et al.*, 2019). In line with this, the phosphorylation status of ELKS1 and ELKS2 was changed by SRPK2 (Figure 5.10). However, we detected an upregulation for serine 415 in ELKS1, which is an amino acid not conserved in *Drosophila melanogaster*. Similarly, we identified a single upregulated phosphorylation site for ELKS2 (S33) after SRPK2 overexpression. Serine 33 of ELKS2 is not conserved in *Drosophila melanogaster*. Interestingly, the adjacent serine (S34) is conserved in *Drosophila melanogaster* (S71) and phosphorylated in Bruchpilot by SRPK79D (Driller *et al.*, 2019). ELKS1 (Cast2) was previously identified as a target of SRPK2 (Driller *et al.*, 2019). ELKS1 fragments containing the N-terminal regions (up to amino acid 353) were used in this study but the exact phosphorylation site was not identified. However, we were not able to detect a SRPK2 regulated phosphorylation site within this region except for serine 415. SRPK2 regulates many phosphatases (Figure 5.6.B), which might lead to the dephosphorylation of a direct SRPK2 site that was detected by Driller and colleagues using *in vitro* phosphorylation.

6.1.2 Evaluation of a new SRPK2 motif

Bioinformatic approaches were used in this study to create a motif of SRPK2 as there is none available to date due to the absence of a big phosphoproteomic screen (Appendix 9.1). Surprisingly, the consensus motif determined from our *in vitro* phosphorylation assay exhibited several differences to the other SRPK2 motif that was generated by published SRPK2 targets and the SRPK1 motif. In contrast to the curated motif (generated using published SRPK2 targets), not only serines were phosphorylated by SRPK2 in our experiment but also threonines. However, the content of threonine was much lower compared to serines indicated by the relative size of the threonine (T) at the P0 position. Our generated SRPK2 motif also contained many arginines (R) and serines (S) at the positions P-7 to P7. Nevertheless, the content of both, arginine and serine, was reduced compared to the SRPK1 and SRPK2 curated motif. Instead, the variation for all positions around the serine or threonine was much higher in our newly generated SRPK2 motif. This highlights the differences between SRPK1 and SRPK2, which can be distinguished by their expression but also by preferences for their targets.

Different SRPK2 targets have already been identified before, such as the serine/arginine-rich splicing factor SC35 (Jang *et al.*, 2009) or acinus (Jang *et al.*, 2008). Acinus is phosphorylated at serine 422, which is part of the serine-arginine (SR) repeats in the protein. The SRPK2 motif generated by its published targets points to a preference of serine-arginine-rich proteins as the most preferred targets.

To characterize the consensus motif of SRPK2, a biased peptide library was *in vitro* phosphorylated by SRPK2 (Wang *et al.*, 1998). Due to the positioning of serine at the P0 position the library was biased to identify only a motif for serine but not threonine or tyrosine phosphorylation. Additionally, arginine was positioned at P-3. This study suggested the three following hallmarks for the SRPK2 motif: First, serine-arginine dipeptides are phosphorylated. Second, a basic environment represented by arginine or histidine is preferred. Third, lysine as the third basic amino acid disturbs the phosphorylation, especially at the position P-2. However, the proposed criteria were not confirmed by the motif identified in tau (Hong *et al.*, 2012). Hong and colleagues revealed that the microtubule associated protein tau is phosphorylated at serine 214, which exhibits the motif -TPS(214)LP-. Even though two SR dipeptides are N-terminal of the threonine, this points to a more flexible motif of SRPK2 compared to SRPK1. Moreover, in our experiment the peptides were disadvantageous because

most likely SRPK2 was not able to bind the peptides. This problem could be circumvented by the phosphorylation of longer fragments.
Our generated motif will most likely also not be valid for all SRPK2 targets. It has to be taken into consideration that we generated a motif based on one SRPK2 target: RIM1. Therefore, the motif might show slight variation when another SRPK2 target would be used. It would be beneficial to identify several direct targets of SRPK2 with multiple phosphorylation sites to build a motif for SRPK2.
A different aspect to keep in mind during the definition of kinase motifs is the possibility of non-linear motifs, which are based on the structure in proximity of the phosphorylation site (de Oliveira *et al.*, 2016). A non-linear motif was suggested for PKA and PKC (Grifman *et al.*, 1997; Duarte *et al.*, 2014). Therefore, structurally formed consensus motifs for SRPK2 are possible but have not been addressed in this study. Our generated motif points to a higher flexibility of SRPK2 with respect to the phosphorylation site in contrast to SRPK1, which motif consists only of serine-arginine repeats (Appendix 9.1). A non-linear motif of SRPK2 could explain the higher variability around the phosphorylation site for SRPK2 because a structure close to the phosphorylation site determines the binding and phosphorylation of the target by SRPK2.

6.1.3 SRPK2 regulates overall AZ protein abundance and synaptic RIM1 levels

Here, we show that SRPK2 regulates the overall abundance of the AZ proteins RIM1 and ELKS1/2 (Figure 5.17) but only RIM1 protein levels were significantly increased at the synapse (Figure 5.21 and 5.22). Moreover, we detected that SRPK2 promotes RIM1 degradation (Figure 5.25). Therefore, SRPK2 seems to regulate both the translation as well as the degradation of RIM1. It has been postulated that phosphorylation of RIM1 increases its stability. In our data, we detected 21 sites in RIM1 directly phosphorylated by SRPK2 and 13 indirectly phosphorylated sites (Figure 5.13). Thus, SRPK2 could impact the stability of RIM1 by direct or indirect phosphorylation. Due to the regulatory role of SRPK2 for many kinases and phosphatases (Figure 5.6), SRPK2 potentially activates different signaling cascades in which proteins could then directly regulate the stability of RIM1. The SRPK2 regulated phosphorylation sites in RIM1 are distributed in clusters in unstructured

regions of RIM1 and could potentially regulate the structure of RIM1 and thereby interaction with other proteins. Strikingly, no phosphorylation site was detected in a structural domain of RIM1 (Zn^{2+}, PDZ, C2A or C2B). Nonetheless, the phosphorylation sites could impact the stability or binding to other proteins leading to a tighter integration and higher stability of RIM1 at the AZ. A protective effect of phosphorylation from proteasome-dependent degradation has been shown for the cyclin-dependent kinase like 5 (CDKL5) (La Montanara *et al.*, 2015). In contrast, phosphorylation can also induce protein degradation as demonstrated for BAG3 phosphorylation by CDK5 in mammalian synapses (Zhou *et al.*, 2019) and PAR-1 phosphorylation in *Drosophila melanogaster* (Mammalian homologues: Microtubule affinity-regulating kinases (MARK) 1-4) (Lee *et al.*, 2012). Therefore, it has to be determined in future experiments which phosphorylation sites in RIM1 by SRPK2 might mediate a protective effect and/or initiate the protein degradation.

The estimated half-life of RIM1 is approximately three days (Cohen and Ziv, 2017), which explains that we did not detect a change of RIM1 protein levels in control neurons after 6 h of emetine treatment. However, SRPK2 enhanced the protein turnover of RIM1 (Figure 5.25). RIM1 is a known target of the E3 ubiquitin ligase SCRAPPER (Yao *et al.*, 2007). In our phospho-proteomic screen, SCRAPPER was not phosphorylated by SRPK2, which could initiate the RIM1 ubiquitination. Alternatively, RIM1 protein levels are also regulated by a SCRAPPER-independent mechanism (Yao *et al.*, 2007) which might be triggered by SRPK2.

Another possibility to control protein abundance is that SRPK2 could affect the transcription and/or translation of proteins. SRPK2 has been identified to regulate transcription (Jang *et al.*, 2008) as well as translation (Windgassen *et al.*, 2004; Michlewski, Sanford and Caceres, 2008). However, the transcription of RIM1 was not altered by SRPK2 (Figure 5.24). The increase of overall RIM1 levels (Figure 5.17) mediated by SRPK2 might be the result of an enhanced translation of RIM1 that counteract the induced RIM1 degradation by SRPK2 (Figure 5.25).

6.1.4 Differences in the function of SRPK2 and SRPK79D

In *Drosophila melanogaster* the regulatory role of SRPK79D was detected for Bruchpilot but not for other AZ proteins. The axonal accumulation of Bruchpilot in the axons of the SRPK79D loss-of-function mutants led to the depletion of Bruchpilot

from the synapses (Johnson *et al.,* 2009). This is in contrast to our data since we did not detect a change of synaptic ELKS1/2 levels (Figure 5.22). SRPK79D phosphorylates Bruchpilot at several sites (Driller *et al.*, 2019). In total 15 phosphorylation sites were detected *in vivo* and *in* vitro. The phosphorylation status of proteins can increase the stability and therefore lead to a higher abundance for example at the active zone. However, these phosphorylation sites in Bruchpilot are not regulated in ELKS1/2 by SRPK2 in cultured mouse cortical neurons (Figure 5.10). Moreover, we detected only one regulated phosphorylation site for ELKS1 and two for ELKS2. Bruchpilot and ELKS1/2 share a similarity in their N-terminus but not in their C-terminus (Held and Kaeser, 2018). Thus, a non-linear motif could explain that homologous serines of Bruchpilot and ELKS1/2 are not phosphorylated. Moreover, SRPK79D and SRPK2 share only 54% sequence homology (Nieratschker *et al.*, 2009). Important to note is that already small differences in protein amino acid sequences can have a major impact on the respective protein function. A prominent example is protein kinase C (PKC), which exists in many different isoforms that function in part independent of each other (Sossin, 2007).
Thus, other phosphorylation sites that are important for protein stabilization and are phosphorylated by SRPK79D in Bruchpilot are not regulated in ELKS1/2 by SRPK2.

6.1.5 SRPK2 acts upstream of RIM1

Our data demonstrated that SRPK2 regulates the clustering of RIM1 in both presynapse and axon and that the number of RIM1 nanoclusters at the presynapse scales with SRPK2 expression (Figures 5.31 and 5.32). RIM1 nanoclusters are part of trans-synaptic molecular nanocolumns that resemble release sites (Tang *et al.*, 2016), indicating that SRPK2 regulates release via RIM1 nanoclusters. This hypothesis was supported by the following findings: FM4-64 dye assays demonstrated that the synaptic release probability positively scales with SRPK2 levels (PhD thesis Johannes Alexander Müller, 2019). This observation was confirmed using the genetically encoded glutamate sensor pAAV-hSyn-SF-iGluSnFR.V184A (PhD thesis Johannes Alexander Müller, 2019). Additionally, the importance of the kinase activity of SRPK2 was highlighted (PhD thesis Johannes Alexander Müller, 2019). The increase in neurotransmitter release was absent when a kinase-dead version of SRPK2 was overexpressed instead of the wild-type SRPK2

variant. To prove that SRPK2 acts upstream of RIM1, SRPK2 was overexpressed in conditional RIM1/2 double knock-out (cDKO) neurons. SRPK2 overexpression could not rescue the reduction in neurotransmitter release indicating that the presence of RIM1 is required for SRPK2 to regulate neurotransmitter release (PhD thesis Johannes Alexander Müller, 2019). Removal of both large RIM isoforms has been shown to reduce neurotransmitter release (Han *et al.*, 2011; Kaeser *et al.*, 2011) and was confirmed in our laboratory. This data demonstrates that SRPK2 tunes presynaptic strength in a RIM-dependent manner.

Moreover, we investigated the effect of SRPK2 on the number of docked synaptic vesicles that correlates with the synaptic release probability and therefore synaptic strength. Interestingly, the number of docked vesicles scales with SRPK2 expression levels (PhD thesis Isabelle Paulußen, unpublished, data not shown). The large isoforms of RIM proteins (RIM1 and RIM2) are important to cluster and localize Ca^{2+} channels to the AZ as well as for the docking of synaptic vesicles (Han *et al.*, 2011; Kaeser *et al.*, 2011). Thus, the higher number of RIM1 nanoclusters due to elevated SRPK2 levels enables the increased number of docked vesicles in the presynaptic terminal. The increase of docked vesicles has been correlated to synaptic strength in previous studies (Murthy *et al.*, 2001; Weyhersmuller *et al.*, 2011). Moreover, an increase of synaptic RIM1 levels is associated with a higher network activity (Lazarevic *et al.*, 2011). Both characteristics of synaptic strength are induced by SRPK2 expression.

Altogether our data demonstrates that SRPK2 acts upstream of RIM1 and modulates presynaptic strength in a RIM-dependent manner by elevating RIM1 nanoclusters resulting in an increase of docked vesicles.

6.1.6 SRPK2 as a potential key player in liquid-liquid phase separation

We identified RIM1, RIM-BP2 but also the microtubule-associated protein tau as a protein whose phosphorylation status is regulated by SRPK2 (Figure 5.4). In total, 14 phosphorylation sites in tau were significantly regulated by SRPK2 (data not shown). The phosphorylation status was suggested to play an important role for the formation of subcellular compartments (Ambadipudi *et al.*, 2017; Milovanovic *et al.*, 2018). Superresolution microscopy enabled the investigation of the nanoscale organization of the AZ. The clustering of different presynaptic proteins as well as their presynaptic

localization were demonstrated (Dani *et al.*, 2010; Tang *et al.*, 2016). Both AZ scaffold proteins RIM1 and RIM-BP are essential for correct Ca^{2+} clustering at the presynapse (Kaeser *et al.*, 2011, 2012; Liu *et al.*, 2011). A recent study suggested that the interaction of RIM and RIM-BP initiates a liquid-liquid phase separation (LLPS) and thereby the recruitment of Ca^{2+} channels (Wu *et al.*, 2019). The concept of phase separation to induce the formation of subcellular compartments was initially identified in *Caenorhabditis elegans* (Brangwynne *et al.*, 2009) but was also observed in neurons. The liquid phase separation in the postsynaptic density is induced by the interaction of SynGAP and PSD-95 (Zeng *et al.*, 2016). In the presynapse, synapsin generates a liquid phase to form synaptic vesicle clusters (Milovanovic *et al.*, 2018). Interestingly, the phase separation by synapsin is regulated by phosphorylation of synapsin by the calcium/calmodulin-dependent protein kinase II (CaMKII). Thus, phosphorylation might regulate LLPS and likely also nanoclusters of RIM1 or other proteins at the synapse. To induce synaptic vesicle fusion, it is mandatory that proteins of the cytomatrix at the AZ like RIM1, RIM-BP and ELKS interact with synaptic vesicles to induce their tethering and subsequent fusion. While CamKII might regulate the dispersion of the liquid phase of synaptic vesicles, phosphorylation of RIM1 by SRPK2 could initiate a similar process for the liquid phase of RIM1 and RIM-BP.

The liquid-liquid phase separation was not only demonstrated for AZ proteins but also for the microtubule-associated protein tau (Ambadipudi *et al.*, 2017; Wegmann *et al.*, 2018). Tau is a soluble protein and does not tend to aggregate *in vitro* (Cleveland *et al.*, 1977; Wille *et al.*, 1992). Hyperphosphorylated tau, as observed in Alzheimer's Disease patients however, induces tangle formation (Hanger *et al.*, 2007). MARK2 was identified as a kinase inducing tau liquid-liquid phase separation by phosphorylating tau at three different serines: S262, S324 and S356 (tau isoform 2N4R) (Ambadipudi *et al.*, 2017). Interestingly, serine S324 was also significantly upregulated when SRPK2 was overexpressed in neurons (S616, Tau (mouse) UniProt ID: P10637).

While phosphorylation of tau induces LLPS, the opposite was observed for synaptic vesicle clusters in which phosphorylation of synapsin by CamKII dispersed the LLPS (Milovanovic *et al.*, 2018). SRPK2 is a prime candidate to coordinate the LLPS as it regulates the phosphorylation status of multiple AZ proteins. Whether the phosphorylation of RIM, RIM-BP or other AZ proteins by SRPK2 controls the LLPS

needs to be answered in future studies as well as the question if this induces or disperses the subcellular compartmentalization.

6.1.7 SRPK2 and RIM1 are required for presynaptic homeostatic plasticity

Our data highlighted the translocation of SRPK2 and RIM1 to the presynapse during presynaptic homeostatic plasticity (Figures 5.37 and 5.38). Elevated levels of SRPK2 resulted in an increase of synaptic vesicle release as described above (chapter 6.1.5) (PhD thesis Johannes Alexander Müller, 2019). Therefore, the high levels of SRPK2 during presynaptic homeostatic plasticity at the synapse should also result in an increase of presynaptic release. This was confirmed using the iGluSnFR assay (PhD thesis Annika Mayer, data not shown, unpublished). Induction of presynaptic homeostatic plasticity resulted in an increase of synaptic release in wild-type neurons, which most likely is mediated by the increase of SRPK2 levels in the synapse. The increase in synaptic output was dependent on RIM1/2 as the release was not potentiated in RIM1/2 cDKO neurons. Similarly, no homeostatic plasticity was observed in conditions with knocked-down or overexpressed SRPK2 levels. This suggests that the release can not be further potentiated by SRPK2 during presynaptic homeostatic plasticity if it is already increased in basal conditions due to SRPK2 overexpression. SRPK2 levels dictate the number of synaptic RIM1 clusters that most likely induce the increase in release. Interestingly, a similar number of synaptic RIM1 clusters was observed during homeostatic plasticity compared to SRPK2 overexpression (HP: 3.45 ± 0.39, SRPK2 OE: 4.32 ± 0.92). Thus, it is possible that SRPK2 overexpression already saturates all potential RIM1 spots with RIM1 molecules. During homeostatic plasticity, increased SRPK2 levels in the overexpressed condition are not able to translocate more RIM1 molecules to the synapse, since all potential spots in the presynaptic bouton are already occupied.
A likewise role was observed in *Drosophila melanogaster* for SRPK79D. It is known that presynaptic homeostatic plasticity similarly potentiates neurotransmitter release (Müller *et al.*, 2012). Recently, it was demonstrated that SRPK79D is necessary to mediate the increase in neurotransmitter release and for AZ remodeling during homeostatic plasticity (Böhme *et al.*, 2019). In accordance with our data of

homeostatic plasticity in RIM1/2 cDKO neurons, RIM is crucial to mediate presynaptic homeostatic plasticity in *Drosophila melanogaster* (Müller *et al.*, 2012). However, it is unknown so far whether SRPK79D regulates RIM levels as well as whether RIM levels increase during presynaptic homeostatic plasticity in *Drosophila melanogaster* as we showed here for mammalian neuronal cultures.

RIM, bassoon, piccolo and other AZ proteins are transported to the AZ by piccolo-bassoon transport vesicles (PTVs) (Shapira *et al.*, 2003). The anterograde transport of PTVs along microtubules is mediated by kinesin motors (Cai and Sheng, 2009). One subtype of the heavy chain of kinesin-1 is KIF5A (Kanai *et al.*, 2000). KIF5a protein expression is upregulated in homeostatic scaled-up neurons (Schanzenbächer *et al.*, 2016), which might be necessary for the transport of additional molecules of AZ members to the presynaptic bouton to induce homeostatic plasticity. Interestingly, SRPK2 phosphorylates several members of the KIF family and one phosphorylation site in KIF5a was significantly upregulated during overexpression of SRPK2 (data not shown). Hence, it can be speculated that SRPK2 acts not only directly at the AZ by phosphorylation of AZ members but also increases the transport of AZ members to enable the generation of new release sites. A similar mechanism was suggested in *Drosophila melanogaster*, where SRPK79D regulates the transport of Bruchpilot to the neuromuscular junction (Böhme *et al.*, 2019).

It is still unclear, how SRPK2 levels are regulated during neuronal activity. SRPK family members are constitutively active and do not require posttranslational modifications for their activation (Ngo *et al.*, 2007). Nonetheless, SRPK2 contains phosphorylation sites that are induced by neuronal activity (Engholm-Keller *et al.*, 2019). Two kinases, Akt and Casein kinase 2 (CK2) have been identified to phosphorylate SRPK2 thereby enhancing SRPK2 function (Mylonis and Giannakouros, 2003; Zhuo *et al.*, 2018). These posttranslational modifications could potentially regulate SRPK2 localization as well as interaction with other proteins like RIM1/2 or ELKS1/2.

The translocation of SRPK2 clusters to the presynapse might result from elevated transcription or translation which has been documented for other kinases and phosphatases (Hermey *et al.*, 2013; Schanzenbächer *et al.*, 2016; Schanzenbächer *et al.*, 2018). Expression levels of SRPK2 protein, however, were not changed during presynaptic homeostatic plasticity induced by TTX or bicuculline (Schanzenbächer *et al.*, 2016). While SRPK1 expression is significantly downregulated, a moderate

upregulation of SRPK2 was detected, which was not significant (Schanzenbächer *et al.*, 2016). Therefore, the unchanged SRPK2 protein levels in our experiments support the current literature (Figure 5.35).

Another possibility to regulate the translocation of SRPK2 to the presynapse are local mechanisms. It has been shown that stress signals result in a translocation of SRPKs in non-neuronal cells (Zhong *et al.*, 2009). Moreover, inhibition of SRPKs is mediated by the interaction with molecular chaperones or scaffold attachment factors B1 and 2 (SAFB1/2) (Tsianou *et al.*, 2009; Zhong *et al.*, 2009). SRPK1 translocation was inhibited by the binding of two chaperons, Hsp40 and Aha1 (Zhong *et al.*, 2009). Interestingly, the binding of Aha1 to SRPK1 occurs within the spacer region between the two kinase domains. This spacer region is highly variable between SRPK1 and SRPK2. Therefore, it is likely that another, so far unknown chaperon interacts with SRPK2 to regulate its localization. Whether these interactions take also place in neurons still needs to be addressed. It is possible that regulatory proteins maintain SRPK2 in the axon and that SRPK2 is released from these chaperons during homeostatic plasticity to enable the increase of synaptic SRPK2 and RIM1 nanoclusters.

All this data points to a predominant role of SRPK2 in the regulation of synaptic strength via RIM1. We identified RIM1 as a direct target of SRPK2 and both RIM1 and SRPK2 are necessary to induce presynaptic homeostatic plasticity. Mechanistically, SRPK2 translocates to the synapse, phosphorylates RIM1 and thereby increases RIM1 nanoclusters as well as neurotransmitter release (Figure 6.1).

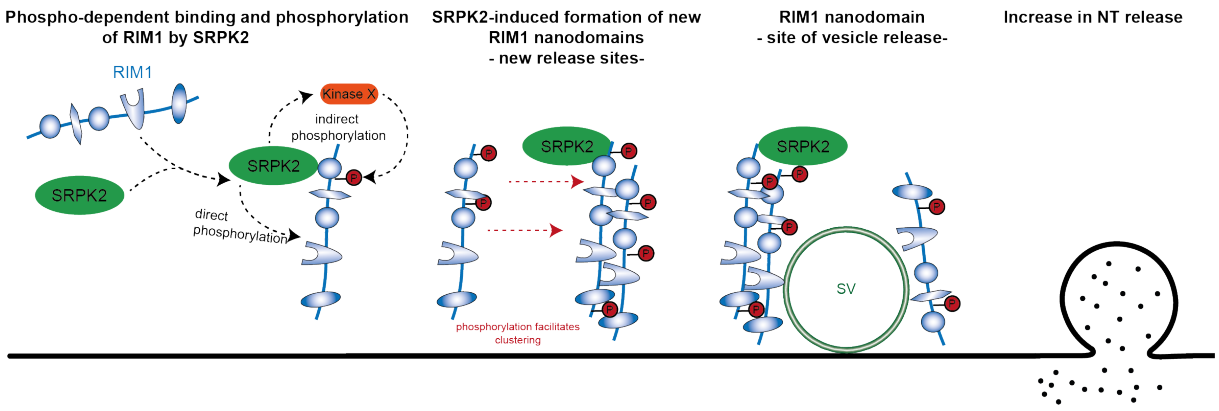

Figure 6.1: SRPK2 modulates synaptic strength by the formation of new RIM1 containing release sites.

SRPK2 binds RIM1 and regulates the phosphorylation status of RIM1 by direct and indirect phosphorylation. The phosphorylation induces the formation of new RIM1 nanodomains that resemble new release site resulting in an increase of NT release.

6.2 The identification of the presynaptic proteome of Mossy fiber and Schaffer collateral synapses

The synaptic proteome has been studied and proteins mediating synaptic transmission have been identified (Schrimpf *et al.*, 2005; Takamori *et al.*, 2006; Filiou *et al.*, 2010; Boyken *et al.*, 2013). However, several studies highlighted different physiological properties of various synapses. One example is presynaptic long-term plasticity (LTP) of MF synapses while Schaffer collateral synapses express a postsynaptic LTP (Weisskopf *et al.*, 1994; Tsien *et al.*, 1996). Surprisingly, LTP in MF was RIM1 dependent in contrast to Schaffer collateral LTP (Castillo *et al.*, 2002; Schoch *et al.*, 2002). These observations highlight the importance to identify the proteome of specific synapse types to understand the characteristics of the synapse of interest.

In this study, we established two different approaches to determine the proteome of MF and Schaffer collateral synapses. In the first approach, we used a fluorescent marker to sort our synapses of interest. For the second approach, mouse lines were generated to induce the biotinylation of proteins in the two synapses of interest. The synaptic proteome was determined using mass spectrometry.

6.2.1 Successful sorting of fluorescent NG2 synaptosomes

We established fluorescence activated synaptosome sorting (FASS), developed by Etienne Herzog and colleagues (Biesemann *et al.*, 2014), successfully in our laboratory. This technique enables researchers to isolate specific synapses and analyze the respective proteome. NG2 synaptosomes were enriched using a mVenus tag fused to PSD-95 in the postsynapse. We were able to enrich the NG2 synaptosome fraction starting from 0.66% of the initial population to 34.4% after the sorting. This means that we achieved a 50-fold enrichment of NG2 synapses with FASS sorting.

However, several drawbacks were discovered during the experiments. The sorting did not lead to the isolation of one specific synaptosome population but rather to an enrichment. An enrichment of 50 - 60% was achieved by this procedure still resulting in a mixture of various synapse types. Therefore, small differences in the protein composition between synapses might not be detected if two distinct subtypes are compared. Potentially, the fluorescently tagged PSD might have been a disadvantage in our experiments. Not all synaptosomes contain the PSD after the synaptosome preparation but only approximately 80% (Biesemann *et al.*, 2014). Therefore, our population was already reduced before the experiment started due to the partial loss of the PSD during the experimental procedure. Another disadvantage of the labeled PSD might be the size difference of the PSD compared to the presynapse. A tagged presynapse is most likely much brighter than the fluorescent postsynapse. Therefore, the signal can be detected better in the sorter resulting in a potential better signal-to-noise ratio. These experimental conditions are important to keep in mind if another mouse line would be generated to isolate synaptosomes using FASS.

Another problem is the size difference of the synaptosomes of our synapse types of interests. MF and Schaffer collateral synapses are for instance different in size (Rollenhagen and Lübke, 2010; Rollenhagen *et al.*, 2018). The size difference would be a problem for the FASS approach as the sorting depends on the size of the target synapses and the settings would need to be adjusted for MF synapses.

6.2.2 Establishing protein biotinylation in specific synapse types

Due to the problems described above, we decided to generate two mouse lines that allow synapse-specific biotinylation for our experimental approach.

We worked with one mouse line expressing BirA in CA3 pyramidal neurons in the hippocampus (Et-iCre:BioID) enabling us to identify the proteome of Schaffer collateral synapses and one mouse line expressing BirA in dentate gyrus granule cells (Prox1Cre:BioID) to determine the proteome of mossy fiber synapses. The generation of both lines was successful since both, the BirA expression as well as biotinylation in the targeted region, was verified (Figure 5.42 and 5.43). The samples are now being prepared for mass spectrometry analysis. We aim to compare the synaptic proteome of the two synapses as well as the somatic proteome. To do so, the region of interest is microdissected and the somata are separated from the synapses. This is achieved by separation of the dentate gyrus (representing the soma proteome) from the CA3 region (synapse) for the Prox1Cre:BioID line and the CA3 region (soma) from the CA1 region (synapse) for the Et-iCre:BioID line.

This procedure has the advantage that all samples can be treated identical. The size of the investigated synapses for instance is negligible. Using the BioID approach, the microdissection can be performed for both lines in this study but also all other lines of interest because the samples can be processed equally and independent of their size. Solely an efficient expression of BirA has to be achieved, which was for instance not observed for a NG2 mouse line (data not shown).

Variations in the proteome of the MF and Schaffer collateral synapses are expected due to their differences in synaptic plasticity. Another explanation for the difference properties of the synapses would be a difference in the transcriptome instead of the proteome. RIM1 exists for instance in different splice variants and their functional role has not been addressed so far. Therefore, it is possible that different splice variants of RIM1 achieve different functions in the synapse. However, the proteomic analysis is not able to distinguish between different RIM1 splice variants due to the trypsinization of the proteins during the sample processing resulting in small peptides. To answer these questions, our laboratory sorted and isolated dentate gyrus granule cells and CA3 pyramidal neurons to look at differences on the mRNA level (PhD thesis Annika Mayer, unpublished).

The BioID mouse lines represent a novel approach in our laboratory to evaluate the proteome of specific synapses. An efficient biotinylation can be achieved using biotin-

containing food. The expression of BirA and a successful biotinylation can be easily analyzed using immunoblots and immunohistochemical stainings. This approach is applicable for other mouse lines to study other synapses of interest.

7. Outlook

This study identified SRPK2 as a synaptic protein that regulates the protein abundance of several AZ proteins. We identified a potential mechanism how synaptic strength is altered during homeostatic plasticity: SRPK2 phosphorylates and regulates RIM1 nanoclusters at the synapse. The increase of synaptic SRPK2 clusters during presynaptic homeostatic plasticity that initiates the increase of synaptic RIM1 nanoclusters highlights the important role of SRPK2 in synaptic plasticity. It is most likely that SRPK2 regulates RIM1 clustering by phosphorylation. Whether direct or indirect phosphorylation is important has to be addressed in the future. We demonstrated that a phospho-signaling network is regulated by SRPK2 and therefore new players can be studied with respect to their role in synaptic plasticity and also the phosphorylation of RIM1. Future work has to resolve which phosphorylation site is important for the clustering of RIM1. Moreover, the role of SRPK2 for LLPS would be of interest. Does SRPK2 participate in the LLPS that has been demonstrated for RIM1 and RIM-BP? If yes, does SRPK2 initiate or disperse the LLPS of both proteins? Does a specific phosphorylation site in RIM1 achieve the regulation?

To identify key players mediating synaptic plasticity, the proteome analysis of Schaffer collateral and MF synapses will bring new insights. The identification of a synapse-specific proteome is necessary to understand the characteristics of specific synapses that have been studied using other experimental approaches like electrophysiology. Many knock-out mouse lines like RIM1 or Rab3 have been analyzed but the BioID approach enables us to compare the proteome and the impact of the absence of one specific protein on the whole proteome in the synapse.

Here, we established the biotinylation in dentate gyrus granule cells and CA3 pyramidal cells. Our first results indicated a successful approach to identify the proteome of specific synapse types. To achieve this, five biological replicates are now prepared and will be measured in the laboratory of our collaborator in Australia, Mark Graham to quantitatively analyze the protein composition of the dentate gyrus granule cells and CA3 pyramidal cells.

We will then be able to compare the protein composition between the different synapse types with respect to their synaptic protein composition but also the protein

composition of the soma. Moreover, the comparison between the proteome and the transcriptome (PhD thesis Annika Mayer, unpublished) will be performed.

8. Contributions

Contributions of other PhD students or collaborators are mentioned in the text. An overview about the contributions is indicated below:

- Processing of neurons and RIM1 for mass spectrometry was conducted in the laboratory of Mark Graham by Kasper Engholm-Keller and Jesse R. Wark
- Bioinformatic analysis of mass spectrometry was performed by Mark E. Graham and Ash J. Waardenberg
- Radiometric *in vitro* phosphorylation assay was performed with Robert Düster
- Homeostatic plasticity experiments of wild-type, RIM1 cDKO, shSRPK2 knock-down and SRPK2 overexpressing neurons were investigated by Annika Mayer (Susanne Schoch's laboratory)
- dSTORM experiments for ELKS clusters were conducted by Eva M. Schönhense (Susanne Schoch's laboratory)
- FM4-64 and iGluSnFR experiments of different RIM1 phospho-mutants were performed by Alexander Müller (Susanne Schoch's laboratory)
- FIB-SEM analysis of wild-type, SRPK2 knock-down and overexpressing neurons were performed by Isabelle Paulußen (Dirk Dietrich's laboratory)
- Mathematica script to calculate density maps in Mathematica were written by Terrence Daniel McGovern
- FASS experiments were conducted together with Monika Tießen (Dirk Dietrich's laboratory)

9. Appendix

9.1 Generation of a new SRPK2 motif

Ashley J. Waardenberg generated SRPK2 motifs from published SRPK2 targets (Table 9.1, (Daub *et al.*, 2002; Jang *et al.*, 2008; Hong *et al.*, 2012; Duarte *et al.*, 2013; Wang *et al.*, 2017)) and *in vitro* phosphorylation of RIM1 (Figure 5.13).

Protein	Phosphorylation site	Sequence	Reference
Tau	S214	GSRSRTP**S**LPTPPTR	Hong et al., 2012
Acinus	S422	GPRSRSR**S**RDRRRKE	Jang et al., 2008
AEP	S226	CYYDEKR**S**TYLGDWY	Wang et al., 2017
AEP	S328	NTNDLEE**S**RQLTEEI	Wang et al., 2017
HBV core protein	S155	VVRRRGR**S**PRRRTPS	Daub et al., 2002
HBV core protein	S162	SPRRRTP**S**PRRRRSQ	Daub et al., 2002
HBV core protein	S170	PRRRRSQ**S**PRRRRSQ	Daub et al., 2002
BLRF2	S148	NATRRAR**S**RSRGREA	Duarte et al., 2013
BLRF2	S150	TRRARSR**S**RGREAKK	Duarte et al., 2013

Table 9.1: Published SRPK2 targets

The motif of SRPK1 was generated using PhosphoSitePlus database (Hornbeck *et al.*, 2015) and highlights the high preference of SRPK1 to phosphorylate RS dipeptides (Figure 9.1.A). Published SRPK2 targets were used for a curated SRPK2 motif (Figure 9.1.B) The new SRPK2 motif is based on the *in vitro* phosphorylation data of RIM1 by SRPK2 (Figure 9.1.C). Clear differences of both SRPK2 motifs can be noticed compared to the SRPK1 motif. However, the curated SRPK2 motif shares more similarity to the SRPK1 motif than the *in vitro* phosphorylation motif.

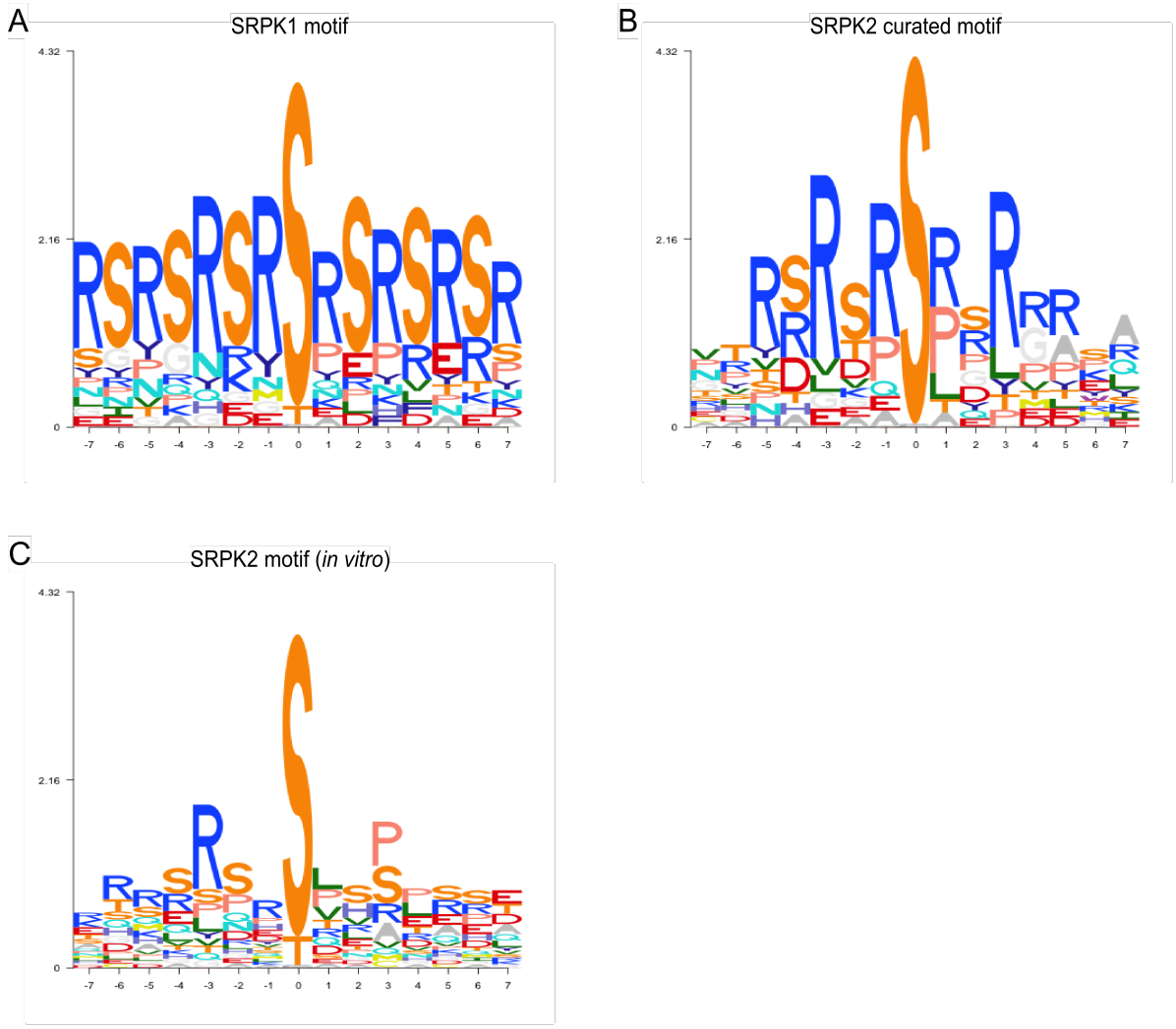

Figure 9.1: Generation of SRPKs motifs.

(A) Motif of SRPK1 is based on PhosphoSitePlus database. **(B)** Motif of SRPK2 using published SRPK2 targets. **(C)** Motif of SRPK2 was generated using the *in vitro* phosphorylation data of RIM1 by SRPK2.

9.2 List of oligonucleotides

Oligonucleotides were synthesized by Invitrogen (Karlsruhe). Lyophilized oligonucleotides were dissolved in Ampuwa water (Fresenius Kabi).

The following oligonucleotides were used to clone RIM1 peptides (Table 9.2). Numbers indicate rat nomenclature of RIM1 (Uniprot ID: Q9JIR4).

DNA (rat sites)	Mouse sites	Sequence (5' to 3')	Direction
RIM1-S285	S285	aattcagaagcaggcatcaagatcaagaagcgagccaccgagggaaaggtaa	Fw
RIM1-S285	S285	tcgacttacctttccctcggtggctcgcttcttgatcttgatgcctgcttctg	Rev
RIM1-S346	S346	aattaggttggagaaagggcgctcccaggactactcagaccggtaa	Fw
RIM1-S346	S346	tcgacttaccggtctgagtagtcctgggagcgccctttctccaacct	Rev
RIM1-S379	S379	aatttaccagactaggtaccgcagcgaccctaacctggctcgctaa	Fw
RIM1-S379	S379	tcgattagcgagccaggttagggtcgctgcggtacctagtctggta	Rev
RIM1-S514	S514	aattagcatgctgcggaacgactcgctgagctccgatcagtcctaa	Fw
RIM1-S514	S514	tcgattaggactgatcggagctcagcgagtcgttccgcagcatgct	Rev
RIM1-S742	S563	aattccttctatttctgttatttctccaaccagccctggagcttaa	Fw
RIM1-S742	S563	tcgattaagctccagggctggttggagaaataacagaaatagaagg	Rev
RIM1-S991	S812	aattaatgtgccattacagaggagcttagatgaaattcatccataa	Fw
RIM1-S991	S812	tcgattatggatgaatttcatctaagctcctctgtaatggcacatt	Rev
RIM1-S1045	S866	aattAagagcaaaacgaggacgaagtgcagaaagcctacacatgtaa	Fw
RIM1-S1045	S866	tcgattacatgtgtaggctttctgcacttcgtcctcgttttgctct	Rev
RIM1-S1078	S899	aattccagatactagtttgcattcaccagaacgagaaaggcactaa	Fw
RIM1-S1078	S899	tcgattagtgcctttctcgttctggtgaatgcaaactagta	Rev

		tctgg	
RIM1-S1175	S1023	aattgtgccagttcgaagcggcagtatagaacaagcaa gcttataa	Fw
RIM1-S1175	S1023	tcgattataagcttgcttgttctatactgccgcttcgaact ggcac	Rev
RIM1-S1203	S1051	aattctagtgccagttcgaagcggcagtatagaacaag caagcttataa	Fw
RIM1-S1203	S1051	tcgattataagcttgcttgttctatactgccgcttcgaact ggcac	Rev
RIM1-S1234	S1082	aattgtgtctcgaagaagcaggagcacgtcacagctca gccagtaa	Fw
RIM1-S1234	S1082	tcgattactggctgagctgtgacgtgctcctgcttcttcg agacac	Rev
RIM1-S1339	S1187	atttctacgtaatgacggtagccagtcggacacggccgt aggtacctaa	Fw
RIM1-S1339	S1187	tcgattaggtacctacggccgtgtccgactggctaccgt cattacg	Rev
RIM1-S1600	S1448	aattcccctgacccgccgggcttcccaatcatctctggaa agttaa	Fw
RIM1-S1600	S1448	tcgattaactttccagagatgattgggaagcccggcgg gtcagggg	Rev
Negative control		aattgttgtcagggacatggcggttgtcagggacatgg cgtaa	Fw
Negative control		tcgattacgccatgtccctgacaaccgccatgtccctgac aac	Rev

Table 9.2: List of oligonucleotides used for cloning RIM1 peptides

The following primers were used to clone RIM1 fragments (Table 9.3).

Fragment	Rat sites (aa)	Sequence (5' to 3')	Direction
Fragment 1	1 - 346	gtggtggaattctagGGCCGGGgaattctatgt	Fw
Fragment 1	1 - 346	acccatggagtctagctccgccttctcgcg	Rev
Fragment 2	563 - 788	gtggtggaattctaggcaaggccaagcgcg	Fw
Fragment 2	563 - 788	acccatggagtctagtaacgtggttgctttactctct ctagcac	Rev
Fragment 3	788 - 1203	gtggtggaattctagaagtcttaccagggcaactct	Fw
Fragment 3	788 - 1203	acccatggagtctagcatccgtctgccttgcattt	Rev
Fragment 4	1203 - 1615	gtggtggaattctagtggggacttcaggaagagc catca	Fw
Fragment 4	1203 - 1615	acccatggagtctagtcatgaccggatgcaggg	Rev

Table 9.3: List of primers used for cloning RIM1 fragments.

The following primers were used for genotyping (Table 9.4).

Primer ID	Primer name	Mouse line	Sequence (5' to 3')
G0117	CAG WPRE rev	BioID	ggcattaaagcagcgtatcc
G0118	CAG BioID fw	BioID	aggacggaatcatcaagcc
G0119	Rosa CAG fw	BioID	aagggagctgcagtggagta
G0120	Rosa CAG rev	BioID	ccgaaaatctgtgggaagtc
G0096	Prox IC1.1	Prox1Cre	actgggatcttcgaactctttggac
G0097	Prox IC1.2	Prox1Cre	gatgttggggcactgctcattcacc
G0098	Prox Cre1	Prox1Cre	ccatctgccaccagccag
G0099	Prox Cre1	Prox1Cre	tcgccatcttccagcagg
G0029	RIM1-WT (#73)	Et-iCre	gcgtgaatccgaaaggtga
G0030	RIM1-WT (#76)	Et-iCre	gctcctaccattgggtggga
G0086	Calb1iCre fw	Et-iCre	cggcgggataaatacagaga
G0087	Calb1iCre rev	Et-iCre	cacagtcagcaggttggaga

Table 9.4: List of primers used for genotyping

10. Abbreviations

aa	Amino acid
AEP	Asparaginyl endopeptidase
APP	Aβ precursor protein
AZ	Active zone
BME	Basal Medium Eagle
BRSK1	BR serine/threonine kinase 1
BSA	Bovine serum albumin
BSN	Bassoon
bp	Base pair
CamKII	Calcium/Calmodulin-dependent protein kinase type II
cAMP	Cycling adenosine monophosphate
CASK	Calcium/Calmodulin dependent serine protein kinase
CAZ	Cytomatrix at the active zone
CDK5	Cyclin-dependent kinase 5
CDKL5	Cyclin-dependent kinase-like 5
cDKO	Conditional double knock-out
CK2	Casein kinase 2
Co-IP	Co-immunoprecipitation
Ctrl	Control
DIV	Day *in vitro*
DMEM	Dulbecco's Modified Eagle's Medium
DNA	Desocyribonucleic acid
dSTORM	Direct stochastic optical reconstruction microscopy
EDTA	Ethylenediaminetetraacetic acid
ELKS	Protein rich in the amino acids E, L, K, S
EM	Electron Microscopy
ERK	Extracellular signal regulated kinase
FASS	Fluorescent activated synaptosome sorting
FCS	Fetal calf serum
FITC	Fluorescein isothiocyanate
FSC	Forward Scatter

GFP	Green fluorescent protein
GST	Glutathione-S-transferase
h	hour
HA	Human influenza hemagglutinin
HBSS	Hank's Buffered Salt Solution
HCl	Hydrochloride
HEK cells	Human embryonic kidney cells
HEPES	4-(2-hydroxyethyl)-1-piperazineethanesulfonic acid
HH	Hippocampus homogenate
IAA	Iodoacetamide
IB	Immunoblotting
ICC	Immunocytochemical staining
IHC	Immunohistochemistry
IMDM	Iscove's Modified Dulbecco's Medium
IP	Immunoprecipitation
IPTG	Isopropyl b-D-1-thiogalactopyranoside
kb	Kilobase pair
kDead	Kinase dead
Kg	Kilogram
LB	Luria Broth
LC-MS	Liquid chromatography-mass spectrometry
LLPS	Liquid-liquid phase separation
LTP	Long-term plasticity
M	Molar
MARK	Microtubule affinity-regulating kinase
MAST1-4	Microtubule Associated Serine/Threonine Kinase 1-4
MBP	Myelin-basic protein
MEA	β-Mercaptoethylamine hydrochloride
MEM	Minimum essential medium
MF	Mossy fiber
mg	Milligram
min	Minutes
mRNA	Messenger RNA
MS	Mass spectrometry

Munc-13	Mammalian Unc-13 homolog
NA	Numerical aperture
NBQX	2,3-dihydroxy-6-nitro-7-sulfamoyl-benzo[f]quinoxaline-2,3-dion
NGS	Normal goat serum
NMJ	Neuromuscular junction
nM	Nanomolar
nm	Nanometer
NT	Neurotransmitter
OD	Optical density
OE	Overexpression
P	Postnatal day
PBS	Phosphate buffered saline
PBST	PBS + Tween-20
PCR	Polymerase chain reaction
Pclo	Piccolo
PEG-400	Polyethylene glycol 400
Pen/Strep	Penicillin/streptomycin
PerCP	Peridinin Chlorophyll Protein Complex
PFA	Paraformaldehyde
PHP	Presynaptic homeostatic plasticity
PKA	Protein kinase A
PKC	Protein kinase C
PNK	Polynucleotide kinase
PPP6r3	Protein phosphatase 6 regulatory subunit 3
PSD	Postsynaptic density
PTV	Piccolo-Bassoon transport vesicles
Rab	Ras-related in brain
rAAV	Recombinant adeno-associated virus
Rev	Reverse
RIMs	Rab3-interacting molecules
RIM-BP	RIM-binding protein
RNA	Ribonucleic acid
ROI	Region of interest
RPM	Rounds per minute

RRP	Readily releasable pool
S2-kDead	Serine protein kinase 2 kinase dead
SAFB1/2	Scaffold attachment factors B1 and 2
SDS	Sodium dodecyl sulfate
SDS PAGE	SDS polyacrylamide gel electrophoresis
sec	Second
SEM	Standard error of mean
SH3	Src Homology 3
shRNA	Small hairpin RNA
SNAP25	Synaptosomal-associated protein of 25 kDa
SRPK	Serine arginine protein kinase
SSC	Side Scatter
Syn	Synapsin
Syph	Synaptophysin
TCEP	Tris(2-carboxyethyl)phosphine hydrochloride
TMT	Tandem mass tag
Ttbk2	Tau-tubulin kinase 2
TTX	Tetrodotoxin
VGCC	Voltage-gated Ca^{2+} channel
WB	Whole brain homogenate
WNK1	WNK Lysine Deficient Protein Kinase 1
WT	Wild-type
µl	Microliter
µm	Micrometer

11. References

Ahmed, M. S. and Siegelbaum, S. A. (2009) 'Recruitment of N-Type Ca(2+) channels during LTP enhances low release efficacy of hippocampal CA1 perforant path synapses.', *Neuron*. United States, 63(3), pp. 372–385. doi: 10.1016/j.neuron.2009.07.013.

Alberini, C. M. (2009) 'Transcription factors in long-term memory and synaptic plasticity.', *Physiological reviews*. United States, 89(1), pp. 121–145. doi: 10.1152/physrev.00017.2008.

Altrock, W. D. *et al.* (2003) 'Functional inactivation of a fraction of excitatory synapses in mice deficient for the active zone protein bassoon.', *Neuron*. United States, 37(5), pp. 787–800. doi: 10.1016/s0896-6273(03)00088-6.

Ambadipudi, S. *et al.* (2017) 'Liquid-liquid phase separation of the microtubule-binding repeats of the Alzheimer-related protein Tau.', *Nature communications*. England, 8(1), p. 275. doi: 10.1038/s41467-017-00480-0.

Benjamini, Y. and Hochberg, Y. (1995) 'Controlling the False Discovery Rate: A Practical and Powerful Approach to Multiple Testing', *Journal of the Royal Statistical Society. Series B (Methodological)*. [Royal Statistical Society, Wiley], 57(1), pp. 289–300. Available at: http://www.jstor.org/stable/2346101.

Biesemann, C. *et al.* (2014) 'Proteomic screening of glutamatergic mouse brain synaptosomes isolated by fluorescence activated sorting', *EMBO Journal*, 33(2), pp. 157–170. doi: 10.1002/embj.201386120.

Bliss, T. V. P. and Lømo, T. (1973) 'Long- lasting potentiation of synaptic transmission in the dentate area of the unanaesthetized rabbit following stimulation of the perforant path', *The Journal of Physiology*, 232(2), pp. 331–356. doi: 10.1113/jphysiol.1973.sp010274.

Bliss, T. V and Gardner-Medwin, A. R. (1973) 'Long-lasting potentiation of synaptic transmission in the dentate area of the unanaestetized rabbit following stimulation of the perforant path.', *The Journal of physiology*. England, 232(2), pp. 357–374. doi: 10.1113/jphysiol.1973.sp010274.

Böhme, M. A. *et al.* (2019) 'Rapid active zone remodeling consolidates presynaptic potentiation.', *Nature communications*. England, 10(1), p. 1085. doi:

10.1038/s41467-019-08977-6.

Boyken, J. *et al.* (2013) 'Molecular profiling of synaptic vesicle docking sites reveals novel proteins but few differences between glutamatergic and GABAergic synapses', *Neuron*. Elsevier Inc., 78(2), pp. 285–297. doi: 10.1016/j.neuron.2013.02.027.

Brangwynne, C. P. *et al.* (2009) 'Germline P granules are liquid droplets that localize by controlled dissolution/condensation.', *Science (New York, N.Y.)*. United States, 324(5935), pp. 1729–1732. doi: 10.1126/science.1172046.

Bruckner, J. J. *et al.* (2017) 'Fife organizes synaptic vesicles and calcium channels for high-probability neurotransmitter release.', *The Journal of cell biology*. United States, 216(1), pp. 231–246. doi: 10.1083/jcb.201601098.

Cai, Q. and Sheng, Z.-H. (2009) 'Molecular motors and synaptic assembly.', *The Neuroscientist : a review journal bringing neurobiology, neurology and psychiatry*. United States, 15(1), pp. 78–89. doi: 10.1177/1073858408329511.

Castillo, P. (2012) 'Presynaptic LTP and LTD of Excitatory and Inhibitory Synapses.pdf', *Cold Spring Harbor perspectives in biology*. doi: 10.1101/cshperspect.a005728.

Castillo, P. E. *et al.* (2002) 'RIM1 alpha is required for presynaptic long-term potentiation', *Nature*, 415(6869), pp. 327–330. doi: Doi 10.1038/415327a.

Chen, H., Tang, A.-H. and Blanpied, T. A. (2018) 'Subsynaptic spatial organization as a regulator of synaptic strength and plasticity.', *Current opinion in neurobiology*. England, 51, pp. 147–153. doi: 10.1016/j.conb.2018.05.004.

Cho, R. W. *et al.* (2015) 'Phosphorylation of Complexin by PKA Regulates Activity-Dependent Spontaneous Neurotransmitter Release and Structural Synaptic Plasticity.', *Neuron*. United States, 88(4), pp. 749–761. doi: 10.1016/j.neuron.2015.10.011.

Citri, A. and Malenka, R. C. (2008) 'Synaptic plasticity: Multiple forms, functions, and mechanisms', *Neuropsychopharmacology*, 33(1), pp. 18–41. doi: 10.1038/sj.npp.1301559.

Cleveland, D. W., Hwo, S. Y. and Kirschner, M. W. (1977) 'Physical and chemical properties of purified tau factor and the role of tau in microtubule assembly.', *Journal of molecular biology*. England, 116(2), pp. 227–247. doi: 10.1016/0022-2836(77)90214-5.

Cohen, L. D. and Ziv, N. E. (2017) 'Recent insights on principles of synaptic protein

degradation.', *F1000Research*. England, 6, p. 675. doi: 10.12688/f1000research.10599.1.

Dani, A. *et al.* (2010) 'Neuron - Superresolution Imaging of Chemical Synapses in the Brain', 68(5), pp. 843–856..

Daub, H. *et al.* (2002) 'Identification of SRPK1 and SRPK2 as the major cellular protein kinases phosphorylating hepatitis B virus core protein.', *Journal of virology*. United States, 76(16), pp. 8124–8137. doi: 10.1128/jvi.76.16.8124-8137.2002.

Davis, G. W. and Müller, M. (2015) 'Homeostatic Control of Presynaptic Neurotransmitter Release', *Annual Review of Physiology*, 77(1), pp. 251–270. doi: 10.1146/annurev-physiol-021014-071740.

Davydova, D. *et al.* (2014) 'Bassoon specifically controls presynaptic P/Q-type Ca2+ channels via RIM-binding protein', *Neuron*, 82(1), pp. 181–194. doi: 10.1016/j.neuron.2014.02.012.

Delvendahl, I., Kita, K. and Muller, M. (2019) 'Rapid and sustained homeostatic control of presynaptic exocytosis at a central synapse.', *Proceedings of the National Academy of Sciences of the United States of America*. United States, 116(47), pp. 23783–23789. doi: 10.1073/pnas.1909675116.

Deng, L. *et al.* (2011) 'RIM proteins activate vesicle priming by reversing autoinhibitory homodimerization of Munc13.', *Neuron*. United States, 69(2), pp. 317–331. doi: 10.1016/j.neuron.2011.01.005.

Ding, J.-H. *et al.* (2006) 'Regulated cellular partitioning of SR protein-specific kinases in mammalian cells.', *Molecular biology of the cell*. United States, 17(2), pp. 876–885. doi: 10.1091/mbc.e05-10-0963.

Driller, J. H. *et al.* (2019) 'Phosphorylation of the Bruchpilot N-terminus in Drosophila unlocks axonal transport of active zone building blocks'. doi: 10.1242/jcs.225151.

Duarte, M. *et al.* (2013) 'An RS motif within the Epstein-Barr virus BLRF2 tegument protein is phosphorylated by SRPK2 and is important for viral replication.', *PloS one*. United States, 8(1), p. e53512. doi: 10.1371/journal.pone.0053512.

Duarte, M. L. *et al.* (2014) 'Protein folding creates structure-based, noncontiguous consensus phosphorylation motifs recognized by kinases.', *Science signaling*. United States, 7(350), p. ra105. doi: 10.1126/scisignal.2005412.

Dudoit, S. *et al.* (2002) 'Statistical methods for identifying genes with differential

expression in replicated cDNA microarray', *Stat Sin*, 12.

Dulubova, I. *et al.* (2005) 'A Munc13/RIM/Rab3 tripartite complex: from priming to plasticity?', *The EMBO journal*. England, 24(16), pp. 2839–2850. doi: 10.1038/sj.emboj.7600753.

Engholm-Keller, K., Waardenberg, Ashley J, *et al.* (2019) 'The temporal profile of activity-dependent presynaptic phospho-signalling reveals long-lasting patterns of poststimulus regulation.', *PLoS biology*. United States, 17(3), p. e3000170. doi: 10.1371/journal.pbio.3000170.

Engholm-Keller, K., Waardenberg, Ashley J., *et al.* (2019) *The temporal profile of activity-dependent presynaptic phospho-signalling reveals long-lasting patterns of poststimulus regulation*, *PLoS biology*. doi: 10.1371/journal.pbio.3000170.

Engholm-Keller, K. and Larsen, M. R. (2016) 'Improving the Phosphoproteome Coverage for Limited Sample Amounts Using TiO2-SIMAC-HILIC (TiSH) Phosphopeptide Enrichment and Fractionation.', *Methods in molecular biology (Clifton, N.J.)*. United States, 1355, pp. 161–177. doi: 10.1007/978-1-4939-3049-4_11.

Faustino, N. A. and Cooper, T. A. (2003) 'Pre-mRNA splicing and human disease.', *Genes & development*. United States, 17(4), pp. 419–437. doi: 10.1101/gad.1048803.

Filiou, M. D. *et al.* (2010) 'Profiling of mouse synaptosome proteome and phosphoproteome by IEF.', *Electrophoresis*. Germany, 31(8), pp. 1294–1301. doi: 10.1002/elps.200900647.

Fisher, R. A. (1934) *Statistical methods for research workers, 5th ed.*, *Statistical methods for research workers, 5th ed.* Oliver and Boyd: Edinburgh.

Fourcaudot, E. *et al.* (2009) 'L-type voltage-dependent Ca(2+) channels mediate expression of presynaptic LTP in amygdala.', *Nature neuroscience*. United States, 12(9), pp. 1093–1095. doi: 10.1038/nn.2378.

Frank, C. A. *et al.* (2006) 'Mechanisms underlying the rapid induction and sustained expression of synaptic homeostasis.', *Neuron*. United States, 52(4), pp. 663–677. doi: 10.1016/j.neuron.2006.09.029.

Gentleman, R. C. *et al.* (2004) 'Bioconductor: open software development for computational biology and bioinformatics.', *Genome biology*. England, 5(10), p. R80. doi: 10.1186/gb-2004-5-10-r80.

Ghosh, G. and Adams, J. A. (2011) 'Phosphorylation mechanism and structure of serine-arginine protein kinases', *FEBS Journal*, 278(4), pp. 587–597. doi: 10.1111/j.1742-4658.2010.07992.x.

Giannakouros, T. *et al.* (2011) 'Serine-arginine protein kinases: A small protein kinase family with a large cellular presence', *FEBS Journal*, 278(4), pp. 570–586. doi: 10.1111/j.1742-4658.2010.07987.x.

Girach, F. *et al.* (2013) 'RIM1alpha SUMOylation is required for fast synaptic vesicle exocytosis.', *Cell reports*. United States, 5(5), pp. 1294–1301. doi: 10.1016/j.celrep.2013.10.039.

Glebov, O. O. *et al.* (2017) 'Nanoscale Structural Plasticity of the Active Zone Matrix Modulates Presynaptic Function', *Cell Reports*. ElsevierCompany., 18(11), pp. 2715–2728. doi: 10.1016/j.celrep.2017.02.064.

Goold, C. P. and Davis, G. W. (2007) 'The BMP ligand Gbb gates the expression of synaptic homeostasis independent of synaptic growth control.', *Neuron*. United States, 56(1), pp. 109–123. doi: 10.1016/j.neuron.2007.08.006.

Gout, S. *et al.* (2012) 'Abnormal expression of the pre-mRNA splicing regulators SRSF1, SRSF2, SRPK1 and SRPK2 in non small cell lung carcinoma.', *PloS one*. United States, 7(10), p. e46539. doi: 10.1371/journal.pone.0046539.

Grauel, M. K. *et al.* (2016) 'RIM-binding protein 2 regulates release probability by fine-tuning calcium channel localization at murine hippocampal synapses.', *Proceedings of the National Academy of Sciences of the United States of America*. United States, 113(41), pp. 11615–11620. doi: 10.1073/pnas.1605256113.

Greengard, P. *et al.* (1993) 'Synaptic vesicle phosphoproteins and regulation of synaptic function.', *Science (New York, N.Y.)*. United States, 259(5096), pp. 780–785. doi: 10.1126/science.8430330.

Grifman, M. *et al.* (1997) 'In vitro phosphorylation of acetylcholinesterase at non-consensus protein kinase A sites enhances the rate of acetylcholine hydrolysis.', *Brain research. Molecular brain research*. Netherlands, 51(1–2), pp. 179–187. doi: 10.1016/s0169-328x(97)00246-5.

Guan, J.-S. *et al.* (2011) 'Cdk5 is required for memory function and hippocampal plasticity via the cAMP signaling pathway.', *PloS one*. United States, 6(9), p. e25735. doi: 10.1371/journal.pone.0025735.

Gui, J.-F., Lane, W. S. and Fu, X.-D. (1994) 'A serine kinase regulates intracellular

loalization of splicing factors in the cell cycle', p. 19.

Gui, J. F. *et al.* (1994) 'Purification and characterization of a kinase specific for the serine- and arginine-rich pre-mRNA splicing factors.', *Proceedings of the National Academy of Sciences of the United States of America*. United States, 91(23), pp. 10824–10828. doi: 10.1073/pnas.91.23.10824.

Han, Y. *et al.* (2011) 'RIM determines Ca(2)+ channel density and vesicle docking at the presynaptic active zone.', *Neuron*. United States, 69(2), pp. 304–316. doi: 10.1016/j.neuron.2010.12.014.

Hanger, D. P. *et al.* (2007) 'Novel phosphorylation sites in tau from Alzheimer brain support a role for casein kinase 1 in disease pathogenesis.', *The Journal of biological chemistry*. United States, 282(32), pp. 23645–23654. doi: 10.1074/jbc.M703269200.

Hanks, S. K. and Quinn, A. M. (1991) 'Protein kinase catalytic domain sequence database: identification of conserved features of primary structure and classification of family members.', *Methods in enzymology*. United States, 200, pp. 38–62. doi: 10.1016/0076-6879(91)00126-h.

Hegde, A. N. (2017) 'Proteolysis, synaptic plasticity and memory.', *Neurobiology of learning and memory*. United States, 138, pp. 98–110. doi: 10.1016/j.nlm.2016.09.003.

Held, R. G. and Kaeser, P. S. (2018) 'ELKS active zone proteins as multitasking scaffolds for secretion.', *Open biology*. England, 8(2). doi: 10.1098/rsob.170258.

Hermey, G. *et al.* (2013) 'Genome-wide profiling of the activity-dependent hippocampal transcriptome.', *PloS one*. United States, 8(10), p. e76903. doi: 10.1371/journal.pone.0076903.

Holderith, N. *et al.* (2012) 'Release probability of hippocampal glutamatergic terminals scales with the size of the active zone.', *Nature neuroscience*. United States, 15(7), pp. 988–997. doi: 10.1038/nn.3137.

Hong, Y. *et al.* (2012) 'SRPK2 Phosphorylates Tau and Mediates the Cognitive Defects in Alzheimer's Disease', *Journal of Neuroscience*, 32(48), pp. 17262–17272. doi: 10.1523/JNEUROSCI.3300-12.2012.

Hornbeck, P. V *et al.* (2015) 'PhosphoSitePlus, 2014: mutations, PTMs and recalibrations.', *Nucleic acids research*. England, 43(Database issue), pp. D512-20. doi: 10.1093/nar/gku1267.

Jang, S.-W. *et al.* (2008) 'Serine/arginine protein-specific kinase 2 promotes leukemia cell proliferation by phosphorylating acinus and regulating cyclin A1.', *Cancer research*. United States, 68(12), pp. 4559–4570. doi: 10.1158/0008-5472.CAN-08-0021.

Jang, S. W. *et al.* (2009) 'Interaction of Akt-phosphorylated SRPK2 with 14-3-3 mediates cell cycle and cell death in neurons', *Journal of Biological Chemistry*, 284(36), pp. 24512–24525. doi: 10.1074/jbc.M109.026237.

Jiang, X. *et al.* (2010) 'A Role for the Ubiquitin-Proteasome System in Activity-Dependent Presynaptic Silencing', *Journal of Neuroscience*, 30(5), pp. 1798–1809. doi: 10.1523/JNEUROSCI.4965-09.2010.

Johnson, E. L., Fetter, R. D. and Davis, G. W. (2009) 'Negative regulation of active zone assembly by a newly identified SR protein kinase', *PLoS Biology*, 7(9). doi: 10.1371/journal.pbio.1000193.

Kaeser-Woo, Y. J. *et al.* (2013) 'Synaptotagmin-12 phosphorylation by cAMP-dependent protein kinase is essential for hippocampal mossy fiber LTP.', *The Journal of neuroscience : the official journal of the Society for Neuroscience*. United States, 33(23), pp. 9769–9780. doi: 10.1523/JNEUROSCI.5814-12.2013.

Kaeser, P. S. *et al.* (2008) 'RIM1 phosphorylation at serine-413 by protein kinase A is not required for presynaptic long-term plasticity or learning', *Proceedings of the National Academy of Sciences*, 105(38), pp. 14680–14685. doi: 10.1073/pnas.0806679105.

Kaeser, P. S. *et al.* (2011) 'RIM proteins tether Ca2+ channels to presynaptic active zones via a direct PDZ-domain interaction', *Cell*, 144(2), pp. 282–295. doi: 10.1016/j.cell.2010.12.029.

Kaeser, P. S. *et al.* (2012) 'RIM genes differentially contribute to organizing presynaptic release sites', *Proceedings of the National Academy of Sciences*, 109(29), pp. 11830–11835. doi: 10.1073/pnas.1209318109.

Kanai, Y. *et al.* (2000) 'KIF5C, a novel neuronal kinesin enriched in motor neurons.', *The Journal of neuroscience : the official journal of the Society for Neuroscience*. United States, 20(17), pp. 6374–6384.

Katayama, N. *et al.* (2017) 'SNAP-25 phosphorylation at Ser187 regulates synaptic facilitation and short-term plasticity in an age-dependent manner.', *Scientific reports*. England, 7(1), p. 7996. doi: 10.1038/s41598-017-08237-x.

Kaufmann, N. *et al.* (2002) 'Drosophila liprin-alpha and the receptor phosphatase Dlar control synapse morphogenesis.', *Neuron*. United States, 34(1), pp. 27–38. doi: 10.1016/s0896-6273(02)00643-8.

Kohansal-Nodehi, M. *et al.* (2016) 'Analysis of protein phosphorylation in nerve terminal reveals extensive changes in active zone proteins upon exocytosis', *eLife*, 5(April2016), pp. 1–25. doi: 10.7554/eLife.14530.

Köhrmann, M. *et al.* (1999) 'Fast, convenient, and effective method to transiently transfect primary hippocampal neurons.', *Journal of neuroscience research*. United States, 58(6), pp. 831–835.

Kong, X. *et al.* (2009) 'CDK11p58 phosphorylation of PAK1 Ser174 promotes DLC2 binding and roles on cell cycle progression.', *Journal of biochemistry*. England, 146(3), pp. 417–427. doi: 10.1093/jb/mvp089.

Koopmans, F. *et al.* (2019) 'SynGO: An Evidence-Based, Expert-Curated Knowledge Base for the Synapse.', *Neuron*. United States, 103(2), pp. 217-234.e4. doi: 10.1016/j.neuron.2019.05.002.

Lazarevic, V. *et al.* (2011) 'Extensive Remodeling of the Presynaptic Cytomatrix upon Homeostatic Adaptation to Network Activity Silencing', *Journal of Neuroscience*, 31(28), pp. 10189–10200. doi: 10.1523/JNEUROSCI.2088-11.2011.

Lazarevic, V. *et al.* (2013) 'Molecular mechanisms driving homeostatic plasticity of neurotransmitter release', *Frontiers in Cellular Neuroscience*, 7(December), pp. 1–10. doi: 10.3389/fncel.2013.00244.

Lee, H. (2006) 'Synaptic plasticity and phosphorylation', *Pharmacol Ther.*, 112(3), pp. 810–832. doi: 10.1016/j.pharmthera.2006.06.003.Synaptic.

Lee, K. J. *et al.* (2013) 'Mossy fiber-CA3 synapses mediate homeostatic plasticity in mature hippocampal neurons.', *Neuron*. United States, 77(1), pp. 99–114. doi: 10.1016/j.neuron.2012.10.033.

Lee, L. *et al.* (2014) 'Regulation of synaptic plasticity and cognition by SUMO in normal physiology and Alzheimer's disease.', *Scientific reports*. England, 4, p. 7190. doi: 10.1038/srep07190.

Lee, S. *et al.* (2012) 'Phospho-dependent ubiquitination and degradation of PAR-1 regulates synaptic morphology and tau-mediated Abeta toxicity in Drosophila.', *Nature communications*. England, 3, p. 1312. doi: 10.1038/ncomms2278.

Leek, J. T. and Storey, J. D. (2007) 'Capturing Heterogeneity in Gene Expression

Studies by Surrogate Variable Analysis', *PLOS Genetics*. Public Library of Science, 3(9), pp. 1–12. doi: 10.1371/journal.pgen.0030161.

Linden, D. J. and Ahn, S. (1999) 'Activation of presynaptic cAMP-dependent protein kinase is required for induction of cerebellar long-term potentiation.', *The Journal of neuroscience : the official journal of the Society for Neuroscience*. United States, 19(23), pp. 10221–10227.

Liu, K. S. Y. *et al.* (2011) 'RIM-binding protein, a central part of the active zone, is essential for neurotransmitter release.', *Science (New York, N.Y.)*. United States, 334(6062), pp. 1565–1569. doi: 10.1126/science.1212991.

Lonart, G. *et al.* (2003) 'Phosphorylation of RIM1α by PKA triggers presynaptic long-term potentiation at cerebellar parallel fiber synapses', *Cell*, 115(1), pp. 49–60. doi: 10.1016/S0092-8674(03)00727-X.

Lonart, G. and Südhof, T. C. (1998) 'Region-Specific Phosphorylation of Rabphilin in Mossy Fiber Nerve Terminals of the Hippocampus', 18(2), pp. 634–640.

Lu, J. *et al.* (2006) 'Structural basis for a Munc13-1 homodimer to Munc13-1/RIM heterodimer switch.', *PLoS biology*. United States, 4(7), p. e192. doi: 10.1371/journal.pbio.0040192.

Luquet, E. *et al.* (2017) 'Purification of Synaptosome Populations Using Fluorescence-Activated Synaptosome Sorting', *Synapse Development*, 1538, pp. 121–134. doi: 10.1007/978-1-4939-6688-2.

Matz, J. *et al.* (2010) 'Rapid structural alterations of the active zone lead to sustained changes in neurotransmitter release.', *Proceedings of the National Academy of Sciences of the United States of America*. United States, 107(19), pp. 8836–8841. doi: 10.1073/pnas.0906087107.

Mermoud, J. E., Cohen, P. T. and Lamond, A. I. (1994) 'Regulation of mammalian spliceosome assembly by a protein phosphorylation mechanism.', *The EMBO journal*. England, 13(23), pp. 5679–5688.

Michlewski, G., Sanford, J. R. and Caceres, J. F. (2008) 'The splicing factor SF2/ASF regulates translation initiation by enhancing phosphorylation of 4E-BP1.', *Molecular cell*. United States, 30(2), pp. 179–189. doi: 10.1016/j.molcel.2008.03.013.

Milovanovic, D. *et al.* (2018) 'A liquid phase of synapsin and lipid vesicles.', *Science (New York, N.Y.)*. United States, 361(6402), pp. 604–607. doi: 10.1126/science.aat5671.

Mizoguchi, A. *et al.* (2002) 'Nectin: an adhesion molecule involved in formation of synapses.', *The Journal of cell biology*. United States, 156(3), pp. 555–565. doi: 10.1083/jcb.200103113.

Monday, H. R., Younts, T. J. and Castillo, P. E. (2018) 'Long-Term Plasticity of Neurotransmitter Release: Emerging Mechanisms and Contributions to Brain Function and Disease.', *Annual review of neuroscience*. United States, 41, pp. 299–322. doi: 10.1146/annurev-neuro-080317-062155.

La Montanara, P. *et al.* (2015) 'Synaptic synthesis, dephosphorylation, and degradation: a novel paradigm for an activity-dependent neuronal control of CDKL5.', *The Journal of biological chemistry*. United States, 290(7), pp. 4512–4527. doi: 10.1074/jbc.M114.589762.

Mosca, T. J. *et al.* (2017) 'Presynaptic LRP4 promotes synapse number and function of excitatory CNS neurons', *eLife*, 6, pp. 1–29. doi: 10.7554/eLife.27347.

Moulder, K. L., Meeks, J. P. and Mennerick, S. (2006) 'Homeostatic regulation of glutamate release in response to depolarization', *Molecular Neurobiology*, 33(2), pp. 133–153. doi: 10.1385/MN:33:2:133.

Müller, M. *et al.* (2011) 'Rab3-GAP controls the progression of synaptic homeostasis at a late stage of vesicle release.', *Neuron*. United States, 69(4), pp. 749–762. doi: 10.1016/j.neuron.2011.01.025.

Müller, M. *et al.* (2012) 'RIM controls homeostatic plasticity through modulation of the readily-releasable vesicle pool.', *The Journal of neuroscience : the official journal of the Society for Neuroscience*. United States, 32(47), pp. 16574–16585. doi: 10.1523/JNEUROSCI.0981-12.2012.

Müller, M., Genc, O. and Davis, G. W. (2015) 'RIM-binding protein links synaptic homeostasis to the stabilization and replenishment of high release probability vesicles.', *Neuron*. United States, 85(5), pp. 1056–1069. doi: 10.1016/j.neuron.2015.01.024.

Murthy, V. N. *et al.* (2001) 'Inactivity produces increases in neurotransmitter release and synapse size.', *Neuron*. United States, 32(4), pp. 673–682. doi: 10.1016/s0896-6273(01)00500-1.

Mylonis, I. and Giannakouros, T. (2003) 'Protein kinase CK2 phosphorylates and activates the SR protein-specific kinase 1.', *Biochemical and biophysical research communications*. United States, 301(3), pp. 650–656. doi: 10.1016/s0006-291x(02)03055-3.

Nahidiazar, L. *et al.* (2016) 'Optimizing imaging conditions for demanding multi-color super resolution localization microscopy', *PLoS ONE*, 11(7), pp. 1–18. doi: 10.1371/journal.pone.0158884.

Nakagawa, O. *et al.* (2005) 'Centronuclear myopathy in mice lacking a novel muscle-specific protein kinase transcriptionally regulated by MEF2', *Genes and Development*, 19(17), pp. 2066–2077. doi: 10.1101/gad.1338705.

Nakamura, Y. *et al.* (2015) 'Nanoscale distribution of presynaptic Ca(2+) channels and its impact on vesicular release during development.', *Neuron*. United States, 85(1), pp. 145–158. doi: 10.1016/j.neuron.2014.11.019.

Ngo, J. C. K. *et al.* (2007) 'SR protein kinase 1 is resilient to inactivation.', *Structure (London, England : 1993)*. United States, 15(1), pp. 123–133. doi: 10.1016/j.str.2006.11.011.

Nieratschker, V. *et al.* (2009) 'Bruchpilot in ribbon-like axonal agglomerates, behavioral defects, and early death in SRPK79D kinase mutants of Drosophila', *PLoS Genetics*, 5(10). doi: 10.1371/journal.pgen.1000700.

Niers, J. M. *et al.* (2011) 'Enhanced in vivo imaging of metabolically biotinylated cell surface reporters.', *Analytical chemistry*. United States, 83(3), pp. 994–999. doi: 10.1021/ac102758m.

Nishi, H., Shaytan, A. and Panchenko, A. R. (2014) 'Physicochemical mechanisms of protein regulation by phosphorylation.', *Frontiers in genetics*. Switzerland, 5, p. 270. doi: 10.3389/fgene.2014.00270.

de Oliveira, P. S. L. *et al.* (2016) 'Revisiting protein kinase-substrate interactions: Toward therapeutic development.', *Science signaling*. United States, 9(420), p. re3. doi: 10.1126/scisignal.aad4016.

Palay, S. L. (1956) 'Synapses in the central nervous system.', *The Journal of biophysical and biochemical cytology*. United States, 2(4 Suppl), pp. 193–202. doi: 10.1083/jcb.2.4.193.

Pereda, A. E. (2015) 'Neurobiology: all synapses are created equal.', *Current biology : CB*. England, 25(1), pp. R38-41. doi: 10.1016/j.cub.2014.11.029.

Pozo, K. and Goda, Y. (2011) 'Unraveling mechanisms of homeostatic synaptic plasticity', *Neuron*, 66(3), pp. 337–351. doi: 10.1016/j.neuron.2010.04.028.Unraveling.

Rappsilber, J., Mann, M. and Ishihama, Y. (2007) 'Protocol for micro-purification, enrichment, pre-fractionation and storage of peptides for proteomics using

StageTips.', *Nature protocols*. England, 2(8), pp. 1896–1906. doi: 10.1038/nprot.2007.261.

Ritchie, M. E. *et al.* (2015) 'limma powers differential expression analyses for RNA-sequencing and microarray studies.', *Nucleic acids research*. England, 43(7), p. e47. doi: 10.1093/nar/gkv007.

De Robertis, E. D. and Bennett, H. S. (1955) 'Some features of the submicroscopic morphology of synapses in frog and earthworm.', *The Journal of biophysical and biochemical cytology*. United States, 1(1), pp. 47–58. doi: 10.1083/jcb.1.1.47.

Robertson, J. D. (1953) 'Ultrastructure of two invertebrate synapses.', *Proceedings of the Society for Experimental Biology and Medicine. Society for Experimental Biology and Medicine (New York, N.Y.)*. United States, 82(2), pp. 219–223. doi: 10.3181/00379727-82-20071.

Rollenhagen, A. *et al.* (2018) 'Structural Properties of Synaptic Transmission and Temporal Dynamics at Excitatory Layer 5B Synapses in the Adult Rat Somatosensory Cortex.', *Frontiers in synaptic neuroscience*. Switzerland, 10, p. 24. doi: 10.3389/fnsyn.2018.00024.

Rollenhagen, A. and Lübke, J. H. R. (2010) 'The mossy fiber bouton: the "common" or the "unique" synapse?', *Frontiers in synaptic neuroscience*. Switzerland, 2, p. 2. doi: 10.3389/fnsyn.2010.00002.

Sakamoto, H. *et al.* (2018) 'Synaptic weight set by Munc13-1 supramolecular assemblies.', *Nature neuroscience*. United States, 21(1), pp. 41–49. doi: 10.1038/s41593-017-0041-9.

Salin, P. A., Malenka, R. C. and Nicoll, R. A. (1996) 'Cyclic AMP mediates a presynaptic form of LTP at cerebellar parallel fiber synapses.', *Neuron*. United States, 16(4), pp. 797–803. doi: 10.1016/s0896-6273(00)80099-9.

Samuels, B. A. *et al.* (2007) 'Cdk5 promotes synaptogenesis by regulating the subcellular distribution of the MAGUK family member CASK.', *Neuron*. United States, 56(5), pp. 823–837. doi: 10.1016/j.neuron.2007.09.035.

Schanzenbächer, C. T. *et al.* (2016) 'Nascent Proteome Remodeling following Homeostatic Scaling at Hippocampal Synapses', *Neuron*, 92(2), pp. 358–371. doi: 10.1016/j.neuron.2016.09.058.

Schanzenbächer, C. T., Langer, J. D. and Schuman, E. M. (2018) 'Time- and polarity-dependent proteomic changes associated with homeostatic scaling at

central synapses', *eLife*, 7, pp. 1–20. doi: 10.7554/eLife.33322.

Schindelin, J. *et al.* (2012) 'Fiji: an open-source platform for biological-image analysis.', *Nature methods*. United States, 9(7), pp. 676–682. doi: 10.1038/nmeth.2019.

Schneider, T. D. and Stephens, R. M. (1990) 'Sequence logos: a new way to display consensus sequences', *Nucleic acids research*, 18(20), pp. 6097–6100. doi: 10.1093/nar/18.20.6097.

Schoch, S. *et al.* (2002) 'RIM1α forms a protein scaffold for regulating neurotransmitter release at the active zone', *Nature*, 415(6869), pp. 321–326. doi: 10.1038/415321a.

Schoch, S. *et al.* (2006) 'Redundant functions of RIM1α and RIM2α in Ca 2+-triggered neurotransmitter release', *EMBO Journal*, 25(24), pp. 5852–5863. doi: 10.1038/sj.emboj.7601425.

Schoch, S. and Gundelfinger, E. D. (2006) 'Molecular organization of the presynaptic active zone', *Cell and Tissue Research*, 326(2), pp. 379–391. doi: 10.1007/s00441-006-0244-y.

Schrimpf, S. P. *et al.* (2005) 'Proteomic analysis of synaptosomes using isotope-coded affinity tags and mass spectrometry.', *Proteomics*. Germany, 5(10), pp. 2531–2541. doi: 10.1002/pmic.200401198.

Serra-Pages, C. *et al.* (1998) 'Liprins, a family of LAR transmembrane protein-tyrosine phosphatase-interacting proteins.', *The Journal of biological chemistry*. United States, 273(25), pp. 15611–15620. doi: 10.1074/jbc.273.25.15611.

Shapira, M. *et al.* (2003) 'Unitary assembly of presynaptic active zones from Piccolo-Bassoon transport vesicles.', *Neuron*. United States, 38(2), pp. 237–252. doi: 10.1016/s0896-6273(03)00207-1.

Sigrist, S. J. and Petzoldt, A. G. (2016) 'Nanocolumns at the heart of the synapse', *Nature*, 536(7615), pp. 151–152. doi: 10.1038/nature18917.

Sossin, W. S. (2007) 'Isoform specificity of protein kinase Cs in synaptic plasticity.', *Learning & memory (Cold Spring Harbor, N.Y.)*. United States, 14(4), pp. 236–246. doi: 10.1101/lm.469707.

Su, S. C. *et al.* (2012) 'Regulation of N-type voltage-gated calcium channels and presynaptic function by cyclin-dependent kinase 5.', *Neuron*. United States, 75(4), pp. 675–687. doi: 10.1016/j.neuron.2012.06.023.

Südhof, T. C. (2012) 'The presynaptic active zone', *Neuron*, 75(1), pp. 11–25. doi: 10.1016/j.neuron.2012.06.012.

Takamori, S. *et al.* (2006) 'Molecular Anatomy of a Trafficking Organelle', *Cell*, 127(4), pp. 831–846. doi: 10.1016/j.cell.2006.10.030.

Takeuchi, M. and Yanagida, M. (1993) 'A mitotic role for a novel fission yeast protein kinase dsk1 with cell cycle stage dependent phosphorylation and localization.', *Molecular biology of the cell*. United States, 4(3), pp. 247–260. doi: 10.1091/mbc.4.3.247.

Tang, A. H. *et al.* (2016) 'A trans-synaptic nanocolumn aligns neurotransmitter release to receptors', *Nature*. Nature Publishing Group, 536(7615), pp. 210–214. doi: 10.1038/nature19058.

Tang, Z., Yanagida, M. and Lin, R. J. (1998) 'Fission yeast mitotic regulator Dsk1 is an SR protein-specific kinase.', *The Journal of biological chemistry*. United States, 273(10), pp. 5963–5969. doi: 10.1074/jbc.273.10.5963.

Tazi, J., Bakkour, N. and Stamm, S. (2009) 'Alternative splicing and disease.', *Biochimica et biophysica acta*. Netherlands, 1792(1), pp. 14–26. doi: 10.1016/j.bbadis.2008.09.017.

Tsianou, D. *et al.* (2009) 'The enzymatic activity of SR protein kinases 1 and 1a is negatively affected by interaction with scaffold attachment factors B1 and 2.', *The FEBS journal*. England, 276(18), pp. 5212–5227. doi: 10.1111/j.1742-4658.2009.07217.x.

Tsien, J. Z., Huerta, P. T. and Tonegawa, S. (1996) 'The essential role of hippocampal CA1 NMDA receptor-dependent synaptic plasticity in spatial memory.', *Cell*. United States, 87(7), pp. 1327–1338. doi: 10.1016/s0092-8674(00)81827-9.

Tyanova, S., Temu, T. and Cox, J. (2016) 'The MaxQuant computational platform for mass spectrometry-based shotgun proteomics.', *Nature protocols*. England, 11(12), pp. 2301–2319. doi: 10.1038/nprot.2016.136.

Uezu, A. *et al.* (2016) 'Identification of an elaborate complex mediating postsynaptic inhibition', *Science*, 353(6304), pp. 1123–1129. doi: 10.1126/science.aag0821.

Vara, H. *et al.* (2009) 'ERK activation in axonal varicosities modulates presynaptic plasticity in the CA3 region of the hippocampus through synapsin I.', *Proceedings of the National Academy of Sciences of the United States of America*. United States, 106(24), pp. 9872–9877. doi:

10.1073/pnas.0900077106.

Venables, J. P. (2006) ‘Unbalanced alternative splicing and its significance in cancer.’, *BioEssays : news and reviews in molecular, cellular and developmental biology*. United States, 28(4), pp. 378–386. doi: 10.1002/bies.20390.

Waardenberg, A. J. (2017) ‘Statistical Analysis of ATM-Dependent Signaling in Quantitative Mass Spectrometry Phosphoproteomics.’, *Methods in molecular biology (Clifton, N.J.)*. United States, 1599, pp. 229–244. doi: 10.1007/978-1-4939-6955-5_17.

Wang, H. Y. *et al.* (1998) ‘SRPK2: A differentially expressed SR protein-specific kinase involved in mediating the interaction and localization of pre-mRNA splicing factors in mammalian cells’, *Journal of Cell Biology*, 140(4), pp. 737–750. doi: 10.1083/jcb.140.4.737.

Wang, Z. H. *et al.* (2017) ‘Delta-Secretase Phosphorylation by SRPK2 Enhances Its Enzymatic Activity, Provoking Pathogenesis in Alzheimer’s Disease’, *Molecular Cell*. Elsevier Inc., 67(5), pp. 812-825.e5. doi: 10.1016/j.molcel.2017.07.018.

Wegmann, S. *et al.* (2018) ‘Tau protein liquid-liquid phase separation can initiate tau aggregation.’, *The EMBO journal*. England, 37(7). doi: 10.15252/embj.201798049.

Weingarten, J. *et al.* (2014) ‘The proteome of the presynaptic active zone from mouse brain.’, *Molecular and cellular neurosciences*. United States, 59, pp. 106–118. doi: 10.1016/j.mcn.2014.02.003.

Weisskopf, M. G. *et al.* (1994) ‘Mediation of hippocampal mossy fiber long-term potentiation by cyclic AMP.’, *Science (New York, N.Y.)*. United States, 265(5180), pp. 1878–1882. doi: 10.1126/science.7916482.

Wessel, D. and Flugge, U. I. (1984) ‘A method for the quantitative recovery of protein in dilute solution in the presence of detergents and lipids.’, *Analytical biochemistry*. United States, 138(1), pp. 141–143. doi: 10.1016/0003-2697(84)90782-6.

Weyhersmuller, A. *et al.* (2011) ‘Rapid active zone remodeling during synaptic plasticity.’, *The Journal of neuroscience : the official journal of the Society for Neuroscience*. United States, 31(16), pp. 6041–6052. doi: 10.1523/JNEUROSCI.6698-10.2011.

Whittaker, V., Michaelson, I. and Kirkland, R. (1964) 'The separation of synaptic vesicles from nerve-ending particles ("synaptosomes")', *Biochemical Journal*, 90(2), pp. 293–303. doi: 10.1042/bj0900293.

Wille, H. *et al.* (1992) 'Alzheimer-like paired helical filaments and antiparallel dimers formed from microtubule-associated protein tau in vitro.', *The Journal of cell biology*. United States, 118(3), pp. 573–584. doi: 10.1083/jcb.118.3.573.

Windgassen, M. *et al.* (2004) 'Yeast shuttling SR proteins Npl3p, Gbp2p, and Hrb1p are part of the translating mRNPs, and Npl3p can function as a translational repressor.', *Molecular and cellular biology*. United States, 24(23), pp. 10479–10491. doi: 10.1128/MCB.24.23.10479-10491.2004.

Wu, X. *et al.* (2019) 'RIM and RIM-BP Form Presynaptic Active-Zone-like Condensates via Phase Separation.', *Molecular cell*. United States, 73(5), pp. 971-984.e5. doi: 10.1016/j.molcel.2018.12.007.

Yamanaka, M. *et al.* (2016) 'Pre-LTP requires extracellular signal-regulated kinase in the ACC.', *Molecular pain*. United States, 12. doi: 10.1177/1744806916647373.

Yao, I. *et al.* (2007) 'SCRAPPER-dependent ubiquitination of active zone protein RIM1 regulates synaptic vesicle release.', *Cell*. United States, 130(5), pp. 943–957. doi: 10.1016/j.cell.2007.06.052.

Zalutsky, R. A. and Nicoll, R. A. (1990) 'Comparison of two forms of long-term potentiation in single hippocampal neurons.', *Science (New York, N.Y.)*. United States, 248(4963), pp. 1619–1624. doi: 10.1126/science.2114039.

Zeng, M. *et al.* (2016) 'Phase Transition in Postsynaptic Densities Underlies Formation of Synaptic Complexes and Synaptic Plasticity.', *Cell*. United States, 166(5), pp. 1163-1175.e12. doi: 10.1016/j.cell.2016.07.008.

Zhen, M. and Jin, Y. (1999) 'The liprin protein SYD-2 regulates the differentiation of presynaptic termini in C. elegans.', *Nature*. England, 401(6751), pp. 371–375. doi: 10.1038/43886.

Zhong, X.-Y. *et al.* (2009) 'Regulation of SR protein phosphorylation and alternative splicing by modulating kinetic interactions of SRPK1 with molecular chaperones.', *Genes & development*. United States, 23(4), pp. 482–495. doi: 10.1101/gad.1752109.

Zhou, J. *et al.* (2019) 'Cyclin-Dependent Kinase 5-Dependent BAG3 Degradation Modulates Synaptic Protein Turnover.', *Biological psychiatry*. United States.

doi: 10.1016/j.biopsych.2019.11.013.

Zhuo, Y. J. *et al.* (2018) 'Enhanced expression of SRPK2 contributes to aggressive progression and metastasis in prostate cancer.', *Biomedicine & pharmacotherapy = Biomedecine & pharmacotherapie*. France, 102, pp. 531–538. doi: 10.1016/j.biopha.2018.03.079.

Zürner, M. *et al.* (2011) 'Analyses of the spatiotemporal expression and subcellular localization of liprin-α proteins', *Journal of Comparative Neurology*, 519(15), pp. 3019–3039. doi: 10.1002/cne.22664.

12. Acknowledgement

During my PhD I had the pleasure to work in a great team of very kind, motivated, skilled people without whom the preparation of this thesis would have been impossible.

I would like to express my gratitude to Prof. Dr. Susanne Schoch for giving me the opportunity to do my thesis work in her lab. From the first day I enjoyed working on this project and you have been a great mentor during the past years. It was always possible to bother you in case of frustrating results and your enthusiasm and new ideas helped to overcome these times.

I wish to thank Prof. Dr. Walter Witke for being the co-advisor of my PhD thesis and Prof. Dr. Alf Lamprecht for their time as part of my thesis committee.

I would like to thank Prof. Dr. Dirk Dietrich for his supervision. I learned a lot during the last years (not only proper axis labeling) that enabled me to work precisely during my PhD but will also help me for future work.

I am deeply grateful to all my colleagues in the AG Schoch/Becker, who were always there to help, discuss, enjoy a coffee or beer and made the lab a second home for the last years.
Ein großer Dank geht an Sabine, die jede Neuronenbestellung irgendwie möglich gemacht hat. Außerdem danke ich allen anderen TAs für ihre Unterstützung im Labor, bei Mäusen oder die Herstellung der vielen Viren.

Vielen Dank an Eva für deine Hilfe in all den Jahren. Ich werde die vielen Stunden am STORM und der gemeinsamen Cluster Analyse nie vergessen. Ich hoffe es werden noch viele weitere Pils-Kölsch Abende folgen.

Danke Alex für deine Unterstützung während des ganzen PhDs und beim SRPK2

Projekt. Du hast immer geholfen, wenn man nicht weiterkam und hattest auch immer ein offenes Ohr, um die neusten Ergebnisse zu diskutieren.

Annika auch dir danke ich für die Unterstützung im SRPK2 Projekt, dass du immer ein offenes Ohr hattest und wir selbst beim Synaptotagmin1 Assay noch gute Laune haben konnten.

Danke Despina, dass selbst Klonierungen Spaß gemacht haben und all die Unterstützung in den letzten Jahren.

Danke Jule für die Hilfe mit den Mäusen und Tierversuchsanträgen.

Ein großer Dank geht an meine Familie und Freunde, die mich nicht nur während meines PhDs, sondern der ganzen Ausbildung begleitet und mich in allen Lebenslagen unterstützt haben. Ein besonderer Dank geht an meine Biochemiker Mädels, mit denen ich das erste Mal eine PCR pipettiert habe und die mich bis zum letzten Kapitel der Doktorarbeit unterstützt haben.
Ich möchte mich von tiefstem Herzen bei meinen Eltern bedanken, die immer eine großartige Unterstützung waren und es immer möglich ist euch um Rat zu fragen.

13. Publications

13.1 Journal articles

Betzin J, Müller JA, Engholm-Keller K, Oprişoreanu AM, Mayer A, Paulußen I, Schönhense EM, Gulakova P, McGovern TD, Geschossman L, Düster R, Wark JR, Becker A, Waardenberg AJ, Graham ME, Dietrich D, Schoch S. *Control of presynaptic function and plasticity by strategic phosphorylation of RIM1 by SRPK2*. In prep. 2020

13.2 Book Chapters

Schoch S, Müller JA, Schönhense EM, **Betzin J**. *Liprins, ELKS and RIM-BP Proteins.* Reference Module in Biomedical Sciences 2018

13.2. Poster presentations

Only first author presentations are listed.

Betzin J, Müller JA, Oprişoreanu AM, Engholm-Keller K, Becker AJ, Dietrich D, Graham M, Schoch S. *Role of SR Protein Kinase 2 (SRPK2) on Composition and Function of the Active Zone.* BonnBrain^3, 2018

Betzin J, Müller JA, Oprişoreanu AM, Engholm-Keller K, Becker AJ, Dietrich D, Graham M, Schoch S. *Role of SR Protein Kinase 2 (SRPK2) on Composition and Function of the Active Zone.* Society for Neuroscience. Annual Meeting, San Diego, 2018

Betzin J, Müller JA, Oprişoreanu AM, Schönhense EM, Engholm-Keller K, Becker AJ, Dietrich D, Graham M, Schoch S. *Role of SR Protein Kinase 2 (SRPK2) on Composition and Function of the Active Zone.* BonnBrain^3, 2019

Betzin J, Müller JA, Mayer A, Oprişoreanu AM, Waardenberg A, Becker AJ, Dietrich D, Graham M, Schoch S. *SRPK2 regulates RIM1 phosphorylation status to tune presynaptic function and plasticity.* Gordon Meeting. Excitatory Synapses and Brain Function, 2019